UC Riverside
UC Riverside Electronic Theses and Dissertations

Title

Influence of Structural and Compositional Heterogeneities on Nanoscale Thermal Transport and Magnetization Dynamics

Permalink

https://escholarship.org/uc/item/4h1819k2

Author

Mohan, Ramya

Publication Date

2021

Copyright Information

Peer reviewed|Thesis/dissertation

UNIVERSITY OF CALIFORNIA
RIVERSIDE

Influence of Structural and Compositional Heterogeneities on Nanoscale Thermal
Transport and Magnetization Dynamics

A Dissertation submitted in partial satisfaction
of the requirements for the degree of

Doctor of Philosophy

in

Materials Science & Engineering

by

Ramya Mohan

September 2021

Dissertation Committee:
      Prof. Richard B. Wilson, Chairperson
      Prof. Suveen Mathaudhu
      Prof. Sinisa Coh

The Dissertation of Ramya Mohan is approved:

_____

_____

_____

                                                    Committee Chairperson

University of California, Riverside

Acknowledgements

I would like to first express my gratitude to my advisor, Prof. Richard B. Wilson, for accepting me into his group, during what was possibly the lowest point of my entire life. In April 2019, I transitioned labs during the ~4th year (!) of my Ph.D., and I wasn't sure if I had what it would take to make it to the finish line. *Circa* 2 years later, and I now have a dissertation that I'm very proud of. And I only have Richard to thank for that. He set me up for success from the very beginning, by providing me with the best possible mentorship and an intellectually stimulating lab environment, conducive for high caliber research. More importantly, his relentless drive and enthusiastic pursuit for scientific discovery re-ignited my own passion for academia, and for that, I'm incredibly grateful. I truly, won the advisor lottery with Richard!

I would next, like to thank Prof. Suveen Mathaudhu and Prof. Sinisa Coh, for being part of my dissertation committee, and for offering their time and feedback with my research. I would also want to thank all the collaborators who contributed to my work - Prof. Ji-Cheng Zhao (University of Maryland) and his group, Prof. Reza Abbaschian

Barnard (at beamline #8.3.2., ALS, LBNL – Berkeley, CA); Dr. Eric Schaible and Dr. Chenhui Zhu (at beamline #7.3.3., ALS, LBNL – Berkeley, CA); Dr. Mikhail (Misha) Zhernenkov and Dr. Yugang Zhang (at beamline – SMI, NSLS-II, BNL, Upton, NY) and Seth Menser (at the San Diego Zoo).

I am deeply grateful for the support and friendship of my former lab-mates, who have by now, become family to me – Parawee Pumwongpitak, Steven Herrera, Morgan Dundon, Luz Cruz, Nicholas Yaraghi, Thomas Dugger, Jesus Rivera, Somchate Wasantwisut, Taifeng Wang, Ruoheng Zhao, Christopher Salinas, and Joshua Edwards. Thanks for all the hikes, the delicious food, introducing me to night-long board-games (Risk!!), and of course, all the jokes and banter. I've treasured every minute, and I wouldn't have survived grad school without you all! I'm looking forward to seeing us all thrive together and build on our wonderful friendship in the years to come.

Special thanks are also due to my other friends from USC/UCR – Dr. Harshavardhan Mylapilli, Raghu Reddy, Dr. Bhogesh Seemala, Dr. Sarah Allec, Dr. Trupti Terse-Thakoor, Dr. Claudia Villarreal, Dr. Wei Huang, Nahal Taremi, Dr. Nicholas Derimow, and Dr. Fabian Villalobos, amongst many others.

Finally, I would like to thank my family. I have been lucky to witness firsthand the power of determination and sheer will, through the course of my mother's career. Mom, you've been a pioneer in so many ways! I love you, and I will always aspire to be like you. Thank you for all the encyclopedias, science magazine subscriptions, for enrolling me in the best possible high school in Goa – Manovikas, and most importantly, for making sure I had all the freedom and opportunity to follow my dreams – this

dissertation is as much, your accomplishment, as it is mine. To my (late) grandmother, Rajam Paati, the most intelligent and the most beautiful woman in the world….you brought me up with the best bed-time stories, instilled in me an appreciation for Indian literature and mythology, and are largely responsible for my moral compass. You've epitomized happiness, peace, and unconditional love in my life. I miss you each day. To my brother, Vinay, you've been a constant source of joy and delight growing up. Also, you are the smartest person I know, and I will always wish you the very best that life has to offer. Thank you for making my childhood fun. I am excited to see you flourish in your career and be happy.

To my closest and very best friend, Awez, from our motorbike rides in Hyderabad to the cross-country road trips in the US – over the last ten-odd years, we have both, come a long way! You have been my "rock of Gibraltar", and I have heavily relied on you for almost everything. It is no wonder my mother coined for you the perfect moniker – "always Awez". I have watched you grow heaps and bounds into a wonderful man and an excellent engineer, and I'm so proud of you. I look forward to seeing you live your American Dream (white picket fence and all), because you deserve nothing less. You inspire me to be better. Thank you.

Long story short, it did take a village.

Ad astra per aspera

Dedicated to

The two women who paved the path I walk on......

My Mother, Dr. Vijaya Mohan
Founder & CEO, Srinivasa Educational Society, Kolhapur (Maharashtra), India.

&

My Grandmother, [Late] Mrs. T. K. Rajammal
High School Gold Medalist (Batch of '1941), Palakkad (Kerala), India.

ABSTRACT OF THE DISSERTATION

Influence of Structural and Compositional Heterogeneities on Nanoscale Thermal
Transport and Magnetization Dynamics

by

Ramya Mohan

Doctor of Philosophy, Graduate Program in Materials Science & Engineering
University of California, Riverside, September 2021
Prof. Richard B. Wilson, Chairperson

The ability to predict and control thermal/magnetic properties is crucial for numerous

applications. Incorporating materials with distinct structure-property relationships could

offer tantalizing new possibilities in the design of denser electronic components with

efficient thermal management. Hence, it is important to understand how variations in

elemental composition and structural inhomogeneities influence thermal transport and/or

magnetization. The primary goal for my dissertation research is to use Time-Domain

Thermo-Reflectance (TDTR) to generate 2-dimensional thermal conductivity maps of

two distinct material systems: (a) ferromagnetic Co-Fe alloys, and (b) Al-PVDF

nanocomposites. I also use Time-Resolved Magneto-Optic Kerr Effect (TR-MOKE) to

investigate magnetization dynamics in Co-Fe alloys. First, I summarize the experimental

results of the magnetization dynamics in Co-Fe alloys. Through TR-MOKE experiments,

I show that Co-Fe compositions that exhibit low Gilbert damping parameters (at the

nanosecond timescale) also feature prolonged ultrafast demagnetization responses (at the

femtosecond timescale) upon photoexcitation. Thus, I report a strong correlation between

the dynamics at both timescales, indicating that the same physical mechanisms likely govern both phenomena. Next, I interrogate the thermal conductivity in Co-Fe alloys. I conduct TDTR measurements on Co-Fe thin films and arc-melted alloys, and spatially map the thermal conductivity on a Co-Fe diffusion multiple. I report two main results: (i) the thermal conductivity does not appear to be strongly influenced by crystalline disorder in Co-Fe alloys, and (ii) Co-Fe compositions that feature ultralow magnetic damping also exhibit significantly high non-electronic contribution to thermal transport. I hypothesize that the magnon thermal transport is likely to be very high at these compositions. Finally, I present high-resolution thermal conductivity maps of Al-PVDF nanocomposite films with varied Al volume fractions (0 – 50%). My thermo-reflectance mapping technique has sub-micron resolution and demonstrates how thermal transport properties vary spatially across the polymer, metal, and metal-polymer interfaces. I show that increasing the Al volume fraction to 50% enhances the bulk thermal conductivity of the polymer film by a factor of 2. In certain areas with coalesced Al particles, the local thermal conductivity dramatically increases by a factor of 250. A careful understanding of the spatial variation in the thermal conductivity will aid in the prediction of flame propagation and combustion characteristics in Al-PVDF films.

Table of Contents

List of Figures

Chapter 1.

Introduction

The primary goal for my dissertation research is to use Time-Domain Thermo-Reflectance (TDTR) to generate sub-micron resolution 2-D thermal conductivity maps of material systems with structural and compositional inhomogeneities. The mapping technique I developed, allows for high-throughput measurements of thermal properties. These maps enable the visualization and quantification of how thermal conductivity and/or heat capacity is influenced by composition, structural inhomogeneities, structural anisotropy, and interfaces.

In this dissertation, I explore the nanoscale thermal and magnetic properties in two different classes of materials –

(i)   ferromagnetic Co-Fe alloys, where the electronic band structure varies as a function of composition; and

(ii)   Al-PVDF energetic nanocomposites, featuring a metal and polymer component with highly dissimilar thermal transport properties.

1.1 Magnetization Dynamics and Magnetic Thermal Transport in Co-Fe alloys:

Several recent investigations have advanced the understanding of how structure-property relationships in ferromagnetic metal alloys affect the magnetization dynamics on nanosecond timescales. A similar understanding for the magnetization dynamics on femto- to pico-second timescales does not yet exist.

It is difficult to find low damping ferromagnets, due to the scattering of magnons by the conduction electrons in a metallic system. However, recent investigations have shown that certain "special" Co-Fe alloy compositions (for e.g., $Co_{0.25}Fe_{0.75}$) exhibit extremely low damping, comparable to ferrimagnetic insulators [1]–[4]. This is primarily due to the unique electronic band structures at these compositions that feature a limited availability of conduction electrons [1]. Thus, there is a possible suppression in electron-magnon scattering, leading to longer magnon lifetimes. In addition to controlling damping rates, electron-magnon scattering can, in principle, affect the ability of magnons to carry heat, i.e., magnon thermal conductivity. This formed my motivation to conduct two fundamental investigations into the Co-Fe alloy system to determine:

(a) their ultrafast magnetization dynamics and how they are influenced by electron-phonon and electron-magnon interaction strengths; and

(b) the influence of electron-magnon scattering rates on the thermal conductivity of magnons.

To address (a), I perform time-resolved magneto optic Kerr effect (TRMOKE) measurements of magnetization dynamics in Co-Fe alloys, spanning femto- to nano-second regimes. In this study, I experimentally demonstrate that Co-Fe compositions exhibiting low Gilbert damping parameters also feature prolonged ultrafast demagnetization responses upon laser excitation. In addition, I analyze the experimental TR-MOKE data using the phenomenological Three Temperature Model (3TM) and the Landau-Lifshitz-Gilbert (LLG) equation. These analyses reveal a strong compositional dependence of the dynamics on electron-phonon interaction strengths, across both femto-

2

and nanosecond regimes. I show that Co-Fe compositions with low damping feature weaker e-p coupling. Altogether, my findings offer key insights into the underlying physics that govern femtosecond magnetization dynamics. Controlling magnetic order is a critical design criterion with far-reaching implications in the development of high-speed energy-efficient data storage devices.

Part (b) focusses on correlating Co-Fe composition to thermal transport. Typically, in metals, the thermal conductivity is dominated by electrons. A small contribution is assumed from lattice vibrations. Whether magnons carry heat in ferromagnetic metals is not yet known, and is assumed to be negligible. However, recent theoretical predictions by [5] indicate a non-trivial value (~7 W/m-K) for the magnon contribution to thermal conductivity in bcc Fe at 300K. This theoretical result formed the basis for my experimental investigation into whether the non-electronic contribution (i.e., from magnons and phonons) is higher in Co-Fe compositions that feature weaker e-p interactions, and longer magnon lifetimes. To test this, I conducted TDTR experiments and four-probe electrical resistivity measurements on two different Co_xFe_{1-x} systems: thin films and arc melted alloys. I also used my 2D mapping technique to measure the thermal conductivity across the Co-Fe interface of a diffusion multiple. To estimate the non-electronic thermal conductivity, I used the Wiedemann-Franz law to subtract the electronic contribution. I also used the Smith-Palmer equation to estimate the compositional dependence of the non-electronic thermal conductivities. My results indicate a correlation between the composition, low damping, and the non-electronic thermal conductivity in Co-Fe alloys. I show that compositions with low magnetic

3

damping also exhibit significantly higher non-electronic thermal conductivities. Since Co and Fe have similar atomic mass, I assume that the lattice contribution is not a strong function of composition. Hence, I hypothesize that this "excess" thermal conductivity arises from the magnon contribution. My results are of interest to the spin caloritronic, magnonic, and nanoscale thermal transport communities.

1.2. Thermal Transport in Al-PVDF Nanocomposite Films:

Fluorine-rich polymers incorporated with aluminum nanoparticles, such as PVDF-Al, are of interest to the energetics community, due to their superior flame propagation characteristics. Recent investigations have shown that high Al volume fractions in PVDF-Al nanocomposites lead to self-sustained ignition and greater flame spread [6]–[8]. The bulk thermal conductivities of Al and PVDF vary by nearly three orders of magnitude ($\Lambda_{Al} \sim 140$ W/m-K, $\Lambda_{PVDF} \sim 0.2$ W/m-K). Hence, it is strongly suggested that at low Al volume fractions, energy transfer in PVDF-Al nanocomposites is impeded by PVDF, which interrupts the combustion process [7]. The motivation for my research is to test this hypothesis by interrogating the effects of microstructural Al inhomogeneities on thermal transport in PVDF-Al films. Measurements of these films are exceptionally difficult because they feature large amounts of spatial inhomogeneities. My mapping technique has a spatial resolution of ~1.4 μm. The resolution is given by $\frac{w_0}{\sqrt{2}}$, where w_0 is the $\frac{1}{e^2}$ radius of the laser beam. Thus, I can visualize and quantify how transport properties vary spatially in these films.

My bulk TDTR measurements has yielded data that shows steadily increasing thermal conductivity as a function of increasing Al volume fraction. At 50% Al volume fraction, the bulk thermal conductivity (Λ_{bulk}) is 0.58 W/m-K. This is a factor of ~2 increase when compared to PVDF with no Al. Furthermore, I studied the effects of structural inhomogeneities in microtomed Al-PVDF films using the 2-dimensional mapping technique. I obtain spatially corelated thermal conductivity measurements across areas rich in PVDF, areas featuring Al nanoparticle agglomerates, and Al-PVDF interfaces. My experimental measurements offer insight into the thermal conductivity of PVDF-Al films. This will allow for the quantitative modelling of conductive heat transfer by the energetics community, to predict flame propagation and combustion characteristics of Al-PVDF propellant systems.

1.3. Organization of this Dissertation:

My dissertation is organized as follows: In Chapter 2, I describe the macroscopic structure-function relationships in a woody protective seed casing in an Australian pyrophytic plant species. Chapter 3 summarizes the femto-magnetism and nanosecond precessional dynamics in Co-Fe alloys. Chapter 4 presents the thermal conductivity and electrical resistivity measurements in Co-Fe alloys. Both thermal and magnetic properties in Chapters 3 and 4 are described as a function of Co-concentration. In Chapter 5, I provide bulk TDTR measurements as well as high resolution thermal conductivity maps in Al-PVDF nanocomposite films. Finally, in Chapter 6, I summarize my findings and present my conclusions.

Chapter 2.

Design of Lightweight Fire-Resistant Composites: Lessons from The *Banksia*

2.1 Introduction:

The follicle valves of the genus *Banksia* are made almost entirely of organic polymeric components and yet exhibit remarkable tolerance to fire and abrading predation, likely due to their chemical components and hierarchically ordered microstructure [9]–[13]. A follicle is a capsule composed of two valves sealed shut with resin. Each follicle contains two seeds, divided by a seed separator to form a follicle-seed system, see Figure. 2.1. The seed separator, reportedly, acts like a "lever" drawing the seeds out of the follicle after the fires subside into a nutrition-rich environment. Exposure to temperatures of up to 600°C in the forest fires thermally degrades the resin binding the follicle valves. The valves and the outer wings of the seed separator reflex forming a protective shield around the seeds. Thereafter, the hygroscopic seed separator, upon exposure to moisture, in the form of rainfall cycles or atmospheric humidity, acts as a mechanical lever to eject the seeds out into a recently hydrated, nutrient-rich post-fire

environment optimal for germination. A careful investigation of the ultrastructure-thermal property relationships across the architectures within these systems will uncover critical design strategies to develop next-generation multifunctional materials for structural and high-temperature applications.
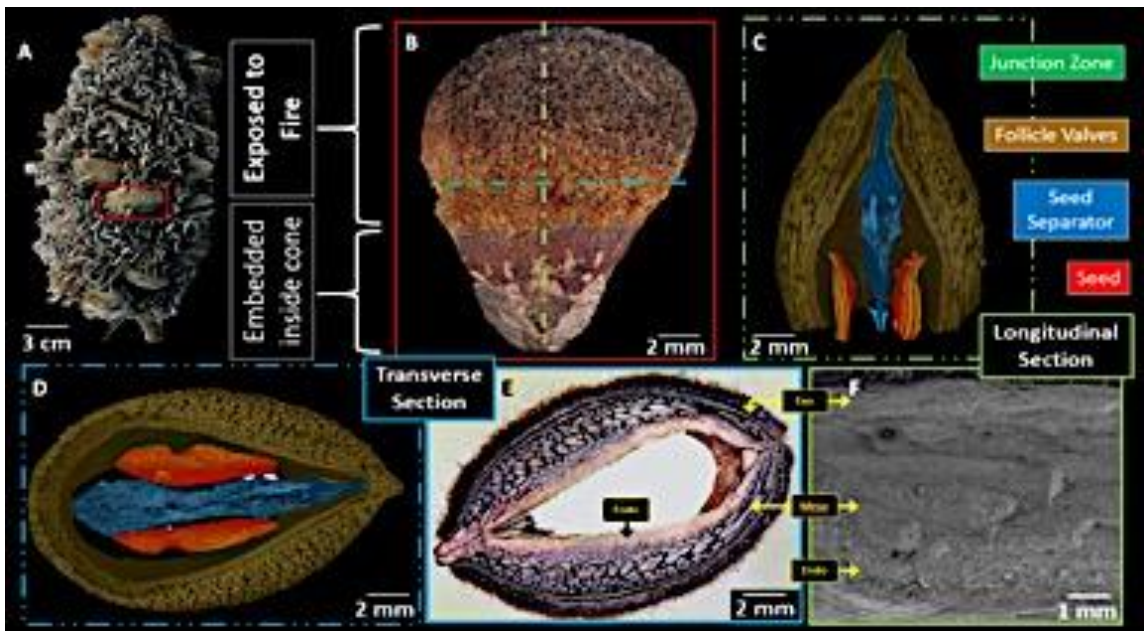
Figure 2.1. [A] Overview of the *B. speciosa* cone with follicles surrounded by remnant flowers; [B] Optical micrograph of a closed *B. speciosa* follicle; blue and green dashed lines denote the transverse and longitudinal sections respectively; [C] & [D] False colored computed tomography [CT] scans of the longitudinal [C] and transverse [D] sections as denoted in [B]; [E] Polished transverse cross-section of the follicle valve as indicated in [B]; [F] Scanning electron micrograph of a fractured longitudinal cross-section of the follicle valve highlighting the exo-, meso- and endo-carp regions.

2.2 Objectives and Hypothesis:

Nature has evolved sophisticated strategies to synthesize organic fibers in hierarchically structured bio-composites with superlative damage tolerance and environmental resistance [14]. I have identified a pyrophytic Australian plant genus, the

Banksia, whose woody follicle valves form a hard cuticle protecting the encapsulated seeds from prolonged exposure to fire until proper environmental conditions are met to allow for seed release. In addition, these tough follicle valves form a hard cuticle that protects the seeds from pecking and boring predators. I propose to leverage these features to design materials offering thermal and mechanical protection, as well as flexibility and reduced weight.

2.3 Experimental Methods and Results:
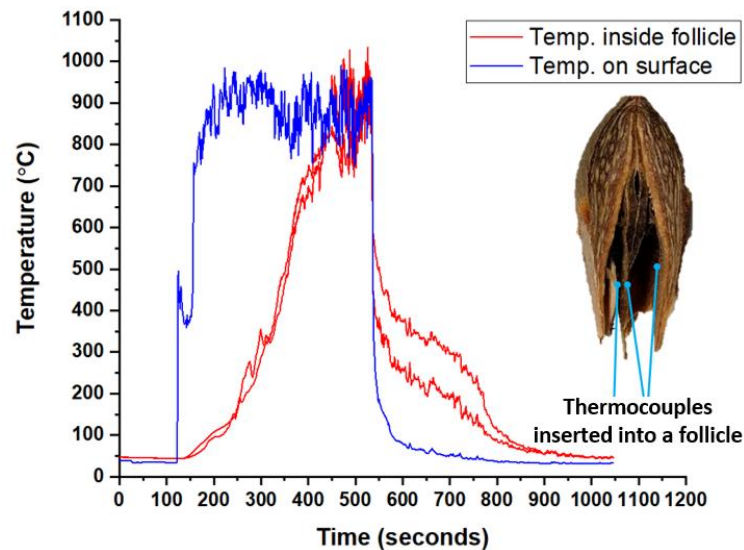
Figure 2.2. Experimental results from the vertical burner set-up at the USDA Fire Lab facility. Fresh *B. speciosa* follicles embedded in pyro-putty were exposed to flames from a vertical burner set-up for up to 10 minutes. The plot in blue is temperature data obtained using thermocouples attached to the surface of the follicle, directly exposed to flames of up to 1000°C. The plot in red is temperature data obtained using thermocouples attached to the seeds encapsulated in the follicles.

Through a combination of microscopy, spectroscopy, and diffraction techniques, I discovered that the follicles feature a tri-layered architecture, which is a huge departure from the consistent cellular microstructure in common construction wood. Furthermore, each of the three layers feature distinct architectural elements and material constituents. This structural anisotropy and chemical heterogeneity at multiple length scales (mm to nm) resulted in greater thermal conductivity (by an order of magnitude) along the external surface of the follicles as opposed to through-thickness heat transport, as revealed by bulk thermal analysis as well as vertical burner/thermal imaging at the USDA Fire Lab (Riverside, CA), see Figure 2.2. Through correlated site-specific synchrotron texturing analysis (micro-diffraction) conducted at ALS and BNL, it was determined that fiber rotation angles and crystallinity gradients enable this anisotropy in thermal transport.

2.4 Analyses and Discussion

An interesting adaptation by the plant involves synthesizing a layer of dense insulating crystalline carbon at temperatures less than 400°C. This is likely made possible by a mechanism called intumescence, which involves the outward expansion of the peripheral layer of the follicle upon heating. I hypothesize that the presence of a reducing atmosphere in the intumescent bubble leads to the formation of oriented Carbon-8, a dense insulating isotope, a possible precursor to graphite at ~400°C. Wood-based materials have been shown to not lend themselves to graphite formation, even at high temperatures [15]–[17]. Thus, intumescence and the underlying polymeric evolution

causing low temperature graphite formation is an important discovery with potential templates for generating multi-modal graphitic thermal coatings.

2.5 Conclusions and Future Perspectives

To summarize, from 8/01/2016 to 10/30/2019, I carried out a thorough investigation into the ultrastructure (macroscale to microscale) of the *Banksia* follicle-seed system and studied the bulk thermal conductivity properties of the follicle. Based on my experimental observations, I strongly suggest that structural anisotropy & chemical heterogeneity within the follicle valve delays heat conduction/flame propagation through to the seed, allowing for the seeds to survive bushfire spreads for prolonged time periods. I identify three unique heat dissipating strategies in the follicle-seed system, as outlined below.

When exposed to flames, the lipid layer of the exocarp undergoes an endothermic phase transition. Intumescence of the exocarp is then observed, which creates expanded "bubbles" that may possibly contain furfural. These bubbles may serve two important functions - (i) the creation of a geometric discontinuity, which inhibits thermal transport by conduction, and likely generates a modified conduction-convection regime, slowing down heat flow; and (ii) the creation of inert micro-environments that prevent the oxidation of the underlying organic matter in the mesocarp, and instead convert it to layers of crystalline "char". This increases the insulation capability of the follicle at high temperatures. As a final line of defense, the presence of calcium oxalate mineral platelets

on the surface of the seed likely provides a means to energy absorptive phase transformation protecting the inner seed organic from burning/high heat.

There are still important gaps to fully understand the fundamental mechanisms that yield extraordinary performance of the follicles under critical thermal loading conditions. The role of the individual constituents, their thermal (as well as mechanical) behavior at the micro/nano scale, and their geometrical arrangement and interfacial properties are unknown. A concerted effort to reduce complexity of these systems and understand the design of lightweight thermally resistant structural materials needs to be implemented.

In order to better understand the effects of each structural inhomogeneity in this system (microstructural, elemental, phase, molecular), I focus the rest of my dissertation on less complicated material systems such as metallic systems and polymeric/metal nanocomposite systems to gauge thermal transport mechanisms at the nanoscale. I will implement learnings from these next few chapters and revisit this problem to make much more definitive conclusions and design biomimetic materials for use in thermally hostile environments.

Chapter 3.

Ultrafast Demagnetization Dynamics in Ferromagnetic Co-Fe Alloys

3.1 Introduction

Laser excitation of a magnetic metal causes energy to cascade from photoexcited electrons into spin and vibrational degrees of freedom[18]–[20]. In ferromagnetic 3d transition metals such as Fe, Co, and Ni, the rapid increase in thermal energy stored by spin degrees of freedom causes femtosecond quenching of the magnetization[19], [20], followed by a partial recovery over the next few picoseconds. Subsequently, on nanosecond timescales, a temperature induced change in equilibrium properties causes oscillatory precessions of the magnetic moment.

Both ultrafast and precessional magnetization dynamics involve energy exchange between magnetic and vibrational degrees of freedom. This energy exchange is mediated by quasi-particle interactions. The strength of quasi-particle interactions in a ferromagnet depends on electronic band structure[21], [22]. In 3d ferromagnetic alloys, the electronic energy bands near the Fermi-level vary strongly with composition[1]. Several recent investigations of nanosecond precessional dynamics in ferromagnetic alloys have explored the relationship between electronic band structure, quasi-particle interactions, and magnetic damping[1]–[3]. Schoen *et al.* report an intrinsic damping parameter less than 10^{-3} for $Co_{0.25}Fe_{0.75}$[1], which is uncharacteristically low for a metal. They attribute the low damping in $Co_{0.25}Fe_{0.75}$ to a minimization in the density of states at the Fermi-level, which decreases the rate of electron-phonon scattering.

Researchers have not yet reached a unified understanding of how quasi-particle interactions govern the magnetization dynamics in the femtosecond regime[19], [23]–[29]. Some studies have hypothesized that spin-flips caused by electron-phonon interactions are key drivers of femtosecond magnetization dynamics[23], [25]. Other experimental and theoretical studies have explored the importance of electron-magnon interactions[26]–[29]. Encouraged by the recent advances in the materials science of nanosecond precessional dynamics[1]–[3], we study the compositional dependence of ultrafast magnetization dynamics in Co-Fe alloys. The goal of our investigation is to understand and characterize the relationship between electronic band structure, quasi-particle interactions, and femto-magnetism properties of ferromagnetic metal alloys.

We perform time-resolved magneto optic Kerr effect (TR-MOKE) measurements to characterize the magnetization dynamics of thin $Co_x Fe_{1-x}$ alloy films on femto- to nanosecond timescales. We observe that the ultrafast magnetization dynamics are a strong function of Co-concentration, see Figures. 3.3. and 3.4. The ultrafast dynamics of $Co_x Fe_{1-x}$ differ most significantly from those of Co and Fe at a composition of $x = 0.25$. We also analyze the time-resolved macroscopic precessional dynamics and report the effective damping parameter of our samples, see Figures 3.5. and 3.6. After linewidth analyses, for $Co_x Fe_{1-x}$, we observe that the Gilbert damping parameter varies from 3.6×10^{-3} to 5.6×10^{-3} for compositions between $x = 0$ and 1, with a minimum value of 1.5×10^{-3} at $x = 0.25$, in good agreement with previously reported results, as is shown in Figure 3.9. (b).

To determine the strength and compositional dependence of electron-magnon and electron-phonon quasi-particle interactions, we analyze our ultrafast magnetization dynamics data with a Three Temperature Model (3TM)[19],[30]. Our results reveal a strong compositional dependence of the electron-phonon energy transfer coefficient, g_{ep}, suggesting that the variation in the ultrafast dynamics in Co_xFe_{1-x} alloys occurs primarily due to electron-phonon scattering. We draw this conclusion because the value of g_{ep} depends on the rate of phonon emission by hot electrons [31]. Electron-phonon scattering is also predicted to govern the damping of nanosecond precessional dynamics [1], [32], [33]. Therefore, our results demonstrate that the same microscopic electron-phonon interactions responsible for Gilbert damping also play an important role in femto-magnetism properties of ferromagnetic alloys.

3.2 Materials and Methods

Sample Preparation: We sputter deposit Co-Fe samples onto sapphire substrates with a direct current (DC) magnetron sputtering system (Orion, AJA International). The base pressure prior to deposition is less than 3.5×10^{-7} torr. We sputter with an Argon pressure of ~3.5×10^{-3} torr. The geometry of our thin film samples is sapphire / Ta(2nm) / Cu(3nm) / Co_xFe_{1-x}(15nm) / Cu(3nm) / Ta(1nm). The Co_xFe_{1-x} layer is deposited by co-sputtering two 4N purity Co and Fe targets at different powers. We chose this film geometry to mimic the samples in Ref.[1] which demonstrated low damping at $x = 0.25$.

To ensure an accurate thickness of each layer in our samples, we calibrate the deposition rates of each metal by sputtering individual Co, Fe, Ta, and Cu films onto

SiO$_2$/Si substrates and/or BK-7 glass substrates. We use picosecond acoustics[34] and time-domain thermo-reflectance (TDTR) measurements[35], [36] to determine the thicknesses of these individual films. We verify the composition of the Co-Fe alloy layer by performing Energy Dispersive X-Ray Spectroscopy (EDS) analyses with a scanning electron microscope (FEI Nova NanoSEM 450) at an operating voltage of 15 kV and working distance of 14 mm. We analyze the EDS data using Aztec Synergy software (Oxford Instruments).

Time-Resolved MOKE Experimental Setup: We use a pump/probe laser system to perform TR-MOKE measurements of the magnetization dynamics. The pulsed laser is a Ti:sapphire oscillator with an 80 MHz repetition rate. The laser beam is split into a pump and probe beam, that are modulated to frequencies of 10.7 MHz and 200 Hz, respectively. A time-delayed pump beam irradiates the sample surface and heats the metal film. The ultrafast heating causes a change in the magnetic moment. We measure the time-evolution of the magnetic moment by monitoring the polarization of the probe beam reflected off the sample surface. The reflected probe beam's polarization state is affected by the out-of-plane magnetic moment of the sample due to the polar Kerr effect. A schematic is shown in Figure 3.1. Additional details about the MOKE experiment set-up are in Ref.[37].
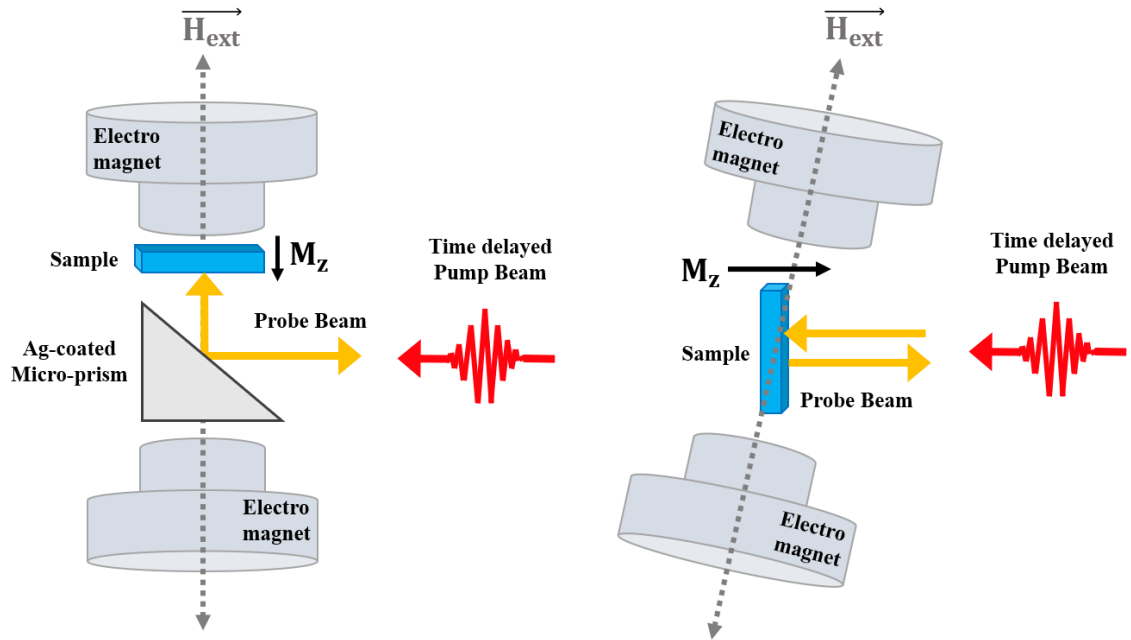
Figure 3.1. Experimental setup to measure TR-MOKE in a polar-configuration. (a) To measure the ultrafast magnetization dynamics, we apply an external magnetic field H_{ext} perpendicular to the plane of the sample. We direct the pump and probe beams to the sample surface using an Ag-coated micro-prism. The out-of-plane magnetization component, M_z is detected by the probe beam. **(b)** We measure precessional dynamics in our samples by tilting the electromagnet by 11°, such that H_{ext} is canted. Upon photoexcitation from the pump pulse, the out-of-plane magnetic moments precess to a new equilibrium orientation, as a result of a net torque imbalance between H_{ext} and the in-plane shape anisotropy of the sample.

The time-resolution of our experiment is controlled by the convolution of the intensity vs. time of the pump and probe pulses. The wavelength of our pump and probe beams is tunable. Employing a red (900 nm) pump and blue (450 nm) probe yields higher time-resolution capabilities, allowing us to accurately measure the ultrafast magnetization at femtosecond time delays. We measure the full-width-at-half-maximum (FWHM) of the convolution of the pump and probe pulses by performing an inverse Faraday effect (IFE) measurement on Pt. We obtain a FWHM value of 390 fs for the convoluted pulses, and a pulse duration of 210 fs for the 900 nm pump/450 nm probe beam setup. We fit the

16

IFE dataset with a sech^2-shaped pulse. For further details on our IFE measurements and pulse duration calculations, please refer to Figure 3.2.
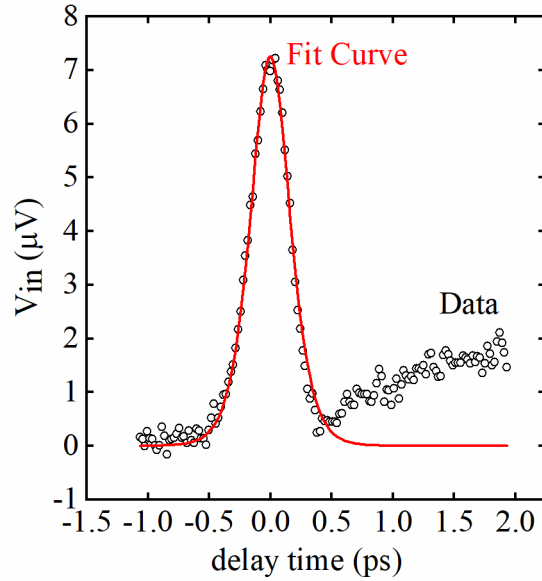
Figure 3.2. Determining the pulse duration on the red (880 nm) pump and blue (440 nm) probe TR-MOKE setup via the inverse Faraday effect. The in-phase TR-MOKE signal obtained on a 20 nm Pt/sapphire sample is shown in open black circles, as a function of delay time. Platinum was chosen to measure the pulse duration on account of its strong electron-electron coupling. This dataset was fit using the $Y = a \times \text{sech}\,((x - b)/c)^2$ function, where a is the amplitude, b is the time-shift to match the experimental data, and c is the pulse duration. The fit is indicated in a red solid line, yielding a pulse duration value of 210 fs.

To investigate the precessional dynamics on longer timescales, we use a pump and probe wavelength of 783 nm. The pulse duration for this setup is 610 fs due to pulse broadening from a two-tint setup we use to prevent pump light from reaching the balanced detector[37], [38].

17

Three Temperature Modeling: To determine the electron, phonon, and magnon energy transfer coefficients, we use the phenomenological Three Temperature Model (3TM), given by the following set of equations:

$$C_e \frac{dT_e}{dt} = g_{ep}(T_p - T_e) + g_{em}(T_m - T_e) + \Lambda_e \frac{d^2 T_e}{dz^2} + S(z,t) \qquad (1)$$

$$C_p \frac{dT_p}{dt} = g_{ep}(T_p - T_e) + \Lambda_p \frac{d^2 T_p}{dz^2} \qquad (2)$$

$$C_m \frac{dT_m}{dt} = g_{em}(T_m - T_e) + \Lambda_m \frac{d^2 T_m}{dz^2} \qquad (3)$$

$$S(z,t) = S_0 P(t) A(z) \qquad (4)$$

Equations 1 – 3 describe the temperature evolution of electrons (*e*), phonons (*p*) and magnons (*m*), as a function of time delay (*t*). *C*, *T*, and Λ are the heat capacity per unit volume, temperature, and thermal conductivity, respectively. We use the density of states (DOS) at the Fermi level as a function of Co-concentration[1] to calculate the electronic heat capacity (C_e) using the Sommerfeld model. We assume that the phonon-magnon energy transfer is negligible compared to electron-magnon coupling, and thus, neglect g_{pm}.

We calculate the laser energy absorption by electrons (*S*), as a function of depth (*z*) and time delay (*t*), as described in Equation 4. The terms *P(t)* and *A(z)* denote the time-dependent laser pulse intensity and the optical absorption profile as a function of stack thickness. We calculate *A(z)* using the refractive indices of each metal constituent of the stack[39]–[41].

3.3 Results and Discussion

3.3.1 Ultrafast Magnetization Dynamics

We plot the normalized ultrafast magnetization dynamics response, $\Delta M(t)$, for Co, Fe, and $Co_{0.25}Fe_{0.75}$ as a function of time delay in Figure 3.3. (a). Data for the rest of the Co-Fe compositions are plotted in Figure 3.4. All our measurements were performed with an incident laser fluence less than ~15 J/m^2. This is a sufficiently small fluence for the dynamics in our experiments to follow a linear regime. In other words, decreasing the incident fluence by a factor of two decreases the optical signal by a factor of two, but does not change the time-dependence of the signal.

We use a polar TR-MOKE configuration to measure the ultrafast magnetization dynamics at femtosecond time delays. A schematic of our experimental setup is shown in Figure 3.1. We apply an external 2.2 Tesla (T) field perpendicular to the plane of the sample using an electromagnet (GMW 3480). This external field is strong enough to effectively overcome the in-plane shape anisotropy of the Co-Fe alloys and saturate the moment in the out-of-plane direction. Since the equilibrium orientation of the moment is in the out-of-plane direction, both, before and after laser irradiation, this geometry allows us to quantify the femtosecond demagnetization response of the Co-Fe alloys, without the presence of macroscopic precessional dynamics, see schematic in Figure 3.3. (b).
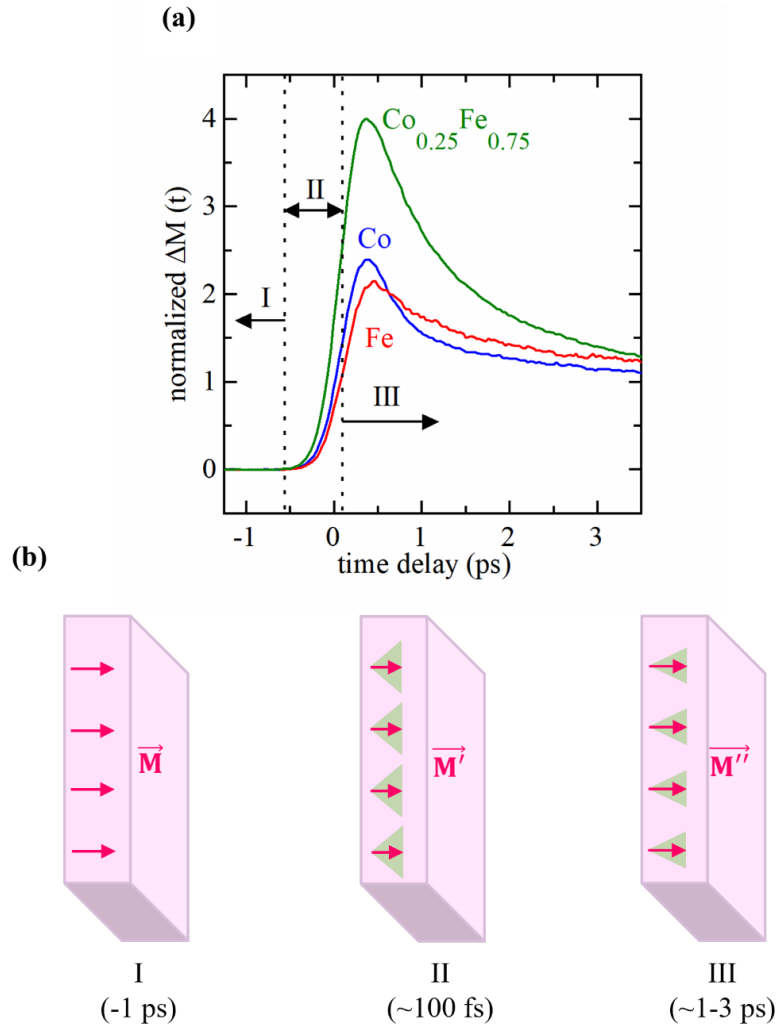
Figure 3.3. Ultrafast magnetization dynamics of Co, Fe, and Co$_{0.25}$Fe$_{0.75}$ thin films (a) Polar TR-MOKE data showing ultrafast demagnetization behavior at short delay times. **(b)** Schematic illustration of the three phases of an ultrafast magnetization dynamics experiment.
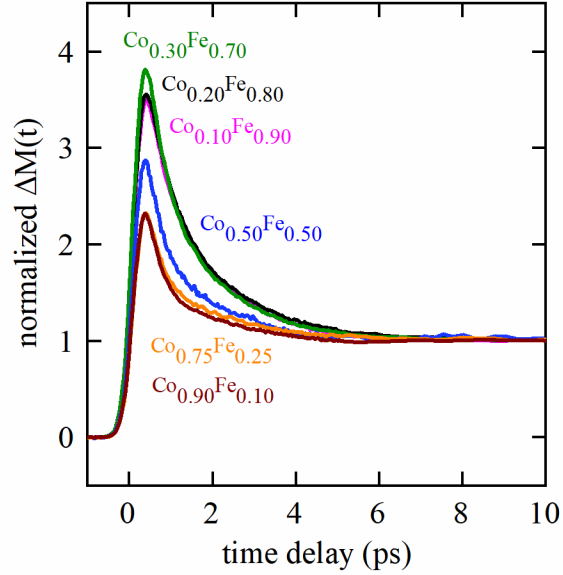
Figure 3.4. Ultrafast magnetization in thin film Co-Fe alloys. Normalized signal from polar TR-MOKE scans of $Co_{0.90}Fe_{0.10}$, $Co_{0.75}Fe_{0.25}$, $Co_{0.50}Fe_{0.50}$, $Co_{0.30}Fe_{0.70}$, $Co_{0.20}Fe_{0.80}$, and $Co_{0.10}Fe_{0.90}$ alloys are plotted, at short delay times. The ultrafast dynamics in Co-concentrations close to 25% are distinctly different from the rest of the Co-Fe alloys.

Upon excitation with the pump pulse, the magnetic moment decreases on a sub-picosecond timescale due to the flow of energy from electrons to magnons[19], [20], [30], [42], [43]. Then, on picosecond timescales, the magnetization partially recovers as energy is transferred to the lattice and temperature gradients across the film thickness relax. After a few picoseconds, the magnetic film reaches a new equilibrium at an elevated temperature. Ultrafast dynamics with sub-picosecond demagnetization followed by picosecond re-magnetization are commonly categorized as "type I" dynamics, and are characteristic of 3d ferromagnetic metals such as Fe, Co, and Ni[23].

To elucidate how the de- and re-magnetization dynamics change with composition, we define two data descriptors: τ_D and R. We define the demagnetization time, τ_D, as the delay time where $d\Delta M(t)/dt$ reaches its maximum value. We define R as the ratio of the maximum of $\Delta M(t)$ to $\Delta M(t \approx 10\text{ps})$. We plot τ_D and R as a function of composition in Figure 3.9 (a). τ_D varies weakly with composition and has a minimum value of 40 fs at $x = 0.25$. In contrast, we observe that R varies strongly with composition and is a maximum of 4 at $x = 0.25$.

3.3.2 Nanosecond Precessional Dynamics

We show measurements of the macroscopic precessional dynamics of Fe, Co, and $Co_{0.25}Fe_{0.75}$ in Figure 3.5 (a). Data for the other Co-Fe compositions are plotted in Figure 3.6. We use a polar TR-MOKE experimental setup, with an obliquely angled external magnetic field, to measure the macroscopic precessional dynamics of our samples. A schematic of our experimental setup is shown in Figure 3.1. Tilting the electromagnet to an angle of 11°, with respect to the plane of the sample, allows us to apply a canted external magnetic field so that the magnetic moment has an out-of-plane component. The equilibrium orientation of the moment depends on the balancing between the applied external field and the thin-film shape anisotropy field. The shape anisotropy field in the z-direction is proportional to the out-of-plane component of the magnetic moment. Upon heating, the total magnetic moment decreases. This decrease results in an ultrafast change to the out-of-plane anisotropy field and equilibrium orientation. As a result, the magnetic moment will precess to a new equilibrium orientation, see schematic in Figure 3.5 (b).

Our polar TR-MOKE setup detects changes in the out-of-plane moment, so we can sensitively measure the frequency and amplitude of the precessional dynamics.

We collect between 6 and 12 TR-MOKE scans of precessional dynamics for each sample. Each of these scans is collected with a different applied external magnetic field, ranging from 0.2 T to 2.2 T. The TR-MOKE signals include precessional dynamics in addition to a background related to temperature-induced demagnetization. To analyze the precessional dynamics, we subtract the background with a biexponential decay function. We fit the resulting dataset with a damped harmonic function, $V(t) = A\sin(\omega t + \emptyset)\exp(-t/\tau)$. Our fits yield unique values of A (amplitude), $\emptyset$ (the initial phase of the oscillation), T (period), and τ (the exponential decay time of the precession). Using these values, we determine the effective dimensionless damping parameter, $\alpha_{eff} = \omega.\tau^{-1}$.
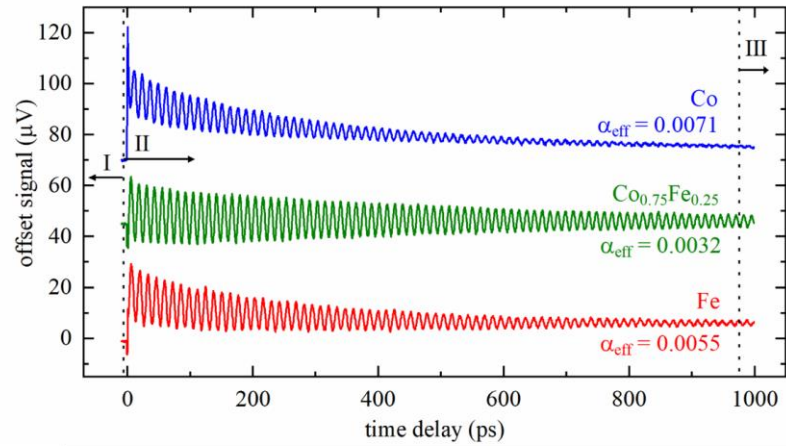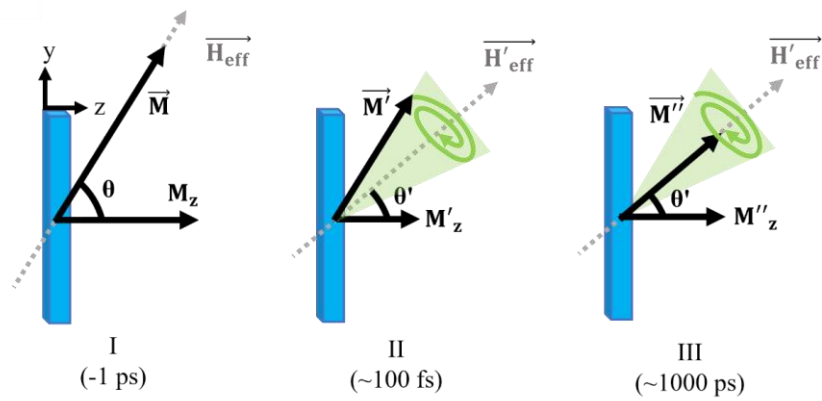
Figure 3.5. Precessional dynamics in Co, Fe, and $Co_{0.25}Fe_{0.75}$ thin films (a) Polar TR-MOKE data on sub-nanosecond timescales. (b) Illustration of the three stages for precessional dynamics after laser excitation.
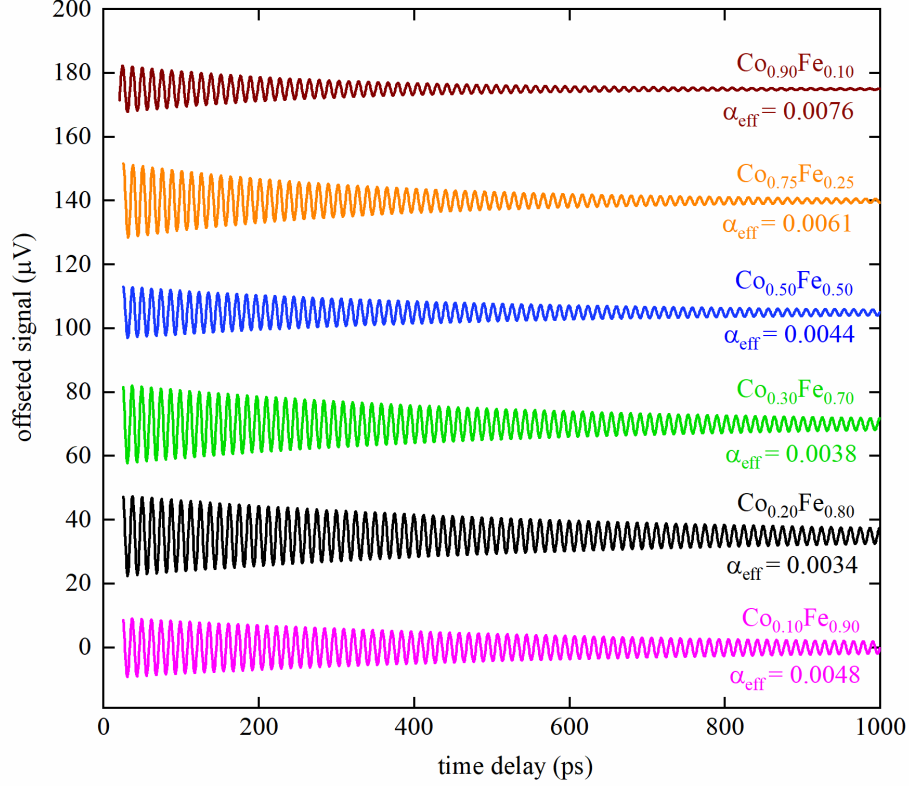
Figure 3.6. Precessional dynamics in thin film Co-Fe alloys. Offset polar TR-MOKE signals of $Co_{0.90}Fe_{0.10}$, $Co_{0.75}Fe_{0.25}$, $Co_{0.50}Fe_{0.50}$, $Co_{0.30}Fe_{0.70}$, $Co_{0.20}Fe_{0.80}$, and $Co_{0.10}Fe_{0.90}$ alloys, are plotted after background subtraction with a biexponential decay function. The lifetime of the magnetic precessions at compositions close to $Co_{0.25}Fe_{0.75}$ are longer than the others.

The resonance frequency is a function of applied external magnetic field and magnetic moment, $\omega = \gamma \sqrt{\frac{H_{eff}}{\mu_0} (\frac{H_{eff}}{\mu_0} + \mu_0 M_s)}$. Here, γ is the gyromagnetic ratio, μ_0 is the vacuum permeability, H_{eff} is the out-of-plane component of the external magnetic field as measured by a Hall probe, and M_s is the saturation magnetization of the sample. We derive the magnetic moment of the sample by treating M_s as a fit parameter. We also

perform VSM measurements of the moment of some of the samples and find that the

magnetic moment obtained is in good agreement with the value that we derive by fitting

our precessional dynamics data. See Figure 3.7 for more details.
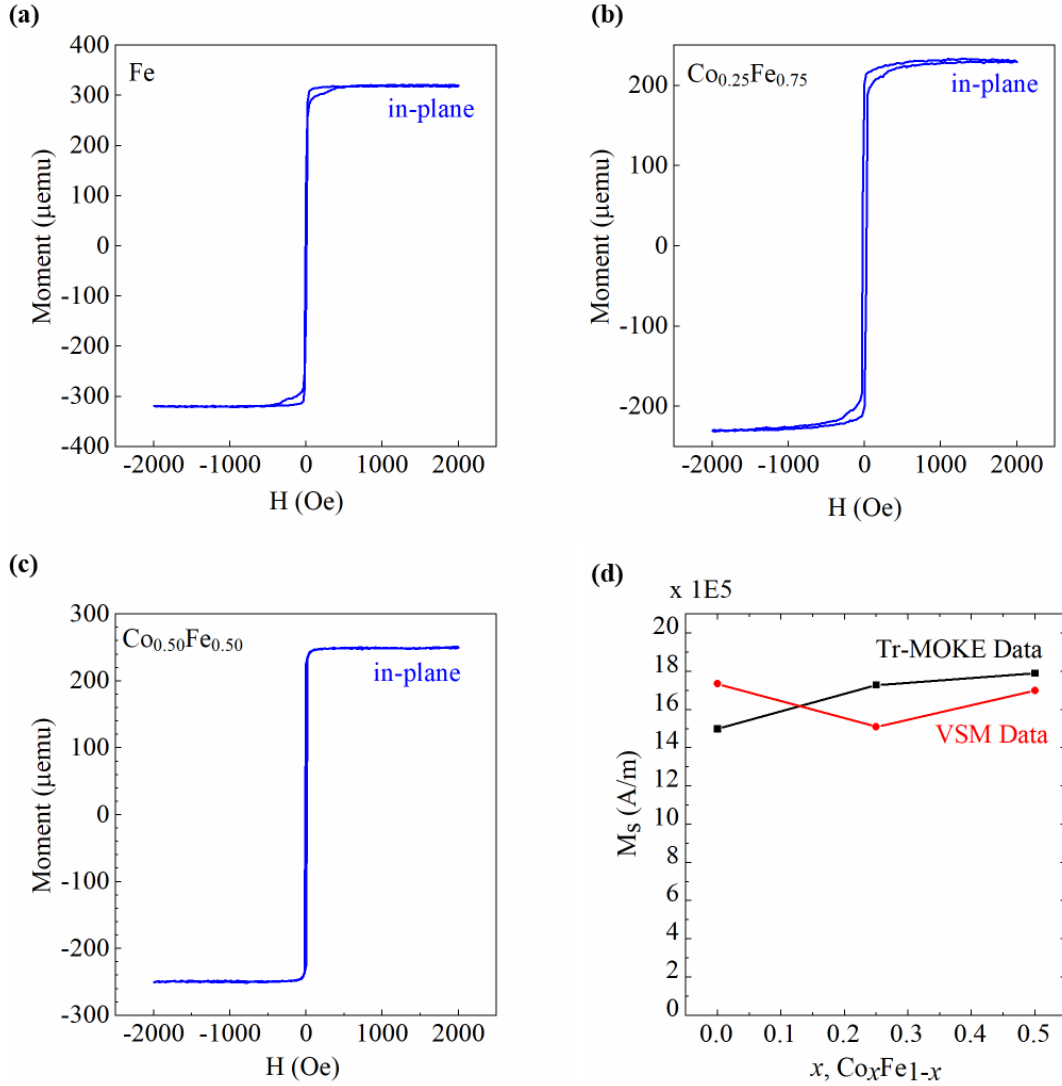
Figure 3.7. Magnetometry on Co-Fe alloys to determine the saturation magnetization (M_s).
We measured the in-plane magnetic moments of three alloy samples (a) Fe, (b) $Co_{0.25}Fe_{0.75}$, and
(c) $Co_{0.50}Fe_{0.50}$, using a vibrating-sample magnetometer (VSM). (d)We find that the M_s values
obtained are in good agreement with the values we obtain by fitting the resonance frequency of
the TR-MOKE data with the Kittel equation $\omega = \gamma \sqrt{\frac{H_{eff}}{\mu_0}(\frac{H_{eff}}{\mu_0} + \mu_0 M_s)}$.

The effective damping parameter α_{eff} that we deduce from our precessional dynamics measurements includes effects from damping and inhomogeneous broadening. The effect of inhomogeneous broadening is independent of the applied field at high frequencies[44]. After performing linewidth calculations, we extract the Gilbert damping parameter, (α), which still includes effects from spin-orbit coupling, etc. These effects are a function of sample geometry, adjacent metals in the stack, etc. Thus, the Gilbert damping parameter is not an intrinsic material property. In order to obtain the intrinsic damping parameter, α_{int}, we'll need to systematically evaluate the effects of spin-pumping from adjoining layers, thickness dependence of α, etc. We have not performed these measurements in this study, and thus, only report α.

To obtain the Gilbert damping parameter intrinsic to the sample geometry, we plot the effective linewidth, $\alpha_{eff} \cdot f$, as a function of frequency, and linearly fit to the equation, $\alpha_{eff} \cdot f = \alpha \cdot f + \Delta H$, where ΔH is the inhomogeneous broadening component and α is the Gilbert damping parameter. Further details can be found in Figure 3.8.
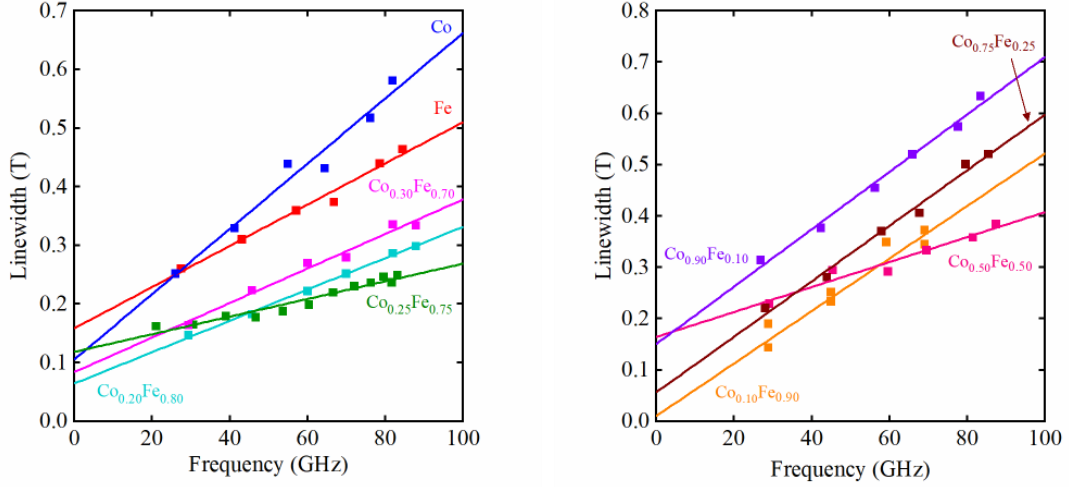
Figure 3.8. Determining the linewidth of the Co-Fe alloys from TR-MOKE data. To extract the Gilbert damping parameter, we plot the linewidth ($=\alpha_{eff} \cdot f$), as a function of frequency, where α_{eff} is the effective damping parameter and the f is the frequency. We linearly fit these datasets using the equation $\alpha_{eff} \cdot f = \alpha \cdot f + \Delta H$, where ΔH is the inhomogeneous broadening component, and α is the Gilbert damping parameter. (a) shows linewidth analyses of Co, Fe, and alloys with Co-concentration close to $Co_{0.25}Fe_{0.75}$, whereas (b) shows the linewidth for the rest of the Co-Fe alloys plotted.

In contrast to prior investigations that performed FMR measurements in the frequency range from 16-18 GHz[2] and 40 GHz[1], our TR-MOKE experimental setup allows us to study dynamics at frequencies as large as 90 GHz. At such high frequencies, we can be confident that our measured Gilbert damping parameter is dominated by the intrinsic linewidth over inhomogeneous broadening effects.

The Gilbert damping parameter we observe of α = 1.5×10^{-3} for $Co_{0.25}Fe_{0.75}$ is amongst the lowest ever reported for a ferromagnetic metal. Schoen et al. report α = 2.1×10^{-3} for $Co_{0.25}Fe_{0.75}$. After accounting for radiative and spin-pumping contributions, they estimate an intrinsic damping parameter for $Co_{0.25}Fe_{0.75}$ to be $\alpha_{int} =$

28

5×10^{-4} . Lee et al. [2] performed FMR measurements of $Co_{0.25}Fe_{0.75}$ epitaxial films and report $\alpha = 1.4 \times 10^{-3}$. Wei et al. report $\alpha = 1.5 \times 10^{-3}$ for $Fe_{0.75}Al_{0.25}$ films [3]. We note that our measured damping parameter likely includes significant contributions from spin-pumping into the adjoining Ta/Cu layers, but we did not experimentally examine the effects of spin-pumping in our samples.

The comparison of R and α in Figure 3.9 and Figure 3.10 reveals that the two quantities depend on composition in a similar manner. R is at a maximum and α is at a minimum at $x = 0.25$. Fe and Co_xFe_{1-x} alloys with $x \geq 0.5$ have small R and high α. Alternatively, Co_xFe_{1-x} alloys with $0.1 < x < 0.5$ have both high R and low α. To confirm this correlation, we performed a hierarchical cluster analysis of the raw data at both femtosecond and nanosecond timescales. The clustering algorithm divides the Co-Fe alloys into groups based on similarities in the dynamics data. The clustering results as a function of composition are similar when based on the femto-/pico-second timescale data vs. the nanosecond timescale data.
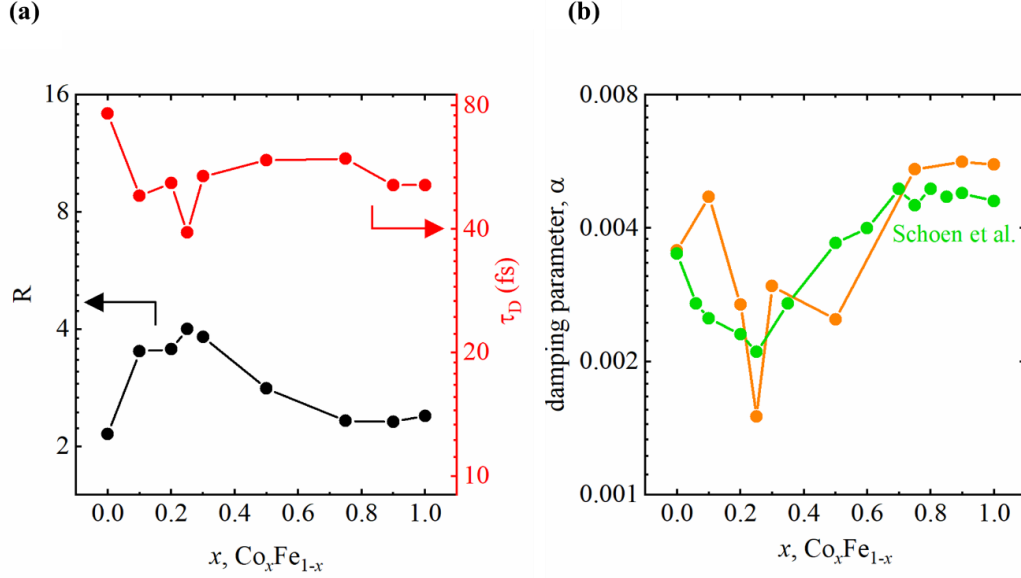
Figure 3.9 Compositional dependence of descriptors for the TR-MOKE experimental data.
(a) In the femtosecond regime, R describes the maximum change in the magnetic moment, i.e. how far from equilibrium spin-degrees of freedom are driven after ultrafast excitation. τ_D describes the lag between zero delay time and demagnetization, as a function of Co-concentration. **(b)** In the nanosecond regime, α denotes the Gilbert damping parameter, as a function of Co concentration. Data obtained from our TR-MOKE experiments described in this study (plotted in orange), agree reasonably with data from Ref. [6] (plotted in green). $Co_{0.25}Fe_{0.75}$ features the largest deviation in R and α, when compared to its constituent elements Co and Fe.

We now explain the correlation between ultrafast and precessional dynamics by considering how electronic scattering processes depend on composition. Similar to prior studies of damping in Co-Fe alloys[1], [3], [45], our results for α vs. x are in good agreement with the "breathing Fermi surface" model for damping[46]. In this model, spin-orbit coupling causes the Fermi-level to shift with the precessions of the magnetic moment[47]. A shift in the equilibrium Fermi-level leads to a nonequilibrium electron population. As the Fermi-level repopulates, intra-band electron-phonon scattering transfers energy to the lattice. The "breathing Fermi surface" model predicts that the

damping parameter is directly proportional to $D(\varepsilon_f)$, because more electronic states near ε_f leads to higher rates of electron-phonon scattering. We observe that the α value for $Co_{0.25}Fe_{0.75}$ is ~2.5x lower than α for Fe. Density functional theory predicts a ~2x difference in $D(\varepsilon_f)$ for $Co_{0.25}Fe_{0.75}$ vs. Fe, see Ref. [1]. Therefore, like prior studies of Co-Fe alloys[1], [3], [45], our data is consistent with the hypothesis that intra-band electron-phonon scattering governs precessional damping.
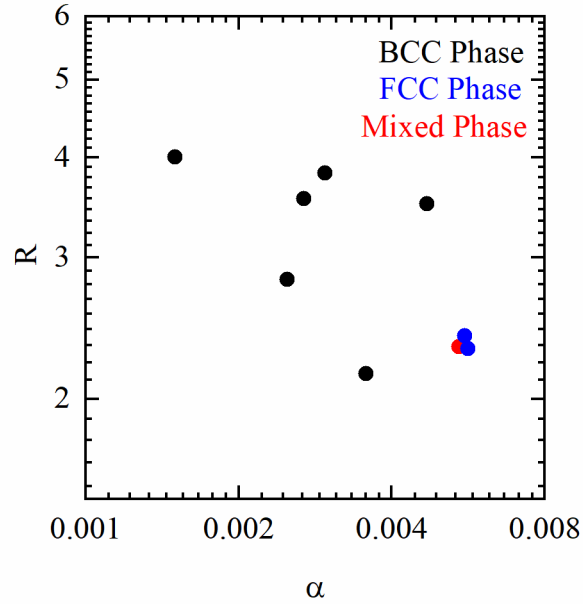
Figure 3. 10. Comparison of TR-MOKE Descriptors at the Femtosecond and Nanosecond Regimes Our plot shows a weak inverse relationship between R and α. We also represent the phases of the Co_xFe_{1-x} thin films as referenced in [1]. Co-Fe alloys that feature bcc phase (i.e., higher Fe concentration) appear to show higher R and smaller α. The fcc and mixed phase alloys have higher Co-concentrations and show relatively low R values and higher α.

3.3.3 Three Temperature Modelling

To better understand how composition affects electron-magnon and electron-phonon energy transfer mechanisms, we analyze our $\Delta M(t)$ data with a phenomenological Three Temperature Model (3TM), see Figure 3.11. The 3TM describes how heat flows between electrons, phonons, and magnons after laser excitation of the Co-Fe sample. The 3TM predicts that τ_D depends on two groupings of model parameters: $\tau_{em} \approx C_m/g_{em}$ and $\tau_{ep} \approx C_e/g_{ep}$. Here C_m and C_e are the magnon and electron heat-capacity per unit volume, and g_{em} and g_{ep} are the energy transfer coefficients from electrons to magnons and phonons, respectively. We estimate values for C_e vs. composition using the Sommerfeld model together with the electronic density of states vs. composition reported in Ref.[1]. The 3TM also predicts that the parameter R is determined by the following grouping of parameters: $R = C_p g_{em}/C_m g_{ep}$ [30], where C_p is the phonon heat-capacity per unit volume. We assume that the value of C_p is 3.75 MJ m^{-3} K^{-1} for Co, Fe and Co-Fe alloys. With these estimates for C_e and C_p, and other relevant model parameters, we can deduce unique values for C_m/g_{em} and C_p/g_{ep} as a function of composition from our TR-MOKE data, see Figure 3.11 (b).
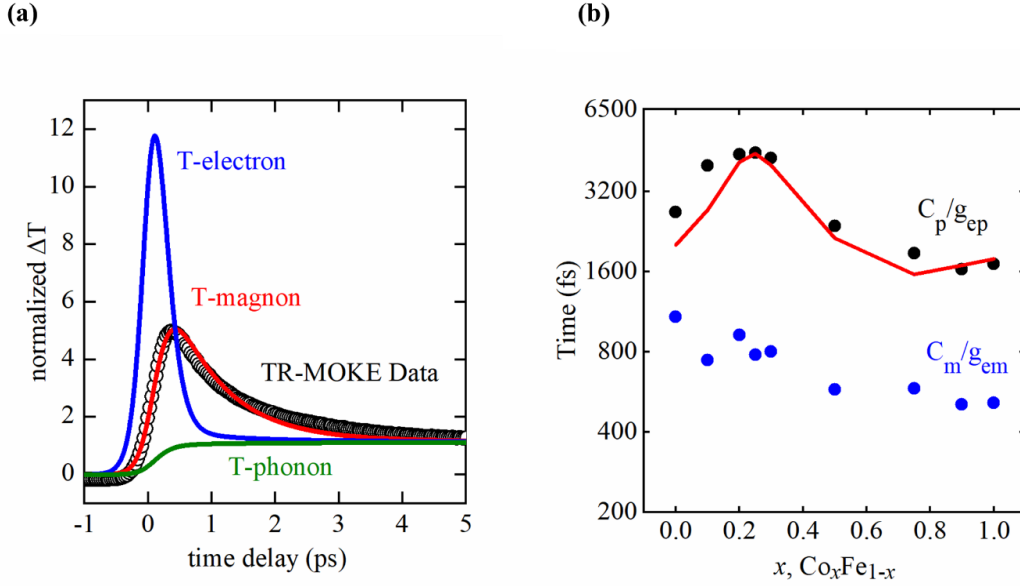
Figure 3. 11. Analyses of Ultrafast Demagnetization Results using the Three Temperature Model (3TM) in Co-Fe alloys. **(a)** Polar TR-MOKE dataset of the $Co_{0.25}Fe_{0.75}$ composition (black circles) with best-fit results of the 3TM. The 3TM describes the temperature excursions of the electrons (blue curve), magnons (red curve) and phonons (green curve) after laser excitation. **(b)** We treat g_{ep} and g_{em} as fit parameters when solving the 3TM. Using literature values of C_p and C_m, we calculate and plot the electron-phonon (τ_{ep}) and electron-magnon (τ_{em}) relaxation times, as a function of Co-concentration. The red-line is a best-fit value for the electron-phonon relaxation time as a function of composition, with the assumption of a composition-independent value for the electron-phonon coupling parameter λ.

Based on our 3TM analysis, we conclude that the strong composition dependence of R is due to the composition dependence of g_{ep}. Boltzmann rate-equation modelling of the nonequilibrium electron dynamics after photoexcitation predicts that the electron-phonon energy-transfer coefficient is $g_{ep} = [\pi \hbar k_B D(\varepsilon_F)]\lambda\langle\omega^2\rangle$ [22]. Here, $\lambda\langle\omega^2\rangle$ is the second frequency moment of the Eliashberg function and is a measure of the strength of electron-phonon interactions. Most of the compositional dependence we observe in g_{ep} is

explained by the compositional dependence of $D(\varepsilon_f)$. To show this, we include a prediction for g_{ep} in Figure 3.11. (b). Our prediction uses the $D(\varepsilon_f)$ vs. x reported in[1] and treats $\lambda\langle\omega^2\rangle$ as a composition independent fit parameter. We find that $\lambda\langle\omega^2\rangle = 260$ meV^2 provides an excellent fit to our data. The best-fit value for $\lambda\langle\omega^2\rangle$ is in good agreement with $\lambda\langle\omega^2\rangle \approx \lambda_R\,\Theta_D^2/2 = 280$ meV^2. Here, λ_R is derived from electrical resistivity data for Fe [48], and $\Theta_D = 470K$ is the Debye temperature of Fe.

Before beginning our experimental study, we hypothesized that the energy transfer coefficient between electrons and magnons, g_{em}, would be correlated with the phase-space for electron-magnon scattering. We expected the phase-space for electron-magnon scattering to be a strong function of band-structure near the Fermi-level [26]–[29]. We also expected the phase-space to be minimized at a composition of $x = 0.25$, because of the minimum in the density of states at the fermi-level. To explore how the phase-space for electron-magnon scattering depends on composition, we performed density functional theory calculations for the electronic band structure with $x = 0$ and $x = 0.25$. Our DFT calculations suggest that the phase-space for electron-magnon scattering is an order of magnitude higher for $x = 0$ vs. 0.25. However, we do not see evidence that this large theoretical difference in electron-magnon scattering phase-space affects ultrafast dynamics. The timescale for magnons to heat up after photoexcitation, $\tau_{em} \approx C_m / g_{em}$, decreases monotonically with increasing x, and does not display structure near $x \sim 0.25$.

3.3.4. Koopman and Fähnle Model Predictions

Several theoretical models predict a strong correlation between τ_D and α_{int}. For example, Koopmans *et al.* predicts that τ_D will be inversely proportional to α by assuming that the dissipative processes responsible for damping also drive ultrafast demagnetization [49]. Alternatively, Fähnle *et al.* predicts that τ_D should be proportional to α_{int} [50].

Koopman Model: The Koopman model uses quantum-mechanical principles to relate the spin relaxation phenomena at sub-picosecond time scales to the Gilbert damping parameter at nanosecond time delays. Furthermore, the Koopman model utilizes the Elliot-Yafet spin flip scattering mechanisms in two scenarios – i) impurity-induced spin flip scattering, where electrons primarily are scattered by impurities in the system and ii) phonon-mediated spin flip scattering, where electron-phonon interactions drive energy equilibriation between the charge and lattice. Both spin-flip mechanisms yield a similar empirical relationship between α and τ_D, as shown below:

$$\tau_D = \frac{C_0 \hbar}{\alpha k_B T_c}$$

where C_0 is a constant ($=1/4$, if $\tau_D \gg \tau_E$, or $=1/8$, if $\tau_D \ll \tau_E$), $\hbar$ and k_B are the Planck's constant and Boltzmann constant respectively, and T_c is the Curie temperature. τ_E is the recovery time.

Fähnle Model: In 2017, Fähnle et al. published a study on Co-Ni bilayers, where they used TR-MOKE to measure both ultrafast demagnetization dynamics and nanosecond precessions. They systematically varied the thickness of Ni and found that the demagnetization time, τ_D was directly proportional to the Gilbert damping parameter, α with varying Ni thickness. These results were explained using the breathing Fermi-surface model for systems displaying conductivity-type damping. The relationship is shown below:

$$\tau_D = \frac{M}{\gamma F_{el} p b^2} \alpha$$

where M represents the magnetization, b^2 is the Elliot-Yafet spin mixing parameter, p is a material-specific empirical parameter, and F_{el} is derived from an *ab initio* density functional electronic theory calculations. Fähnle also suggested that the inversely proportional relationship indicated in the Koopman model was on account of the resistivity-like damping featured by the Ni thin layer system.

In our experiments on Co-Fe thin films, we observe only a weak correlation between τ_D and α. While α varies with composition by a factor of three, τ_D for 8 of the 9 compositions we study fall within 20% of 75 fs. The τ_D value we obtained for Fe (= 76 fs) agrees well with experimental results reported in [23], [26], [51].

3.4 Conclusions

We have measured the magnetization dynamics of $Co_x Fe_{1-x}$ thin-films, and we observe that both ultrafast and precessional dynamics of $Co_{0.25}Fe_{0.75}$ differ significantly from Co and Fe. When the moment of $Co_{0.25}Fe_{0.75}$ is driven away from its equilibrium

orientation, the timescale over which the precessions occur, and for the moment to return to equilibrium is 3-4x as long as for Fe or Co. Similarly, when magnons in of $Co_{0.25}Fe_{0.75}$ are driven into a nonequilibrium state by ultrafast laser heating, the timescale for thermalization with the lattice is 2-3x as long as for Fe or Co. Through 3TM analyses, we demonstrate that this occurs primarily due to the effect of the electronic band-structure on electron-phonon interactions, consistent with the "breathing Fermi surface" theory. Our findings are of fundamental importance to the field of ultrafast magnetism, which seeks to control magnetic order on femto- to picosecond timescales. Such control requires a thorough understanding of how and why energy is exchanged between electronic, spin, and vibrational degrees of freedom. Prior studies have shown that g_{ep} is correlated with a wide range of physical properties, e.g the superconducting transition temperature[52], electrical resistivity [48], photoelectron emission[53], and the laser fluence required for ablation[54]. To our knowledge, our study provides the first demonstration that g_{ep} in ferromagnetic metals is also correlated to the Gilbert damping parameter α.

Our findings also have implications for the ongoing search for magnetic materials with ultrafast magnetic switching functionality. Atomistic spin dynamics simulations predict that the energy required for ultrafast electrical or optical switching of rare-earth ferromagnetic alloys, e.g. GdFeCo, is governed by the electron-phonon energy transfer coefficient[55]. To date, most studies aimed at exploring the materials science of ultrafast switching have used alloy composition as a way to control magnetic properties [56]–[59]. Our work suggests an alternative strategy for reducing the energy requirements for ultrafast magnetic switching. The alloy composition should be chosen to minimize the

electronic density of states at the Fermi-level. Such metals will have lower electron-phonon energy transfer coefficients, and therefore more energy efficient ultrafast switching [55].

Finally, our findings offer a new route for discovering ferromagnetic materials with ultra-low damping as a result of low g_{ep}. Current methods for identifying low damping materials involve labor-intensive ferromagnetic resonance measurements of one alloy composition at a time. Alternatively, high-throughput localized measurements of ultrafast demagnetization dynamics of samples produced using combinatorial techniques[60] would allow promising alloy compounds with weak electron-phonon interactions to be rapidly identified [61]–[63].

Chapter 4.

Nanoscale Thermal Transport in Co-Fe Alloys

4.1 Introduction

Over the past two centuries, researchers have firmly established the science of thermal and electrical transport in metals and their alloys. Heat and charge currents are mediated by electrons. As a result, thermal and electrical conductivities, Λ_{Total} and σ, are related to each via the following relationship,

$$\Lambda_{Total} = AL_0T\sigma + B. \qquad (1)$$

Here, Λ_{Total} is the total thermal conductivity, L_0 is the Sommerfeld Lorenz number of $2.44 \times 10^{-8} \, W\Omega K^{-2}$, and T is temperature. A and B are phenomenological parameters related to electronic scattering processes and the magnitude of the non-electronic thermal conductivity. The $AL_0T\sigma$ term describes electronic contributions to the thermal conductivity, while B describes nonelectronic contributions, e.g. from phonons. Heat transport in metallic systems is typically dominated by electrons. If electron scattering processes are elastic or quasi-elastic (i.e., energy is conserved), then $A \approx 1$. Hundreds of experimental measurements of thermal transport in metals and their alloys establish that, at room temperature, B can vary between ~1 and 20 W m^{-1} K^{-1}.

Electron scattering defects impedes both charge and heat transport. Consequently, metal alloys are observed to have lower σ and Λ_{Total} than their constituent materials. Alloy disorder also scatters phonons and decreases phonon thermal conductivity. As a result, B is typically observed to be lower in alloys than in single

crystals. Together the effect of disorder on electron and phonon thermal transport leads to Λ_{Total} of metal alloys having a strong, but well-understood, dependence on composition.

The ability of collective spin excitations (i.e., magnons) to carry heat at room temperature is unexplored, even in magnetic metals. However, recent theoretical investigations have explored the possibility of magnons being a non-negligible heat carrier. Zhou et al. perform atomistic simulations to predict a magnon thermal conductivity of ~7.5 W/m-K in bcc Fe at 300K [5]. Another study by Wu et al. utilizes spin-lattice dynamics simulations to deduce a magnon contribution of ~15 W/m-K [64], in bcc Fe at 300K. Moreover, recent investigations on ferromagnetic alloy systems reveal interesting magnetization dynamics as a function of composition [1], [2], [4], [65], [66]. Schoen et al. discover that certain Co-Fe alloy compositions feature low magnetic damping, comparable to ferrimagnetic insulators [1]. This was attributed to a minimization in the density of states at the Fermi level, resulting in a possible suppression of electron-magnon scattering. Through TR-MOKE experiments, Mohan et al. provide experimental evidence of prolonged lifetimes of magnetic excitations in Co-Fe alloys at both femto- and nanosecond timescales [66].

In this work, we report the electrical and thermal conductivity of thin-film and bulk Co-Fe alloys. We observe transport properties that depend on composition in a manner completely inconsistent with established trends. Co-Fe alloys with $x > 0.5$ have *higher* values for Λ_{Total} then either Co or Fe. To our knowledge, there are no experimental reports of transport properties in alloys where disorder does not impede

thermal transport. Furthermore, in the composition range of $0.2 < x < 0.6$, we observe an electronic contribution to the total thermal conductivity that is atypically low for high thermal conductivity metals. At a composition of $x = 0.25$, we find that thermal transport by electrons explains only ~65% of the total thermal conductivity. Our results suggest that the nonelectronic contribution to thermal conductivity, B, increases in Co-Fe alloys. In the composition range of $0.2 < x < 0.6$, our results imply an exceptionally large value for B of 50 ± 20 W m^{-1} K^{-1}. Prior to our study, the highest value ever reported for B was ~15 W m^{-1} K^{-1} in Ni-based alloy solutions [67].

The outline of this chapter is as follows: We first describe how we prepared three types Co_xFe_{1-x} samples: sputtered thin-films, a bulk diffusion multiple, and arc-melted bulk alloys. Second, we describe our time-domain thermo-reflectance (TDTR) and four-point-probe electrical measurements of transport properties. Third, we use simple kinetic theory models for electron transport to estimate electron mean-free-paths as a function of composition. Fourth, we present a Wiedemann-Franz law / Smith-Palmer analysis to estimate the nonelectronic contribution, B, to the total thermal conductivity Λ_{Total}. Finally, we consider the possibility of significant magnon thermal transport in Co-Fe alloys. Our analysis suggests that magnon transport is a likely explanation for the anomalously large value for B that we observe for Co-Fe alloys. Recent investigations by Zheng et al. show that for Ni-based alloy solutions, the non-electronic contribution could be as high as 15 W/m-K [67]. For bcc Fe, it is shown that the lattice contributions could be as high as 12 W/m-K [68].

4.2 Materials and Methods

Thin Films: We sputter deposit Co_xFe_{1-x} films, that are capped and seeded with Pt, onto Si/SiO_2 substrates using a direct current (DC) magnetron sputtering system (Orion, AJA International). The sample geometry is Si / SiO_2(300nm) / Pt(2nm) / Co_xFe_{1-x}(200nm) / Pt(20nm). We obtain Co_xFe_{1-x} layers ($0 \leq x \leq 1$) by co-sputtering two 4N purity Co and Fe elemental targets at different powers. The relative sputtering powers determine x. The base pressure in the sputtering chamber prior to deposition is $< 3.5 \times 10^{-7}$ torr. The Ar pressure during the sputtering process is ~3.5×10^{-3} torr.

To measure the composition of the Co_xFe_{1-x} alloy films, we perform Energy Dispersive X-Ray Spectroscopy (EDS) analyses with a scanning electron microscope (FEI Nova NanoSEM 450) at an operating voltage of 15 kV and working distance of 14 mm. We analyze the EDS data using the Aztec Synergy software (Oxford Instruments).

Diffusion Multiples: Diffusion multiples refer to alloy assemblies of three or more unique metal blocks that are inter-diffused at high temperatures to form solid solutions and/or intermetallic compounds [69]. In our analyses, we use a diffusion multiple featuring a ~250 μm Co-Fe composition gradient, prepared using a dual-anneal methodology. This involves a two-step heating process - an initial high temperature annealing at 1200°C for ~500 hours, and a subsequent heat treatment at 1000°C for ~1000 hours. After heat treatment, the sample is water quenched to ambient temperature. The dual annealing not only generates a wider composition gradient at the metallic interface, but also induces reliable phase precipitations. Thus, we can effectively render a

library of intermetallic alloys with pronounced phase equilibria. Further details on how the diffusion multiple was synthesized and processed can be found in [70].
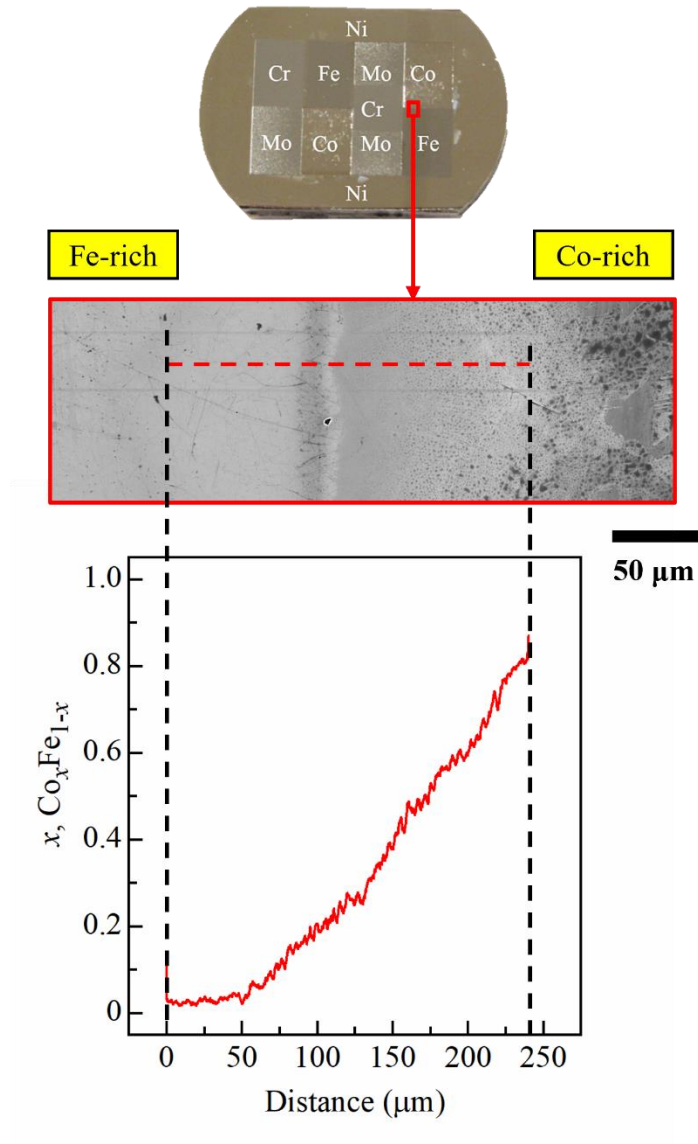
Figure 4.1. Microstructural Analyses in a Co-Fe Diffusion Multiple. We show the Co-Fe composition gradient along the interface in the diffusion multiple. We use scanning electron microscopy to obtain high resolution images of the Co-Fe interface, and then use energy dispersive X-ray spectroscopy to obtain the Co-concentration along the interface.

We characterize the Co-Fe interface using SEM and EDS, at 6 unique locations along the sample. At each location, we first obtain high-resolution scanning electron micrographs. Next, we collect EDS line-scans (step size ~77 nm) to determine the elemental Co and Fe compositions along each interface gradient. We also check for potential oxide formation and/or other contaminants in the regions of interest and find none. The length of the Co-Fe interface varies between 200 – 250 μm, and features a uniform composition gradient. The microstructural analyses at one of the six locations is plotted in Figure 4.1.

Arc-Melted Alloys: We prepare arc-melted Co_xFe_{1-x} alloy samples ($0 \leq x \leq 1$) using 99.999% elemental purity Co and Fe buttons. We use a nominal total mass of ~1.5 gm to make each Co_xFe_{1-x} alloy sample. We determine the individual masses of Co and Fe according to the desired alloy composition. We place samples of Co and Fe on a water-cooled copper hearth inside an Arc-Melter (Centorr Bell Jar series). Heating occurs until a single-phase liquid is produced. The samples are then allowed to solidify, flipped over, and remelted thrice to produce homogenous alloys. Finally, we embed the solidified Co_xFe_{1-x} alloys in epoxy resin (Alumilite Clear Casting Resin) and vertically section using a diamond wafering blade to reveal the alloy cross-section (dia. ~ 7 mm). We then abrade these cross-sections using SiC paper (up to ~ 1200 grit) and subsequently, fine polish using Al_2O_3 powder to a surface roughness of < 3 nm, as determined by atomic force microscopy (Dimension 3100, Veeco).

We use EDS to verify the elemental Co and Fe composition of each arc-melted alloy. In addition, we interrogate the phase in these alloys using X-Ray Diffraction (XRD, Panalytical Empyrean) with a Cu Kα source, see Figure 4.2.
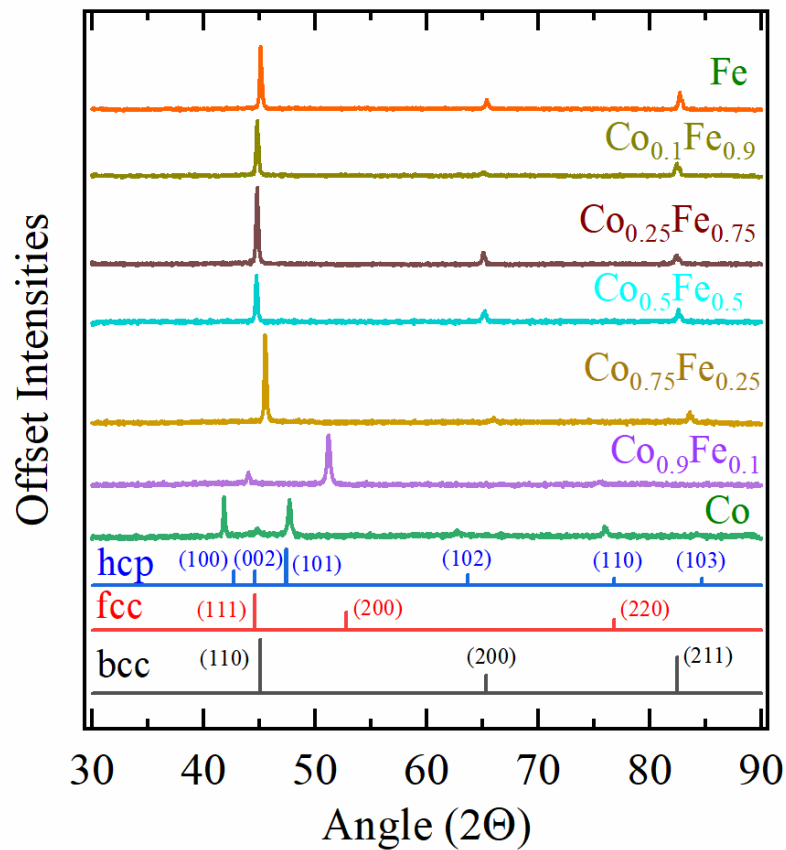
Figure 4.2. X-Ray Diffraction data for arc-melted Co-Fe alloys We note that the peaks for Fe, and Co_xFe_{1-x} ($0.1 < x < 0.5$) correspond to BCC crystal structure. At $x = 0.75$, we see a shift in the BCC peaks. At $x > 0.9$, we see that the phase is no longer pure BCC. For $x = 0.9$, the peaks were fit to an FCC crystal structure. For Co, the peaks correspond to HCP crystal structure.

Time-Domain Thermo-Reflectance (TDTR): TDTR is a widely used technique to measure the thermal properties in both thin films and bulk media [36]. We use a

pump/probe laser system to perform TDTR measurements on Co_xFe_{1-x} thin films and bulk alloys. In addition, we spatially probe the variation of thermal conductivity along the Co-Fe composition gradient in our diffusion multiple.

A Ti:sapphire oscillator (Mai Tai, Spectra-Physics) produces a pulsed laser beam with an 80 MHz repetition rate and wavelength of 783 nm. This laser beam is split into "pump" and "probe" components. The time-delayed pump beam heats the metal surface. The subsequent temperature-dependent change in reflectance of the metal surface is measured by the probe beam. The pump beam is modulated to a frequency (f) of 3 or 10.7 MHz using an electro-optic modulator. The probe beam is modulated to 200 Hz using a mechanical chopper. Our choice of f and the spot size (w_0) of the pump/probe beams depends on whether we seek to interrogate through-plane or in-plane thermal transport in our samples. We set the powers of the pump and probe beams to keep the steady state temperature rise less than ~30K during measurements. Additional details on our optical pump/probe setup can be found in Ref. [37].

The thermo-reflectance signals are measured by a radio-frequency (RF) lock-in amplifier. The in-phase and out-of-phase signals measured by the lock-in depend on thermal transport properties of the sample. We analyze the ratio $-V_{in}/V_{out}(t)$, using the Feldman algorithm for isotropic heat diffusion across multi-layered systems [35]. The primary input parameters in the TDTR model are the thermal conductivities (Λ), volumetric heat capacities (C), and thicknesses (h) of each layer in the stack. We utilize the volumetric heat capacities from literature. The total thermal conductivities of typical transducer metals (such as Al, Pt, etc.) and substrates (such as SiO_2/Si, sapphire, etc.) are

well known. In addition, we estimate the thicknesses of each layer using picosecond acoustic signals in the V_{in} output as described by Hohensee et al. [34].

We treat the thermal conductivity of the metal as a fit parameter. In Figure 4.3. (a), we show an example of the TDTR data for a $Co_{0.20}Fe_{0.80}$ film and the thermal model predictions with the best-fit value for the thermal conductivity.

For thin-film measurements, we use a pump modulation frequency, $f = 10.7$ MHz, and a $1/e^2$ laser spot size of 7.8 μm, to maintain quasi-one-dimensional thermal transport. At this frequency, the ratio $-V_{in}/V_{out}(t)$ is sensitive to the through-plane thermal conductivity of the metal film, and the thermal effusivity of SiO_2. For measurements of the bulk Co_xFe_{1-x} alloys and the diffusion multiple, we decrease the pump modulation frequency to $f = 3$ MHz, and use a $1/e^2$ laser spot size of 3.4 μm. We choose a lower f and smaller spot size for measurements of bulk samples to increase the sensitivity of the ratio $-V_{in}/V_{out}(t)$ to the bulk metal's thermal conductivity.

Thermo-Reflectance Mapping: For diffusion multiple samples, we collect thermo-reflectance maps to measure the evolution of thermal conductivity with position, and therefore composition. For spatial mapping, we collect thermo-reflectance signals at a single delay time [71]. For these experiments, we did not coat the Co-Fe diffusion multiple with a transducer layer. In the absence of a transducer layer, the output ratio $-V_{in}/V_{out}(t)$ in our thermal model is equally sensitive to the Co-Fe thermal conductivity at all delay times after the first ~100 ps. We collected the thermo-reflectance maps at a

delay time of t = 200 ps, with a pump modulation frequency of f = 3 MHz, and a $1/e^2$ laser spot size of 3.4 μm.

We mount the diffusion multiple on a 2-axis sample stage with motorized actuators. We carefully align the sample plane such that any bidirectional movement along the sample surface results in < 5% change in the laser spot size, i.e., the sample remains in focus throughout the measurement. V_{in}/V_{out} *(t=200 ps)* is recorded as a function of position. We measure an area of ~200 μm x 10 μm with a step-size of 2 μm (500 total points). We convert the ratio vs. position to thermal conductivity vs. position using our thermal model (described above). We also show a thermo-reflectance plot of the Co-Fe interface (in-phase signals vs. position/composition). The Co-concentrations in the same area of the sample along the Co-Fe interface are measured with scanning electron microscopy and energy dispersive X-ray spectroscopy.

Collinear 4-point probe measurements: We perform collinear 4-point probe measurements on Co_xFe_{1-x} thin films using a commercial probe head (Signatone) connected to a Sourcemeter (Keithley K2410). For arc melted bulk Co_xFe_{1-x} alloys, the resistance is much lower than for thin-film samples. Therefore, for bulk samples we use a Keithley K2410 as a current source. We drive currents I from -200 mA to +200 mA and measure the resulting voltages V using a Keithley K2182 nanovoltmeter. We use the slope of V versus I to determine the sheet resistance R of the alloys. We obtain a measure of the electrical resistivity ρ from sheet resistance after accounting for geometric correction factors related to sample dimensions and thickness. We use the Wiedemann-

Franz law to determine the electronic thermal conductivity from the electrical resistivity. As a control measurement, we measure a high conductivity single crystal Al substrate from MTI. We observe 2.69 $\mu\Omega - $ cm, in good agreement with the literature value of 2.65 $\mu\Omega - $ cm for high purity single crystal Al [72].

van der Pauw measurements: We also perform 4 probe measurements on arc melted bulk Co_xFe_{1-x} alloys following the standard van der Pauw configuration. We use a probe station equipped with four tungsten carbide probe tips to establish electrical contact. We drive and drain known currents I from -200 mA to +200 mA at two of the four contact points and measure the voltages V at the other two contact points with a nanovoltmeter. We measure the sheet resistivity (ρ) of the bulk alloys following the method described in [73].

4.3 Experimental Results

4.3.1 Thermal Transport in Co-Fe Thin Films

We summarize the results of our thermal conductivity measurements of co-sputtered polycrystalline Co_xFe_{1-x} thin films in Figure 4.3. We plot the total thermal conductivity (Λ_{Total}) measured by TDTR, at nine Co-Fe compositions in Figure 4.3. (b). The measured Λ_{Total} for thin-film Fe is 42 W/m-K and thin-film Co is 58 W/m-K. We observe a minimum thin-film thermal conductivity of 28 W/m-K at composition of $Co_{0.10}Fe_{0.90}$. As Co-concentration increases beyond 10 at.%, Λ_{Total} increases steadily and

reaches a maximum of 64 W/m-K at $Co_{0.60}Fe_{0.40}$. Thereafter, we see a decrease in Λ_{Total} at $Co_{0.75}Fe_{0.25}$, and a subsequent increase at pure Co.

Surprisingly, Λ_{Total} is a maximum in a sample with a large amount of compositional disorder. $Co_{0.60}Fe_{0.40}$ has a higher thermal conductivity than Fe (by ~ 50%) and Co (by ~ 10%). In addition to alloy disorder, this Co-Fe alloy composition may have structural disorder. Similar thin-film Co-Fe samples have been observed to undergo a phase transition from BCC at 60 at.% Co to mixed phase at 75 at.% Co, to FCC at Co [1].

We report the electronic contribution to thermal conductivity ($\Lambda_{Electronic}$) in Figure 4.3. (b). We estimate the electronic thermal conductivity using the Wiedemann-Franz law and four point probe measurements of the electrical resistivity. The Co_xFe_{1-x} compositional dependence of $\Lambda_{Electronic}$ is similar to that displayed by Λ_{Total}, with an exception around 20 at.% Co. We observe an electrical conductivity, and therefore electronic thermal conductivity, that is 40% and 70% lower for $Co_{0.2}Fe_{0.8}$ than $Co_{0.18}Fe_{0.82}$ and $Co_{0.25}Fe_{0.75}$, respectively. Our observation of a minimum in the thin-film electrical conductivity at a composition of x ~ 0.20 is in agreement with the observations of Ref. [65] .
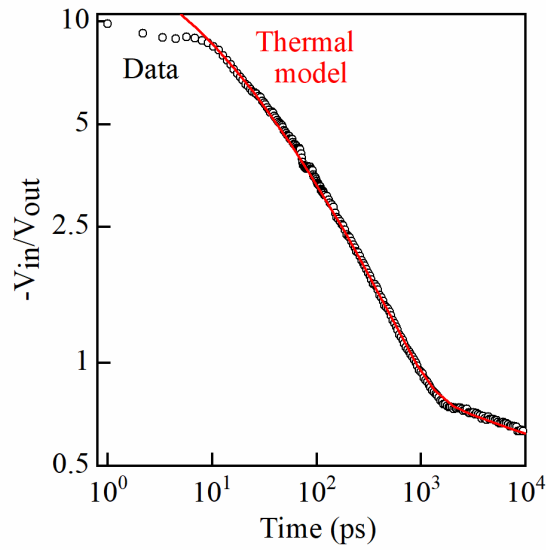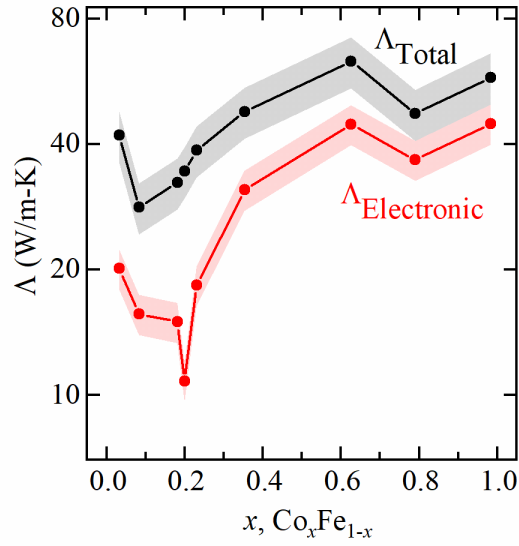
Figure 4.3. Summary of Nanoscale Thermal Transport Measurements in Co$_x$Fe$_{1-x}$ Thin Films. (a) Ratio of in-phase and out-of-phase TDTR signal as a function of delay time for a Co$_{0.25}$Fe$_{0.75}$ film. The red solid line represents thermal model fit to the experimental data (shown in open black circles) with Λ_{Total} = 33 W/m-K. **(b)** Total thermal conductivity measurements (Λ_{Total}) and the electronic contribution to thermal conductivity ($\Lambda_{Electronic}$) predicted by the Wiedemann-Franz law.

4.3.2 Thermo-reflectance Mapping in Co-Fe Diffusion Multiple

We describe the compositional dependence of thermal conductivity in a Co-Fe diffusion multiple in Figure 4.4. In Figure 4.4. (a), we plot the output TDTR ratio, -V_{in}/V_{out} *(t)*, as a function of pump-probe time-delay measured at six locations along the Co-Fe interface. The ratio varies linearly with the measured thermal conductivity, Λ_{Total}, provided that the $1/e^2$ laser spot size is constant. Thus, the TDTR scans in Figure 4.4 (a) indicate that the highest Λ_{Total} value is at a composition of $Co_{0.50}Fe_{0.50}$. Λ_{Total} depends weakly on composition for $0.5 < x < 0.75$. Alternatively, Λ_{Total} is a strong function of composition for *x < 0.5*, with a minimum value at *x* = 0.1. The Co-Fe interface beyond $Co_{0.75}Fe_{0.25}$ was optically rough, resulting in diffuse reflectance. Thus, we could not perform reliable thermo-reflectance measurements of the diffusion multiple beyond *x >* 0.75.

In Figure 4.4 (b), we plot Λ_{Total} as a function of Co_xFe_{1-x} composition ($0 \leq x \leq$ 0.75). We utilize scanning electron microscopy energy dispersive X-ray spectroscopy data from the Co-Fe interface to carefully align the composition and thermal conductivity profiles. We observe that the compositional variation in thermal conductivity along the Co-Fe interface follows a similar same trend as that observed in the Co_xFe_{1-x} thin films. We measure Λ_{Total} = 80 W/m-K for pure Fe, which is in excellent agreement with literature values [74]. As Co solute is added into Fe, we note that the value of Λ_{Total} drops and approaches a minimum of 54 W/m-K, at a concentration of ~10 at.% Co. As the Co concentration increases further, the thermal conductivity increases monotonically, and reaches a maximum value of 150 W/m-K at ~50 at.% Co – higher than the measured

Λ_{Total} values for pure Fe or pure Co [74].. As Co concentration increases to 75 at.% Co, the Λ_{Total} value decreases to 135 W/m-K.

4.3.3 Thermal/Electrical Transport in Co-Fe Arc Melted Alloys

Figure 4.5. denotes the electrical resistivity and thermal transport measurements in arc melted Co_xFe_{1-x} alloys. We summarize the electrical resistivity (ρ) measurements as a function of composition in Figure 4.5. (a). ρ values measured using the collinear 4-point probe method agree reasonably well with that measured using the van der Pauw configuration. We measure ρ in Fe and Co to be 11.5 and 5.8 $\mu\Omega$ – cm, respectively. This is in excellent agreement with literature values for Fe and Co of 12 $\mu\Omega$ – cm and 5.6 $\mu\Omega$ – cm. We observe that ρ increases by ~ 65 % between $0 \leq x \leq 0.2$, peaking at 19 $\mu\Omega$ – cm at $x = 0.20$. At $x > 0.5$, ρ depends weakly on composition. Overall, our results agree well with those reported in [65], where Srichandan et al. measured electrical resistivity in Co-Fe films grown using molecular beam epitaxy. Furthermore, our data shows similar trends as that reported in [75], where Freitas et al. carried out measurements at 4K.

In Figure 4.4. (b), we plot the total thermal conductivity from TDTR scans, as well as the electronic contribution to the thermal conductivity, predicted using the Wiedemann Franz Law. We observe that Λ_{Total} for each composition agrees excellently with the measurements from the diffusion multiple. Similarly, as observed in the thin films, the $\Lambda_{Electronic}$ values show a minimum at $x = 0.20$, and follow a similar trend as that of Λ_{Total}.
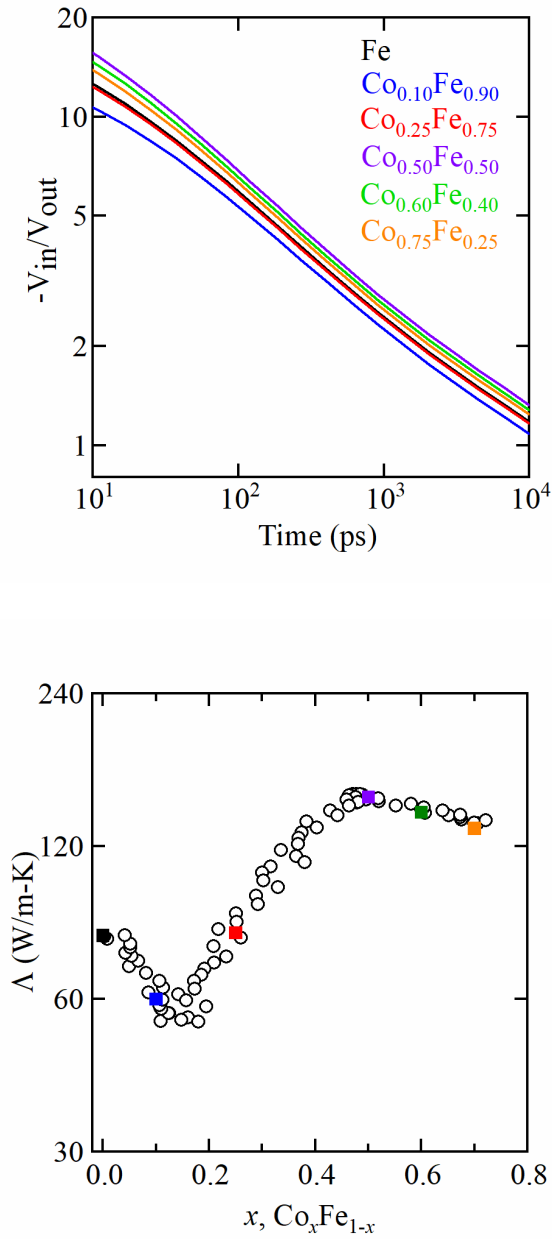
Figure 4.4. Compositional Dependence of Thermal Transport in a Bulk Co-Fe Diffusion Multiple (a) TDTR signal vs. time-delay at 6 locations along the Co-Fe interface of the diffusion multiple. The Co_xFe_{1-x} alloy composition at each of the 6 locations was measured via scanning electron microscopy energy dispersive X-ray spectroscopy (SEM-EDS). **(b)** Total thermal conductivity measurements (Λ_{Total}) as a function of Co_xFe_{1-x} alloy composition. Open black circles represent values obtained using thermo-reflectance mapping at a fixed time-delay of t = 200 ps. Filled squares represent thermal conductivity (Λ_{Total}) fits at compositions measured using full TDTR vs. time-delay scans from **(a).**
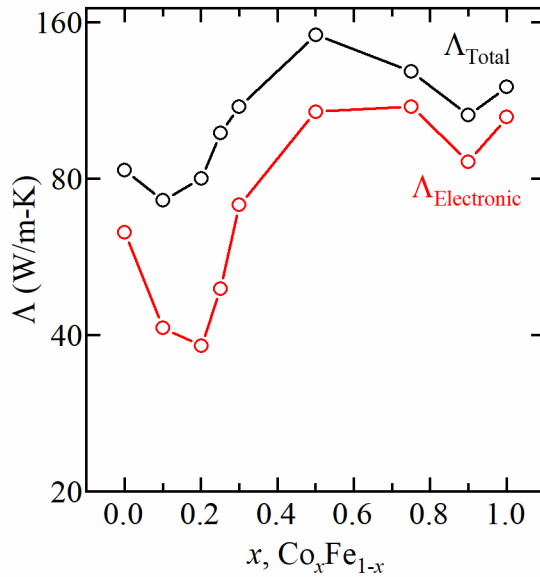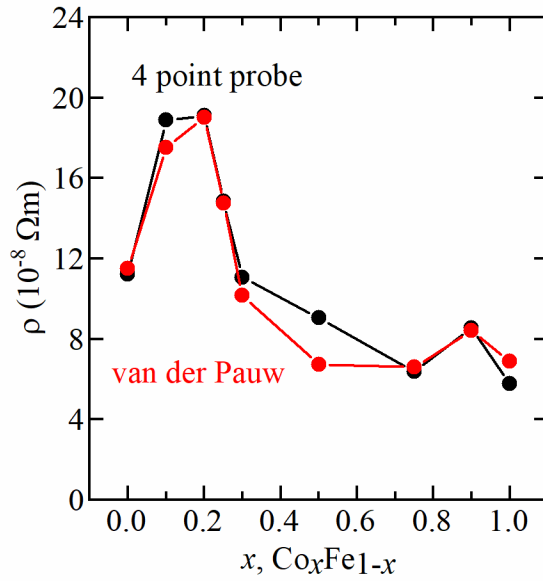
Figure 4.5. Electrical Resistivity/Electronic Conductivity Measurements in Arc-Melted Co_xFe_{1-x} Alloys (a) We plot the sheet resistance (ρ) obtained using the collinear 4-point probe method, as well as the van der Pauw method as a function of Co-concentration. **(b)** We plot the total thermal conductivity measurements (Λ_{Total}) obtained using TDTR in black. The red plot represents the electronic contribution to thermal conductivity ($\Lambda_{Electronic}$) predicted using the Wiedemann-Franz Law, as a function of Co-concentration.
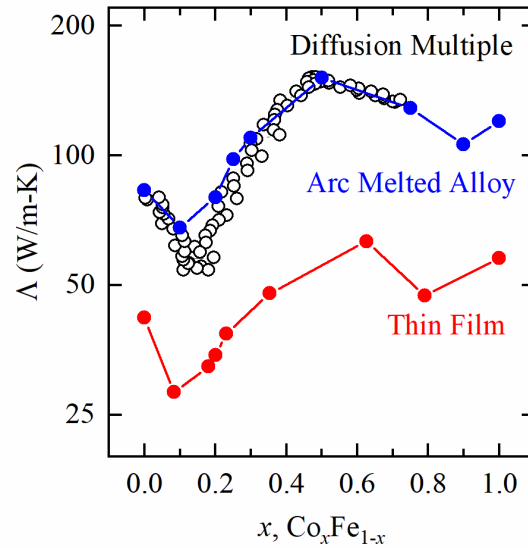
Figure 4.6. Summary of Thermal Conductivity across all the three Co-Fe systems The compositional dependence of thermal conductivity appears to follow the same trend in the case of thin films and bulk alloy samples. Moreover, the thermal conductivity values of the diffusion multiple and the arc-melted Co-Fe alloys are in excellent agreement with each other.

4.4. Analyses and Discussion

4.4.1. Compositional Dependence of Thermal/Electrical Conductivity

Textbook theories predict that alloys will exhibit lower thermal conductivity than their constituent pure metals. This is mostly attributed to crystallographic disorder induced by the addition of substitutional atoms to the lattice in metal alloys. Disorder scatters electrons and decreases electron mean-free-paths, resulting in lower conductivity. Experimental studies of transport in Ni-Rh [67], Cu-Au [76], Ni-Al [77], and Pt-Rh [78],

along with many others [79]–[81], report substantial decreases in electrical and/or thermal conductivity with increasing compositional disorder.

However, we observe a dramatic deviation in Co-Fe alloys from this nearly universal "textbook" behavior for thermal transport in alloys. The thermal and electrical conductivity of alloys with $x > 0.5$ seem largely unaffected by compositional disorder. We show that the Λ_{Total} – composition profile follows a similar trend in both sputtered thin films (which have less order than their bulk counterparts) and bulk alloys. Besides, the electronic contribution to thermal transport (as predicted by the WF-Law) shows a similar compositional dependence, except near x ~ 0.20, where there is a sharp drop in conductivity in both thin films and bulk Co-Fe alloys.

Moreover, and surprisingly, in both thin film and bulk Co_xFe_{1-x} alloys, Λ_{Total} is at a maximum at $\sim 0.5 \leq x \leq 0.6$. The thermal conductivity at these compositions surpasses Λ_{Total} for both Fe and Co, by ~50% and ~15% respectively. To our knowledge, there are no published studies where an alloy is shown to display higher conductivity than its constituent elements. Ordered intermetallic compounds like Ni-Al and Co-Al [82] have thermal and electrical conductivities comparable to their constituent materials. However, ordered intermetallic compounds have abrupt changes in transport properties near compositions where ordered phases are possible. We observe no abrupt changes in transport properties near compositions where ordered phases are most likely to form, e.g., near $x = 0.5$.

4.4.2. On the Average Electron Relaxation Times in Co-Fe Alloys

To explore the physical phenomena governing heat/charge transport in the Co-Fe alloys, we estimate the variation of the average electron mean free paths (l) as a function of composition. In addition to structural/compositional disorder, electron mean free paths are also affected by and quasi-particle interactions such as electron-phonon and electron-magnon scattering. Matthiessen's rule suggests that the total electrical resistivity in a metal is the series sum of resistivities due to independent individual scattering effects,

$$\rho = \rho_0 + \rho(T). \qquad (2)$$

Here, ρ_0 is the electrical resistivity due to disorder, and $\rho(T)$ is a measure of temperature-related contributions from scattering. We estimate the composition dependence of ρ_0 using measurements by Freitas et al. of electrical resistivity of bulk CoFe samples vs. x at 4 K [75].

The Drude model for electrical transport relates electrical resistivity to electron energy relaxation times (τ_e),

$$\rho = \frac{m^*}{e^2 \times \eta_{eff} \times \tau_e}. \qquad (3)$$

Here, m^* is the effective electron mass and e is the electronic charge. We use the $m^* = 8$ value for Fe from [83] and consider no variation with composition on account of the nearly similar atomic masses for Fe and Co. Kinetic theory for electron thermal transport predicts

$$\Lambda_e = \frac{1}{3} C_e v_F{}^2 \tau_e = \frac{1}{3} \left[\frac{1}{3} \pi^2 D_F k_B{}^2 T \right] v_F{}^2 \tau_e. \qquad (4)$$

The density of states (D_F) at the Fermi level is a strong function of Co-concentration and is obtained from [1]. To obtain η_{eff} from D_F, we use the WF-Law derivation and equate (2) and (3), where $\sigma = 1/\rho$, as follows –

$$\eta_{eff} = \frac{1}{3} D_F v_F{}^2 m^*, \text{ where } v_F \text{ is the Fermi velocity.}$$

Ref [83] provides a v_F value for Fe to be $1.98 \times 10^8 cm/s$. On the other hand, Gall et al. [84] estimate the v_F value for Co to be $2.5 \times 10^8 cm/s$. Therefore we expect any changes to v_F with respect to composition to be small. We assume the value for Fe in our calculations for all compositions.

   With the above assumptions, we estimate the average electron relaxation times, τ_0 and $\tau(T)$ as a function of composition *x*. The corresponding electron mean free paths (l_{Total}, l_0, and $l_{(T)}$), $l = v_F \tau_e$, are also plotted in Figure 4.7. At 4K, contributions from quasi-particle interactions such as electron-phonon and electron-magnon scattering are negligible. The only possible contributions are scattering processes on account of compositional disorder, defects, and impurities, or electron-electron scattering. At 300K, the electronic mean free paths show an increase between $0.1 \leq x \leq 0.5$, alluding to a suppression in scattering, and a decrease in quasi-particle interactions.
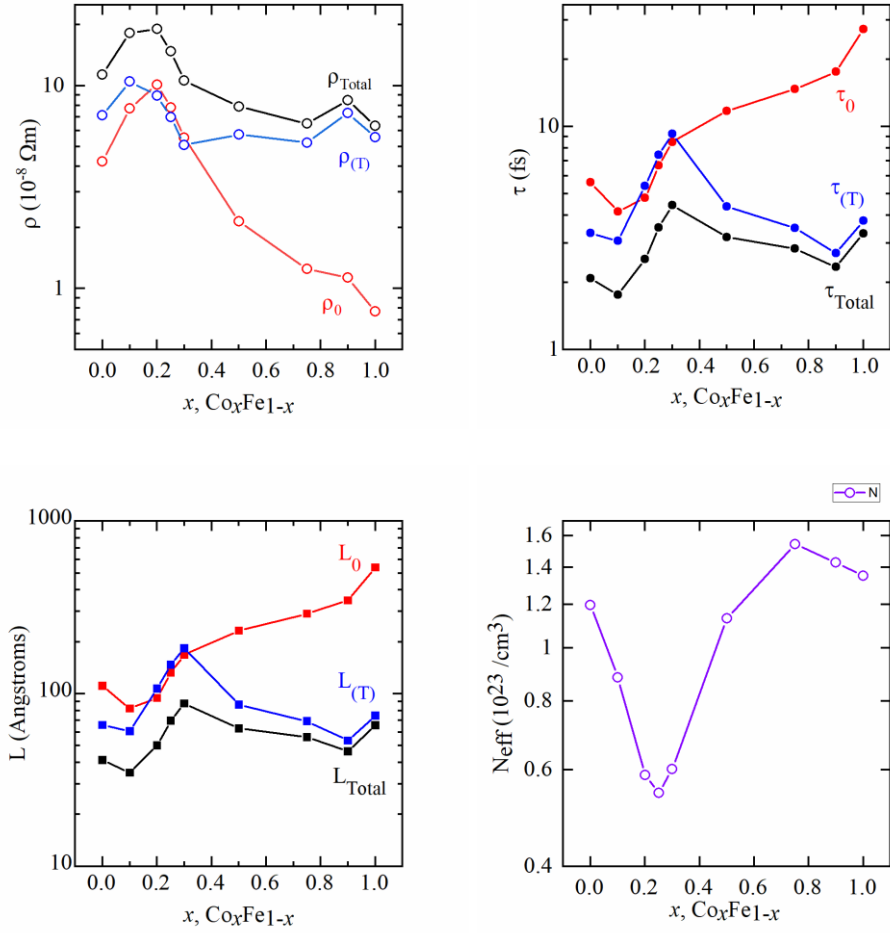
Figure 4.7. Energy Relaxation Times and Mean Free Path Approximations **(a)** We plot the experimentally measured electrical resistivity, ρ_0 by Freitas et al at 4K from Ref. [75] and our data at 300K, ρ_{Total}. ρ_{Total} - ρ_0 yields $\rho_{(T)}$. In **(b),** we plot the average electron relaxation times corresponding to ρ_0, ρ_{Total} and $\rho_{(T)}$ – τ_0, τ_{Total}, and $\tau_{(T)}$. Similarly, in **(c)**, we plot the average electron mean free path at 4K, 300K, and the difference, denoted by L_0, L_{total}, and $L_{(T)}$. **(d)** The effective number of charge carriers are plotted as a function of Co-concentration.

4.4.3. Applicability of the Smith-Palmer Equation

In Figure 4.8. we plot our experimentally measured values for Λ_{Total} vs electrical conductivity, $\sigma = 1/\rho$, along with the predictions using the Smith-Palmer equation, $\Lambda_{Total} = AL_0T\sigma + B$ [85]. In a non-magnetic metal, the nonelectronic contribution is from phonons. In magnetic materials, magnons could also contribute to the total thermal conductivity [5], [64]. In the limit that B is negligible and A = 1, the Smith-Palmer Equation becomes equivalent to the well-known Wiedemann-Franz Law.

Our data is best explained by the Smith-Palmer relation with A = 1 and B = 20 W/m-K. We set B = 20 W/m-K which is based on our measurements of Fe, as well as prior reports for the lattice thermal conductivity of Fe [68]. With these values for A and B, we find that the Smith-Palmer predictions for Λ_{Total} agree reasonably well with our experimental data for bulk Co_xFe_{1-x} at $x \leq 0.1$ and $0.75 \leq x \leq 1$. It also agrees reasonably well with all our thin-film data. However, for compositions $0.2 \leq x \leq 0.5$, there appears to be an offset of ~30 W/m-K, suggesting that B depends on composition. For $0.2 \leq x \leq 0.5$ we find A = 1 and B = 47 W/m-K yields excellent agreement with the data. This is explored in the next section.
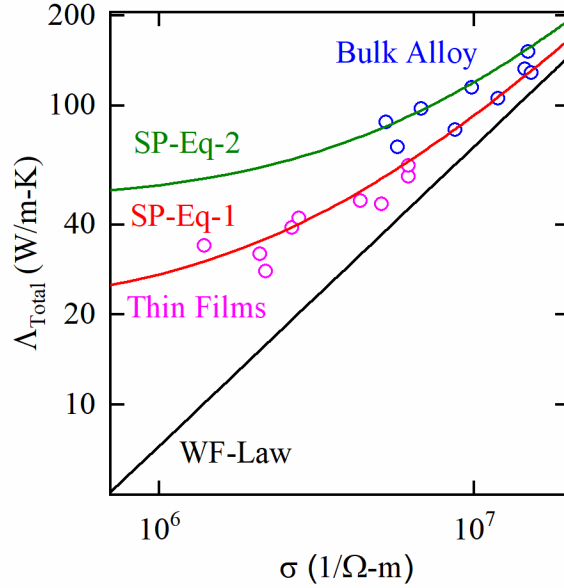
Figure 4.8. Smith-Palmer Equation and the Wiedemann-Franz Law Predictions We plot Λ_{Total} as a function of σ for both our bulk arc-melted Co-Fe alloys, as well as Co-Fe thin films. The WF-Law underpredicts Λ_{Total} for all Co-Fe alloy compositions in thin films and bulk alloys. In order to fit the data using the Smith-Palmer Equation, we use $\Lambda_{Total} = AL_0T\sigma + B$, where A and B are empirical constants. We find that we can fit our datasets using two values of A and B: for $x \leq 0.1$ and $0.75 \leq x \leq 1$, A = 1 and B = 20 W/m-K, for $0.2 \leq x \leq 0.5$, A = 1 and B = 47 W/m-K. This suggests that B has compositional dependence.

4.4.4. Non-electronic Contribution and Possibility of Magnetic Thermal Transport

We summarize the compositional dependence of the non-electronic contribution to thermal conductivity in Figure 4.9. We estimate the non-electronic contribution to thermal conductivity ($\Lambda_{Non-electronic}$) by subtracting the $\Lambda_{Electronic} = \sigma L_0 T$ from Λ_{Total} in both Co-Fe thin films and bulk alloys. Overall, the trends for the nonelectronic thermal conductivity are similar for thin-film and bulk samples. For pure Co and Fe, the $\Lambda_{Non-electronic}$ values are nearly identical. Additionally, the dependence of $\Lambda_{Non-electronic}$ on x is similar across the range $0.1 \leq x \leq 0.9$. Amongst the alloy samples (not pure Co and Fe),

the $\Lambda_{Non\text{-}electronic}$ is highest for $0.2 \leq x \leq 0.5$. For both bulk and thin-film alloys, $\Lambda_{Non\text{-}electronic}$ peaks near x ~ 0.20, followed by a steady decline between $0.2 \leq x \leq 0.75$. We note that the effect of small amounts of alloy disorder, i.e., $x < 0.1$ or $(1\text{-}x) < 0.1$, appear to be different in our thin-film vs. bulk samples.

The $\Lambda_{Non\text{-}electronic}$ values we observe for bulk $Co_xFe_{1\text{-}x}$ alloys with $0.2 \leq x \leq 0.5$ are exceptionally high. Typical values for $\Lambda_{Non\text{-}electronic}$ in 3d ferromagnetic metals range from 15 W/m-K (in Ni) [67] to 20 W/m-K (in Fe) [68]. Zhou et al. predict a phonon contribution of 12.5 W/m-K for bcc Fe at 300K [5], which is plotted in Figure 4.9. On the other hand, Wu et al. predict a phonon conductivity of 8.3 W/m-K for Fe at 300K [64].
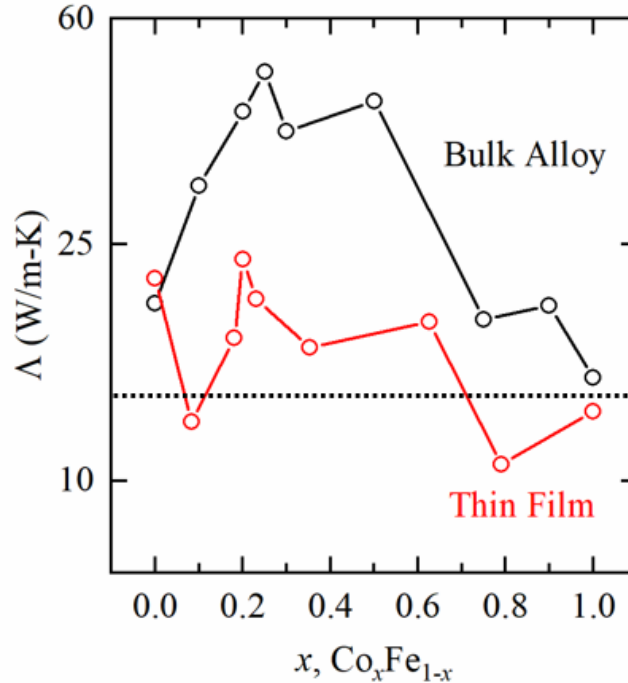
Figure 4.9. Non-electronic Contribution in Bulk Alloy and Thin Films The non-electronic thermal conductivity reflects the similar composition-dependence in both thin films and bulk-alloy samples. In both samples, we see substantial non-electronic contributions between $0.2 \leq x \leq 0.5$. Moreover, the values in both Fe and Co for both thin films and bulk alloys are reasonably close agreement with each other.

$\Lambda_{Non\text{-}electronic}$ includes contributions from the lattice (i.e., phonons) and collective spin excitations (e.g., magnons). We exclude the composition dependence of the phonon thermal conductivity as a likely explanation for the large values $\Lambda_{Non\text{-}electronic}$ at $0.2 \leq x \leq 0.5$. Phonon thermal conductivity depends largely on bond strength, anharmonicity, crystal structure, atomic mass, and defect density. The only parameter we expect to change significantly with x is defect density, which will decrease the lattice thermal conductivity. Therefore, the nonelectronic thermal conductivity of pure Co and Fe can safely be viewed as an upper limit on the phonon thermal conductivity of Co_xFe_{1-x} alloys. A lattice contribution of 10-20 W/m-K leaves approximately 30 to 40 W/m-K of thermal conductivity unexplained.

4.5 Conclusions

In conclusion, we are able to demonstrate that there is a larger-than-expected thermal conductivity in Co-Fe alloys than the simple theory for electronic transport would suggest. One possible explanation is that the WF-Law underestimates the amount of heat carried by electrons in Co-Fe alloys. Recent investigations reveal violations to the WF-Law in several metallic systems [86]–[90], mostly due to quasi-particle interactions resulting in inelastic scattering or hydrodynamic collective motion of charge carriers. But these phenomena typically occur only at cryogenic temperatures. These phenomenon usually leads to the WF-Law overpredicting $\Lambda_{Electronic.}$ We are unaware of any scattering mechanisms that would degrade charge currents but not heat currents at ~300K.

Another (and in our view more likely) explanation for the large values of $\Lambda_{Non\text{-}electronic}$ in Co-Fe alloys is magnon thermal transport. Spin ladder systems are known to have significant magnon thermal conductivity values ranging from ~10 to ~100 W/m-K at 300K [91]. We are unaware of any experimental studies reporting significant magnon thermal conductivity in other materials at room temperature. However, several recent theory papers predict that magnon thermal conductivity can be significant in magnetic metals. Atomistic simulations by Zhou et al. predict a magnon thermal conductivity of ~7.5 W/m-K [5], whereas Wu et al. used spin-lattice dynamics simulations to predict a magnon thermal conductivity of ~15.2 W/m-K [64], both in bcc Fe at 300K.

In stark contrast to electron or phonon lifetimes, magnon lifetimes can increase in alloy systems. Qin et al. reveal that magnons may have longer lifetimes in Fe-Pd alloys [4]. Research by Schoen et al. [1] and [our preprint] in Co_xFe_{1-x} thin films shows that the lifetime of magnetic precessions at $x \sim 0.25$ are at least twice as long as that in Co and Fe. The low damping of magnetic precession is due to the reduced availability of conduction electrons in alloys, which limits scattering, and enhances the lifetime of magnetization dynamics.

Chapter 5.

Nanoscale Thermal Transport in Al-PVDF Nanocomposites

5.1. Introduction

Energetic nanocomposites are typically comprised of metal particles (fuel/oxidizer) dispersed in a polymer matrix (reactive binder material). When highly electronegative elements like Fluorine react with metals like Aluminum, considerable heat is generated. In fact, research has indicated that the energy density for Al/fluorination reaction is $\sim 2\times$ higher than the Al/oxidation reaction[92], [93]. Hence, incorporating Aluminum nanoparticles in fluoropolymers is attractive for energetics and solid rocket propellant applications. A comparative combustion study of Aluminum nanoparticles in three fluorine-rich polymers, PVDF, Viton and THV shows that Al-PVDF has the highest burn rate amongst them all [94]. Moreover, Al-PVDF has excellent mechanical stability, even at high volume fractions of Al (such as 50%) and is easy to process, making it a promising candidate for combustion applications [6], [7].

The flame propagation characteristics of Al-PVDF composites are a strong function of Al volume fraction (ϕ) [7]. At low Al volume fractions ($\phi < 10\%$), the Al-PVDF composite can be ignited using a laser, however, the combustion is not sustained. At $\phi \geq 30\%$, these composites demonstrate self-sustained combustion upon ignition. In addition, Al-PVDF composites with the highest ϕ also exhibit the fastest flame propagation speeds [6].

Several studies attribute these observations to the differences in the thermal properties of Al-PVDF films as a function of ϕ. Al and PVDF have dissimilar thermal conductivities that vary by almost three orders of magnitude. Thus, in composites with low ϕ, it is possible that thermal energy transfer is impeded by the insulating PVDF polymer[7], [95]–[97], which likely disrupts the flame spread. As ϕ increases, it can be reasonably argued that the Al nanoparticles are spaced closer, and thus, there likely is minimally interrupted heat transfer. Flame propagation depends on two competing mechanisms – (i) how fast heat is generated, which is a function of reaction chemistry, and (ii) and how fast the generated heat is transferred to cooler regions, which depends on heat diffusion [98].

In this study, we aim to interrogate the effects of increasing Al volume fraction on thermal transport in Al-PVDF nanocomposite films. We perform frequency-dependent time-domain thermo-reflectance (TDTR) measurements on thin Al-PVDF films as a function of ϕ (0 – 50 %). Our experiments yield data that shows a monotonic enhancement of thermal conductivity as ϕ increases. At $\phi = 50\%$, the total thermal conductivity ($\Lambda \sim 0.58 \, W/m\text{-}K)$ is $\sim$ 100% higher than PVDF with no Al nanoparticles ($\Lambda \sim 0.30 \, W/m\text{-}K)$. However, at $\phi = 10\%$, there is a ~10% increase in ($\Lambda \sim 0.34$ W/m-K). A higher thermal conductivity likely corresponds to more effective heat conduction. Hence, it is possible that the enhancement of bulk thermal conductivity upon increasing the Al volume fraction in Al-PVDF composites contributes to greater flame spread.

We compare our TDTR results to two mean field approximation models that predict the effective thermal conductivity in composites – the Maxwell-Eucken model

[99], [100] and the Nielsen-Lewis model [101]–[103]. Our data agrees well with the Nielsen-Lewis model predictions for Al volume fractions below 20%. Above volume fractions of 20%, we find that the N-L model overpredicts the thermal conductivity of the Al-PVDF film. This could be attributed to the significant porosity exhibited in Al-PVDF films with increasing Al volume fractions, shown in our microstructural analyses. This changes the heat transfer mechanisms from strictly solid-solid conduction to include the deleterious effects of solid-gas boundary and other heterogenous heat transfer mechanisms. Porosity will reduce the overall thermal conductivity of the film at higher Al volume fractions. This may be why the N-L model overpredicts Λ at high ϕ. It is important to note that the N-L model assumes homogeneity in particle distribution.

To visualize and quantify the effects of structural inhomogeneities on nanoscale thermal properties, we employ high-resolution thermo-reflectance mapping. We show that the local thermal conductivity varies significantly across the Al-PVDF nanocomposite, for all Al volume fractions. We see two major types of structural inhomogeneities in these films – $1 - 5$ μm sized Al nanoparticle clusters and $1 - 3$ μm sized pores. Our maps show that in areas of Al coalesced particles, the local thermal conductivity value reaches ~ 77 W/m-K. Similarly, we see that pores in the film are infiltrated by epoxy resin during the embedded process, and show thermal conductivity values of less than 0.2 W/m-K.

Our experimental TDTR measurements offer critical insight into the nanoscale thermal transport of PVDF-Al films. We probe how the effective thermal conductivity varies with volume fraction, as well as how the local thermal conductivity varies spatially

at sub- μm resolutions. The results reported in this work will aid in quantitative modelling of conductive heat transfer by the energetics community, to predict flame propagation and combustion characteristics in these material systems.

5.2 Materials and Methods:

Sample Preparation and Characterization:

Thin film lay-up and Materials Characterization: We prepare six films, each with varying volume fractions of Al – 0%, 10%, 20%, 30%, 40%, 50%. We dissolve 15 gms of PVDF in DMF and stir for at least 12 hours. The weight of Al nanoparticles added will depend on the final volume fraction we want to achieve. We add the desired amount of Al nanoparticles to the PVDF solution and mix with a vortex mixer. We sonicate the resulting homogenous Al/PVDF mixture for approximately an hour. We further homogenize the mixture by stirring on a stir plate for at least 24 hours. This mixture is additionally sonicated for at least 30 minutes prior to printing. Finally, we print the Al/PVDF film.

Scanning electron microscopy and Energy Dispersive X-ray spectroscopy reveal areas with F concentrations that indicate PVDF-dense regions, and Al agglomerations that indicate Al nanoparticle clusters formed due to coalescing.
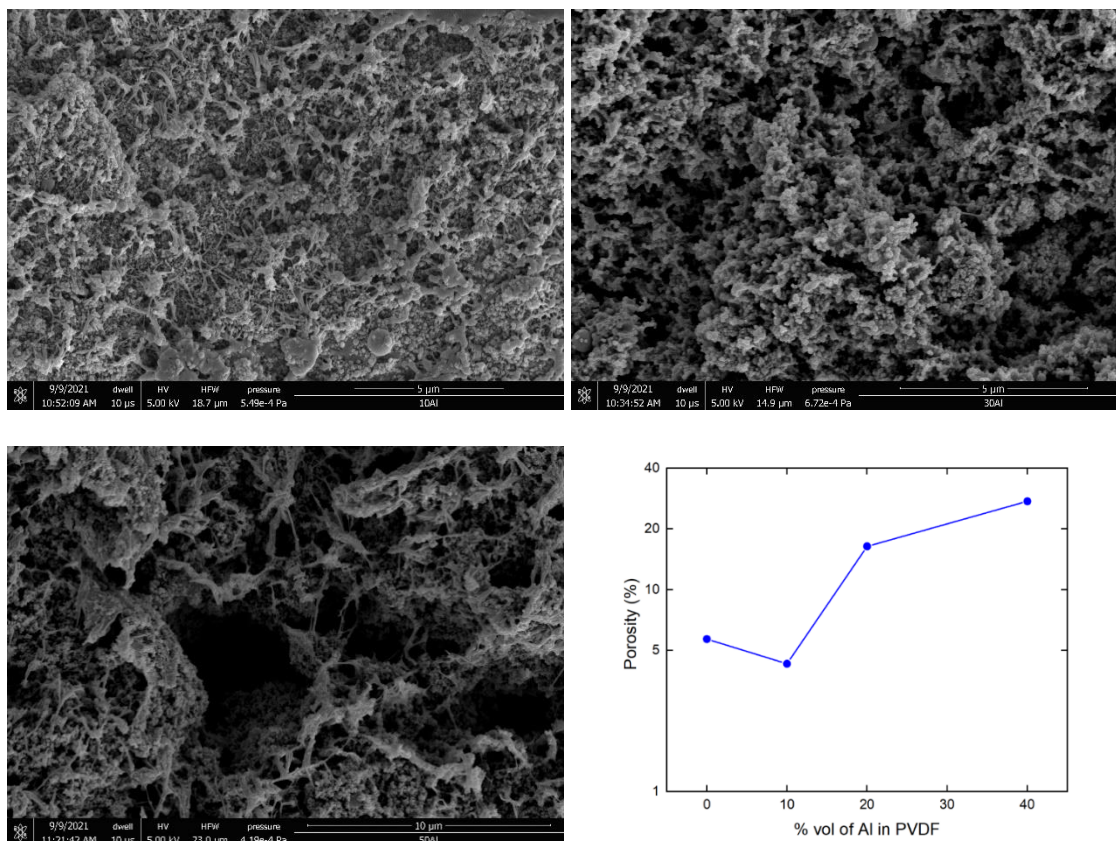
Figure 5.1. Materials Characterization of an Al-PVDF film as a function of Al volume fraction (a), (b) and **(c)** show scanning electron micrographs (SEM) of Al-PVDF films with a volume fraction of 10%, 30% and 50% respectively. There is visible increase in porosity with increasing volume fraction. As volume fraction increases, we see that the amount of Al particle agglomerates visible also shows an increase. In **(d),** we plot the porosity as a function of Al volume fraction. We note, through image processing using Image-J, that the porosity increases by a factor of 7, going from PVDF with no Al to 50% vol. Al – PVDF.

Preparation of the Sample Surface:

(i) Embedding in Epoxy Resin: We cut the Al/PVDF films into long thin sections and embed them in Spurr's resin (EMS). We choose Spurr's resin for the ability to tune its hardness to match that of the embedding material – this is to enable cleaner sectioning during the microtoming process. Spurr's resin is comprised of four components: (i) ERL

4221, the epoxy resin component; (ii) DER 736, a glycol-based flexibilizer; (iii) NSA, a hardening agent; and (iv) DMAE, an accelerating agent that invokes rapid curing at 70°C and minimizes resin penetration into the polymer sections. We modify the hardness of the final resin block by changing the amount of DER 736 and NSA. We chose the relative formulation of the ERL : DER : NSA to be 1.25 : 1 : 3.125 by mass. We add 0.69 wt. % of DMAE as the final curing agent. We de-gas this mixture at room temperature for about ~20 minutes to remove any air bubbles. We embed polymer samples in this mixture in silicone molds and cure at 70°C for ~8 hours to form hard sectioning blocks. Further details about this formulation can be found in [104].

(ii) Sectioning with a Diamond Knife: We use an ultramicrotome (insert model info from CFAMM) to section fully cured resin blocks. To do so, we first utilize a glass knife prepared using a glass knife-maker (insert model info) to create a desired flat trapezoid surface of RMS roughness ~100 nm. Subsequently, we use a 37° AFM diamond knife (Diatome) to produce smooth polymer cross-sections. Creating smooth cross-sections capable of specular reflectance was challenging, especially since we encounter Al nanoparticles loosely dispersed into the PVDF polymer matrix. Through multiple attempts, we note that a sectioning speed of 0.7 cm/sec, cutting angle of 6°, and a section thickness of 70 nm produced the best results, with the least vibrational "chatter". We use atomic force microscopy (AFM, Veeco) to verify that the RMS roughness of the Al/PVDF polymer cross-sections is less than 10 nm.

(iii) Coating with an Al Transducer Layer: To enable thermo-reflectance measurements, we sputter deposit a thin Al layer onto the polymer sample surface using a

direct current (DC) magnetron sputtering chamber (Orion, AJA International). The chamber base pressure prior to sputtering is $< 3.5 \times 10^{-7}$ torr. We use high purity Ar gas to enable sputtering at a pressure of $\sim 3.5 \times 10^{-3}$ torr. We use a high purity (99.995%) Al target (Kurt J. Lesker) at a sputtering power of 200W. We chose Al as an opaque transducer on account of its large thermo-reflectance (*dR/dT*) at 783 nm, which is the wavelength of our TDTR measurements.

Time-Domain Thermo-Reflectance (TDTR):

We use time-domain thermo-reflectance (TDTR), an established optical thermometry technique, to measure the thermal conductivity of the Al/PVDF films [36]. We utilize a mode-locked Ti:sapphire oscillator (MaiTai, Spectra Physics) to generate a periodic train of laser pulses at 80 MHz. This output light is split into "pump" and "probe" beams. The pump beam irradiates the surface of the transducer. The resulting temperature rise causes a variation in the reflectance, which is detected by the probe beam. In our TDTR set-up, the pump beam is delayed in time with respect to the probe beam using a mechanical delay stage (Akribis Systems DGL150). This allows for a time domain of up to 9 ns. The pump beam is modulated to a desired frequency (f) spanning a range from 100 kHz – 10.7 MHz using an electro-optic modulator, whereas the probe beam is modulated to 200 Hz using an optical chopper. The choice of f dictates the penetration depth of heating – reducing the value of f will increase the penetration depth, and vice versa. Further technical details of our TDTR experimental setup, the various optical components used, etc. is provided in [37].

We direct the pump and probe beams to the sample surface and focus using the desired objective lens (Edmund Optics, Mitutoyo). We perform TDTR measurements at $1/e^2$ laser spot sizes (w_0) of 7.8 μm, 3.4 μm, or ~1.8 μm. At such small spot sizes, the localized temperature rise on the polymer surface could be significant enough to alter their molecular structure and physical properties. Thus, we lower the combined pump/probe powers to values of ~ 0.85 – 1.5 mW. This is to ensure that the steady state temperature rise across the polymer surface (ΔT_{ss}) is less than ~10K.

To improve the signal-to-noise ratio (SNR) at low probe powers, we utilize a 90:10 beam splitter that transmits ~90% of the reflected probe signal to the detector. Additionally, we ensure that the microtomed polymer surface is smooth enough to yield a specularly reflecting surface for reproducible TDTR measurements. To do so, we coat a SiO_2-Si substrate with a thin layer of Al and obtain a measure of its reflectance. The reflectance can be estimated by measuring the DC voltage generated by a reflected probe beam of known power, incident on the detector. We compare this value to that obtained on our Al coated polymer films and verify that they are no less than 10% apart.

TDTR measurements generate two output signals of interest - the in-phase (V_{in}) and out-of-phase (V_{out}), measured by a radio-frequency (RF) lock-in amplifier (SRS 844, Stanford Systems). We fit the negative ratio, $-V_{in}/V_{out}$, obtained as a function of time delay, to the isotropic three-dimensional heat diffusion model by Cahill et al. [35] This analysis requires four primary input parameters – thermal conductivities (Λ), thermal boundary conductance (G), volumetric heat capacities (C), and thicknesses (h), of the Al transducer layer and the underlying Al/PVDF film. We obtain C for both Al and PVDF

73

from literature, and employ the weighted mean method to deduce C for differing volume

fractions of Al in the Al/PVDF system. To estimate Λ_{Al}, we sputter a thin Al layer onto a

SiO_2-Si substrate and measure the sheet resistivity using the four-point probe method. We

use the Wiedemann-Franz Law to obtain Λ_{Al}. We use picosecond acoustic echoes

observed at short time delay in the V_{in} signal to estimate the thickness of the Al

transducer layer, following the method described in [34].

We adjust the thermal conductivity of the Al/PVDF layer, so the thermal model

predictions best match the experimental $-V_{in}/V_{out}$ datasets as a function of time delay.

Further details about the TDTR data analyses procedure, along with sensitivity and

uncertainty analyses, are detailed in [36].

High-Throughput Thermo-reflectance Mapping:

We utilize sub-micron resolution thermo-reflectance mapping to interrogate the

effects of microstructural inhomogeneities on thermal transport in Al/PVDF films. We

collect V_{in} and V_{out} signals as a function of position, at a single pump-probe delay time

[71]. We choose the delay time where the output ratio, $-V_{in}/V_{out}$, demonstrates maximum

sensitivity to the thermal conductivity of the Al/PVDF substrate. We collect all our

thermo-reflectance maps at a fixed delay time of $t = 500$ ps, with a pump modulation

frequency of $f = 10.7$ MHz or 500 kHz, and a $1/e^2$ laser spot size (w_0) of ~1.77 – 2.2 μm.

Pure PVDF samples are smoother than Al-PVDF samples. Thus, the spot-size of pure

PVDF polymer samples is small (~1.77 μm). As the Al volume fraction gets higher in the

polymer film, the sample surface gets comparatively rougher. The spot-size of the Al-PVDF film with $\phi = 50\%$ is ~2.2 μm.

We mount our samples on an automated 2-axis (XY) sample stage, fitted with DC servo actuators. We map areas of $\sim 10\ \mu m \times 10\ \mu m$, with a step-size of 500 nm. To verify that the polymer surface is in focus throughout the measurement, we measure w_0 at all four vertices of our maps and ensure that the variation is less than ~ 5%. We use the beam-offset method to measure w_0. At each position in the map, we record $-V_{in}/V_{out}$ *(t=500 ps)*. We use our TDTR thermal model to convert the ratio to thermal conductivity, as a function of position.

5.3. Results and Analyses:

5.3.1. Thermal Conductivity of Al-PVDF Films

In Figure 5.2. we describe the results of our TDTR experiments of Al/PVDF nanocomposite films. We plot the measured thermal conductivity values as a function of Al volume fraction (0 – 50%) in Figure 5.3, and compare our results with the Maxwell [100] and Nielsen-Lewis [101], [102], [105] model predictions.

In Figure 5.2. (a), we plot the ratio, $-V_{in}/V_{out}$, as a function of delay time for a pure PVDF polymer film, at three different laser spot sizes. In all three plots, we note that the ratio ($-V_{in}/V_{out}$) is suppressed by the presence of a possible strain wave at longer time delays (see red arrows). Wang et al. reported a similar phenomenon in the TDTR analyses of microtomed polymer fiber cross-sections coated with an Al transducer layer in [106]. They attributed this behavior to a possible thermo-elastic effect that occurs due

to a mismatch between the elastic constants of the Al transducer and the underlying soft polymer substrate. This mismatch likely induces a lateral stress component in the Al film which is relaxed by the emission of an acoustic wave that is related to the zero-order symmetric Lamb mode of the Al transducer. In our datasets, we note that this acoustic wave decays at a delay time of ~325, 650, and 1500 ps for laser spot sizes of 1.8 μm, 3.4 μm, and 7.8 μm respectively. This corresponds to a wave propagation velocity of ~ 5.2 nm ps^{-1}, in good agreement with the value (v_L = 5.44 nm ps^{-1}) reported in [106].

In Figure 5.2 (b), we plot the ratio for Al/PVDF films with varying volume fractions of Al nanoparticles. While the deviation occurring due to the acoustic strain wave is present in PVDF films with 10 vol.% Al, we observe that it disappears upon increasing the Al concentration to 30 and 50 vol.%. The addition of inorganic filler to a polymer matrix adds stiffness to the material, which increases its elastic modulus [107], [108]. Thus, the variance between the thermo-mechanical properties of the Al transducer and the underlying polymer is reduced, decreasing the amplitude of any lateral strain waves. Hence, our results provide a qualitative validation to the hypotheses presented in [106].

In Figure 5.2.(a), we fit our TDTR data using the thermal model and obtain the thermal conductivity (Λ) for pure PVDF to be 0.27 W/m-K for all laser spot sizes. This is in excellent agreement with the value of Λ reported in [8], for pure PVDF films prepared by melt-mixing and hot-pressing processes. Similarly, in Figure 5.2. (b), we obtain thermal conductivity values of 0.34, 0.48, and 0.58 W/m-K for PVDF films with Al volume fractions of 10, 30 and 50 % respectively. Thus, our results show that increasing

the Al filler concentration to 50 vol.% in a PVDF film enhances its thermal conductivity by ~100%.
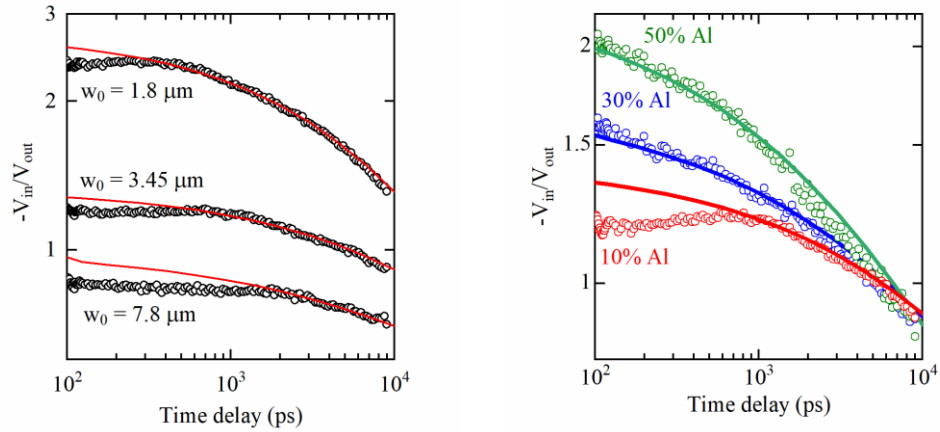
Figure 5.2. Bulk Thermal Conductivity in Al-PVDF Nanocomposites (a) We plot the ratio as a function of delay time for pure PVDF polymer film at three different spot sizes, as indicated in the figure. The appearance of acoustic strain waves is observed for all three spot sizes. In **(b)**, we plot the ratio as a function of time delay for Al-PVDF films as a function of Al volume fraction. We note that while the strain wave is visible at a volume fraction of 10% Al, it disappears upon increasing the Al volume fraction to 30% and eventually 50%.
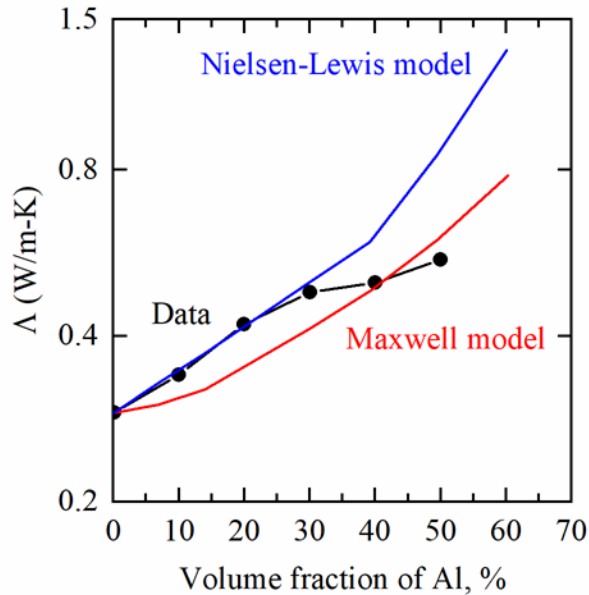
Figure 5.3. Summarizing the Thermal Conductivity in Al-PVDF films We plot the bulk thermal conductivity as a function of Al volume fraction. We compare our experimental data to predictions from the Maxwell model and Nielsen-Lewis model. Our data doesn't agree with the Maxwell model but shows reasonable agreement with the Nielsen-Lewis model between volume fractions of 10-20%.

5.3.2 Thermo-Reflectance Mapping of Al-PVDF Films

We present 2-dimensional thermal conductivity maps of PVDF films, with and without Al nanoparticles, in Figure 5.4. We collect these maps at a pump modulation frequency of 10.7 MHz, using a laser spot size of ~2 μm, and a delay time of 500 ps. At 500 ps, the lateral acoustic strain wave has propagated outside the area being probed, and the ratio is determined by the thermal conductivity of the underlying polymer substrate. Our maps have a spatial resolution of 500 nm.

In Figure 5.4. (a), we map the thermal conductivity in a microtomed PVDF film with no Al nanoparticles. As is expected for a pure polymer, we show that the Λ profile

of PVDF film is homogenous, with an average value of 0.29 $\pm$ 0.03 W/m-K. The spread in data is ~10%, which is within the systematic error margins of a standard TDTR experiment, with a small laser spot size of 1.77 μm.

On the other hand, there is a strong spatial variation in the thermal conductivity profile of the Al/PVDF film (50 vol.% Al). While the bulk thermal conductivity (Λ_{bulk}) of the Al/PVDF nanocomposite is 0.58 W/m-K, our map spans a total thermal conductivity range from 0.15 – 3.2 W/m-K, as shown in Figure 5.4. (b). At an [X, Y] position of ~ [6, 2] μm, the local thermal conductivity (Λ_{local}) approaches 3.2 W/m-K, a ~$6x$ enhancement of Λ_{bulk}. Over a radial distance of ~1.5 μm, there is a gradual reduction in the Λ_{local}, before it approaches the bulk value. A smaller increase (by $2x$) in the thermal gradient is observed at [X, Y] ~ [3, 1] μm, where Λ_{local} = 1.1 W/m-K. These areas likely contain Al nanoparticle clusters.
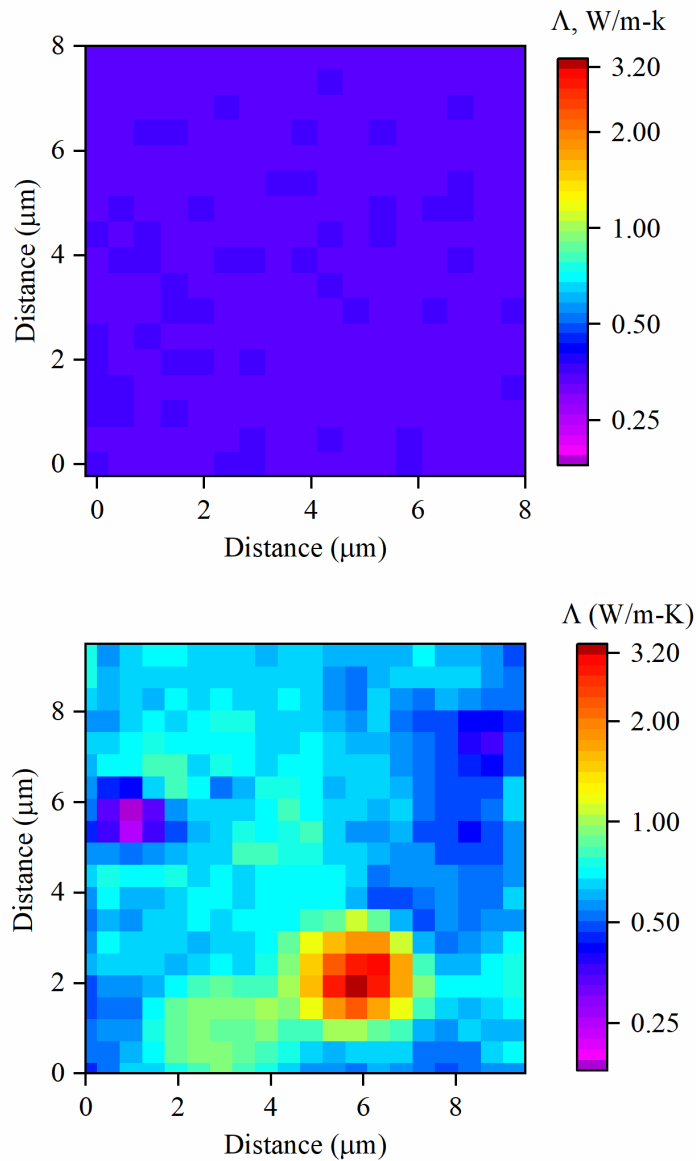
Figure 5.4. Thermo-reflectance Maps at High Frequency (10.7 MHz) We plot thermal conductivity maps of (a) PVDF with no Al and (b) PVDF with 50% vol. Al, with the same scale as shown in the right. Expectedly, the PVDF displays homogenous values of thermal conductivity, while the Al-PVDF nanocomposites features areas of low and high local thermal conductivity, depending on the presence of pores, polymer-rich regions, and/or coalesced Al particles.

Similarly, there are regions where $\Lambda_{local} \sim 0.25$ W/m-K (e.g., at [X, Y] $\sim$ [1, 5] μm). The thermal conductivity of Spurr's resin, as measured by TDTR, is ~ 0.2 W/m-K.

Thus, it is possible that areas featuring $\Lambda_{local} < 0.2$ W/m-K are indicative of pores that are infiltrated by epoxy resin during the embedding process. Our results show a significant structure-thermal property variation in the PVDF/Al nanocomposite material.

5.3.3 Frequency-Dependent Measurements of Thermal Conductivity

In Figures 5.5 and 5.6, we summarize frequency-dependent measurements of thermal conductivity in an Al/PVDF film (featuring 40 vol.% Al). The frequency *(f)* is related to the depth of penetration *(d)* by, $d = \sqrt{\frac{\Lambda}{\pi f C}}$ [36], where C is the volumetric heat capacity. Reducing the modulation frequency from 10.7 MHz to 0.1 MHz increases the penetration depth of heating from ~80 nm to ~860 nm, considering Λ_{bulk} ~ 0.5 W/m-K. Thus, at low frequencies, it is possible for us to interrogate buried pores and/or Al nanoparticle clusters.

$\underline{\Lambda_{bulk}}$ **from TDTR Scans:** We plot thermal conductivity as a function of heating frequency in an Al/PVDF film (40 vol.% Al) in Figure 5.5. We also show the correlated depth of heating *(d)* in the top *x* axis. For a heating depth of ~80 – 160 nm, we see that Λ_{bulk} is uniform at 0.5 W/m-K. Increasing the penetration depth to ~390 and ~860 nm reduces Λ_{bulk} to 0.45 W/m-K and 0.4 W/m-K respectively. This could be attributed to a non-uniform dispersion of Al nanoparticles in the PVDF matrix, or could be a small error in the spot size.
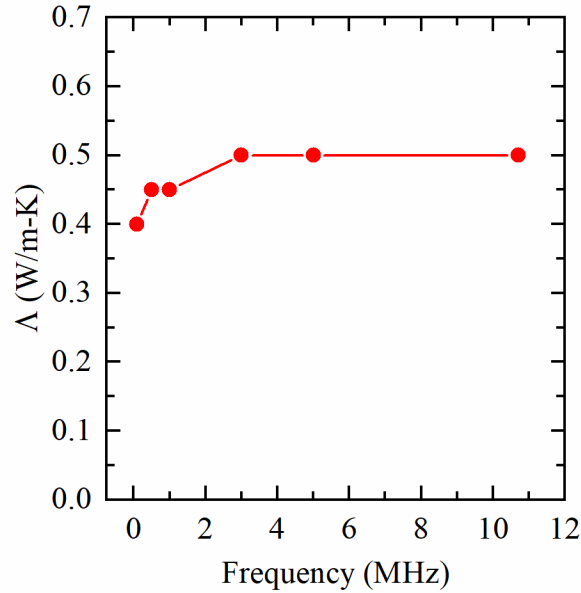
Figure 5.5. TDTR as a function of heating frequency Here, we plot thermal conductivity as a function of heating penetration depth. We note that the thermal conductivity decreases after the frequency is lowered to 1 MHz and 0.1 MHz by 20%.

Λ_{local} from Thermo-reflectance Maps: To further elucidate the effect of buried pores and/or Al clusters, we spatially profile the thermal conductivity in a 40 vol% Al/PVDF film in Figure 5.6. We interrogate the same region at two modulation frequencies. Figure 5.6. (a) shows a map at f = 10.7 MHz, while Figure 5.6. (b) shows a map at f = 0.5 MHz. These maps correspond to heating depths of ~ 80 nm and ~390 nm respectively.

While comparing both maps, we note a deviation in the Λ_{local} values in various regions. For example, at [X, Y] ~ [2, 2] μm, Λ_{local} (f = 10.7 MHz) ~ 0.9 W/m-K and Λ_{local} (f = 0.5 MHz) ~ 2 W/m-K, hinting at a presence of an Al cluster below the surface. Meanwhile, at [X, Y] ~ [7, 4] μm, Λ_{local} (f = 10.7 MHz) ~ 0.5 W/m-K and Λ_{local} (f = 0.5 MHz) ~ 0.25 W/m-K. This either points to the possibility of an underlying PVDF-rich

region with a low concentration of Al nanoparticles or a buried pore that got infiltrated with Spurr's resin.
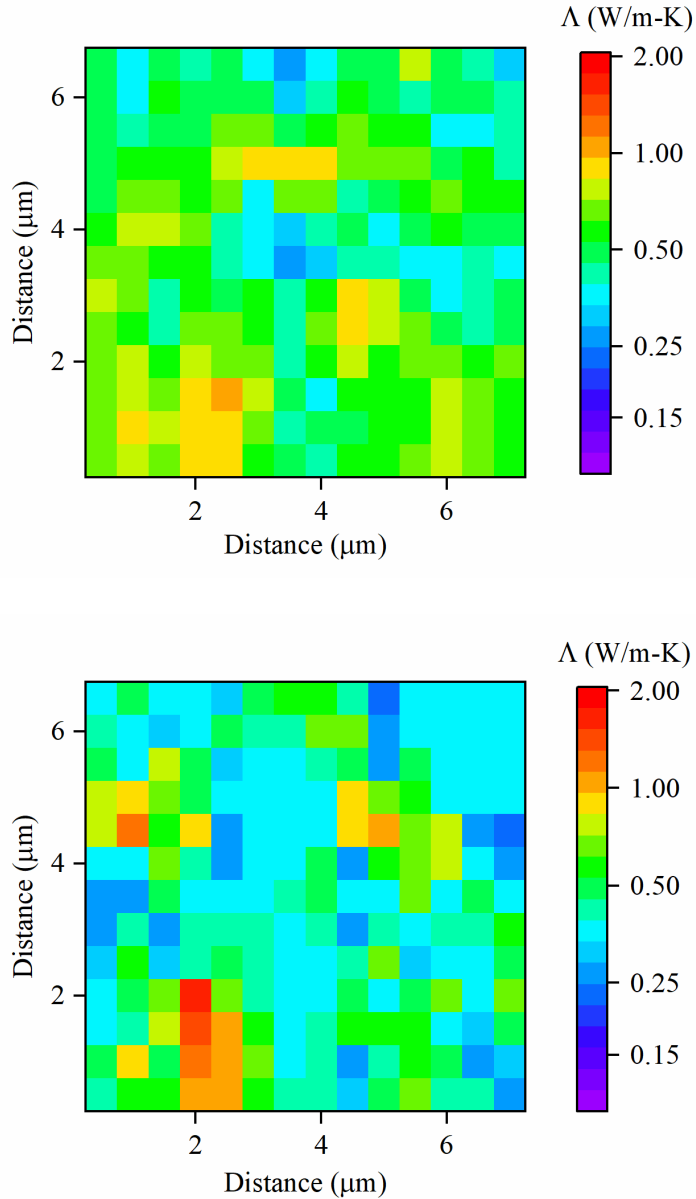
Figure 5.6. Thermo-reflectance Maps with Frequency Dependence We plot thermal conductivity maps of PVDF-Al nanocomposite films with an Al volume fraction of 40%. In (a) we show a map at high frequency (10.7 MHz) and in (b) we plot a map at low frequency (0.5 MHz) In (b) we see the presence of high thermal conductivity local regions possibly indicating the presence of a buried Al cluster (at x = 2, y = 2 μm). We also see the presence of areas with thermal conductivity below 0.25 W/m-K, likely indicating buried pores.

5.4. Discussion:

Maxwell-Eucken Model: Maxwell's model was the first to provide analytical solutions to calculate the effective electrical conductivity of a heterogenous material with randomly dispersed non-interacting spherical particles in a continuous medium[100]. Eucken[99] extended Maxwell's model to predict the thermal conductivity of particulate composites, as follows -

$$\Lambda_{bulk} = \left(\frac{K+2\emptyset}{K-\emptyset}\right)\Lambda_m, \quad (1)$$

$$\text{where } K = \frac{\Lambda_f + 2\Lambda_m}{\Lambda_f - \Lambda_m}. \quad (2)$$

Here, Λ_m denotes the thermal conductivity of the matrix material, Λ_f is the thermal conductivity of the particulate filler components, $\emptyset$ is the volume fraction of the particulate filler.

At lower $\emptyset$ ($\emptyset < 20$ %), Al spheres are possibly spaced far apart from each other. Hence, it is likely that there is negligible inter-particle interaction [109], [110]. This could, in theory, result in more accurate predictions of thermal conductivity for $\emptyset < 20$, but both our experimental data and previous results report otherwise. Our measured values for Λ_{bulk} are not in agreement with the M-E model predictions. Similarly, except at very low volume fractions ($\emptyset > 5$), Zhou et al. report that the Maxwell-Eucken model underpredicts thermal conductivity for Al-PVDF composites [8].

Nielsen-Lewis Model: Unlike the Maxwell model, the Nielsen-Lewis model takes into account the thermo-physical effects of particle interactions, by incorporating a wide variety of particle shapes, sizes and packing fractions [103], [109]. The Nielsen-Lewis model is given by –

$$\Lambda_{bulk} = \left(\frac{1+A.B.\emptyset}{1-B.\eta\,\emptyset}\right)\Lambda_m, \text{ where } B = \left(\frac{\frac{\Lambda_f}{\Lambda_m}-1}{\frac{\Lambda_f}{\Lambda_m}-A}\right) \text{ and } \eta = 1 + \left(\frac{1-\emptyset_m}{\emptyset_m^2}\right)\emptyset - (3)$$

A is the shape factor, which depends on the shape and aspect ratio of the filler materials, $\emptyset_m$ is the maximum packing fraction of the dispersed particles. For a random distribution of spherical particles, A = 1.5 and $\emptyset_m$ = 0.637, taken from [109]. The Nielsen-Lewis model shows excellent agreement with our experimental data at $\emptyset$ < 0.30, however it overpredicts the thermal conductivity at higher $\emptyset$.

We, now, attempt to explain the sources of discrepancy in the predicted versus measured Λ_{bulk} in our Al-PVDF composites. Both the Maxwell-Eucken and Nielsen-Lewis models rely on effective medium approximations and treat composites as "macroscopically homogenous" materials [103]. They offer an estimate of the effective bulk thermal conductivity of composites, knowing the thermo-physical properties and volume fractions of each component. However, our ultrastructural analyses and thermo-reflectance mapping data reveal the presence of several structural inhomogeneities that could likely influence local and effective thermal properties of these Al-PVDF composites.

85

(i) **Effects of Pores:**

The presence of porous networks has a deleterious effect on thermal conductivity. Hence foams and cellular materials often feature highly insulating properties. Image processing of scanning electron micrographs shows an increase in porosity in the Al-PVDF composite films with increasing Al volume fractions. These pores are likely "air pockets" that offer discontinuities in thermal conduction pathways. The presence of solid-gas boundaries changes our heat transfer problem from strictly solid-solid conduction to include gas convection, gas conduction, and radiation components. This could possibly result in an overall decrease in thermal conductivity. Thus, to better predict the thermal conductivity in particulate composites with $\emptyset < 0.40$, it is important to consider the effects of heat transfer regimes across solid-gas boundaries using porous media modelling techniques.

(ii) Effects of Metal-Polymer Interfacial Resistance:

The primary heat carrier in metals are electrons, whereas, in polymers, heat is carried by lattice vibrations (or phonons). At metal-polymer interfaces, these heat carriers undergo scattering. The probability of transmission after scattering will depend on the extent of acoustic impedance mismatch or available energy states mismatch on both sides of the interface [111], [112]. Scattering of heat carriers shortens their mean free paths and reduces the overall thermal conductivity of the material.

Furthermore, as the size of the particulate filler decreases, there is an increase in the interfacial area per unit volume, likely resulting in additional scattering sites. This could

further decrease the effective conductivity. Hence, in our Al-PVDF composite films featuring 80 nm Al spheres, interfacial thermal resistance cannot be neglected. In addition, the metal-polymer interfaces could feature imperfect mechanical/chemical bonding, which could lead to an additional drop in the effective thermal conductivity. The Nielsen-Lewis model does not include contributions from the interfacial thermal resistance. Hence, we hypothesize that this could be another reason why our experimental values are lower than the Nielsen-Lewis model predictions.

On the Percolative Effects of Al Agglomerates:

Finally, we want to add a comment on the effects of Al nanoparticle percolation on local thermal conductivity values. In our Al-PVDF thermal conductivity maps, we note an increase in the local thermal conductivity values in the presence of Al agglomerates. Each agglomerate is likely made up of ~10s of closely packed Al nanoparticles. This could possibly result in the creation of highly conductive heat propagation channels. Therefore, unsurprisingly, at the core of the agglomerates, we show that Λ_{local} increases by up to ~250 times the bulk thermal conductivity values, see Figure. 5.7. We attribute this to the percolative effects of Al nanoparticles stacked in close contact with each other. This result is concurrent with other experimental investigations that report an enhancement of thermal conductivity by several orders of magnitude upon adding high aspect ratio fillers to polymer matrices [113]–[115].

There is considerable debate over the influence of particulate filler percolation in determining the effective thermal conductivity of metal-polymer composites. Some

studies show that above a certain critical volume fraction of particulate filler in a composite (termed as percolation threshold), the rise in effective thermal conductivity stops slowly increasing, but rather shoots up exponentially [116], [117]. Some studies show a continued linear increase in thermal conductivity as a function of filler volume fraction [118], [119]. In our thermal conductivity maps, while we do observe local spots that feature extremely high thermal conductivity, we don't observe a significant impact on the effective bulk thermal conductivity in our Al-PVDF composite films that could be attributed to percolation effects.
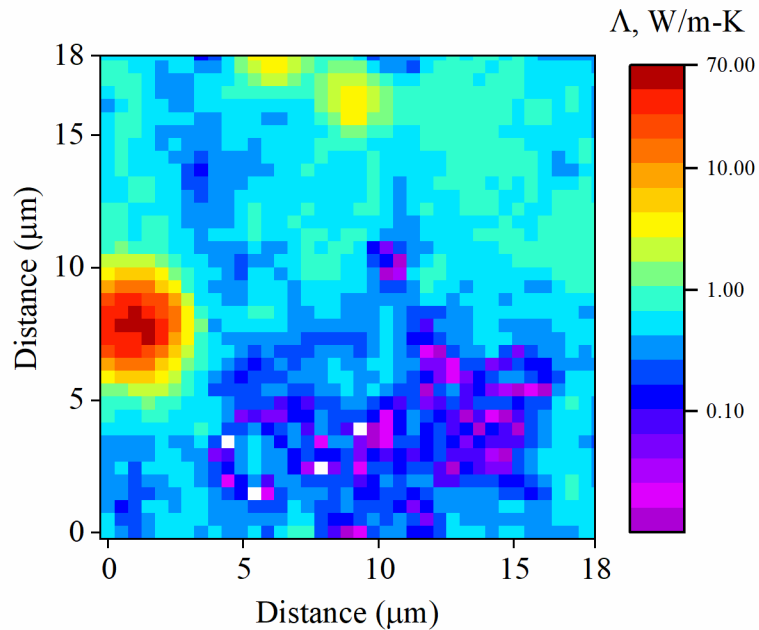
Figure 5.7. Thermo-reflectance Map at High Frequency (10.7 MHz) Showing High Λ Values
We plot a thermal conductivity map of PVDF with 50% vol. Al. In this map, we show a Λ_{local} value of ~77 W/m-K at the core of an Al agglomerate ~ 250 times higher than the effective thermal conductivity of the Al-PVDF polymer film. Moreover, we also show what appears to be pores where the Λ_{local} value appears to be < 0.1 W/m-K.

The Influence of Al Volume Fraction on Combustion:

Several groups have studied the combustion performances of Al-PVDF nanocomposites as a function of Al volume fraction. At $\emptyset = 10$, laser heating of the Al-PVDF film couldn't result in sustained combustion [6], [7], [97]. However, at $\emptyset > 30$, they achieve self-sustained combustion propagation in Al-PVDF films. They hypothesize that this is due to enhanced heat conduction on account of the addition of highly conductive Al nanoparticle fillers. We experimentally demonstrate that increasing the volume fraction of Al to 50% enhances the overall thermal conductivity of the Al-PVDF film by ~100%. This could, in theory, result in highly conductive heat propagation channels that aid in rapid energy transfer. On the contrary, an Al volume fraction of 10% only increases the effective thermal conductivity by ~10%, suggesting that the effective thermal conductivity in these films is dominated by PVDF, and not Al.

5.5. Conclusions

In conclusion, we show that increasing Al filler content by 50 vol.% enhances the bulk thermal conductivity of the PVDF matrix by a factor of 2. However, at the micrometer length-scale, the Al-PVDF nanocomposite features several Al clusters and possible percolation networks, locally increasing the thermal conductivities by factors of greater than 200. This creates conductive pathways for heat to propagate and combustion to be self-sustained upon ignition. Therefore, combustion experiments and energetics investigations observe that although at 10% vol. Al, they do not see evidence of sustained

combustion upon igniting, increasing the Al concentration to 30% and eventually 50% greatly increases the rate of burn, as well as allows for sustained combustion.

Chapter 6.

Conclusions

In this dissertation, I explore nanoscale transport properties using Time-Domain Thermo-Reflectance (TDTR) in two distinct systems – (i) ferromagnetic Co-Fe alloys, and (ii) nano-energetic Al-PVDF composite materials. I also use Thermo-Reflectance mapping at a single time delay to spatially probe the thermal conductivity in these materials.

In addition, I investigate magnetization dynamics in Co-Fe alloys, using the Time-Resolved Magneto-Optic Kerr technique (TR-MOKE). I also utilize the phenomenological three-temperature model (3TM) to investigate the role of quasi-particle interactions on the magnetization dynamics of Co-Fe thin films.

Summary of Results:

In my work on ferromagnetic Co-Fe alloy systems, I show that composition has a huge effect on both thermal and magnetic transport. This could be attributed to the change in the electronic band structure as a function of composition, and the quasi-particle interactions that arise due to Fermi energy band variations. Through analyses presented in this dissertation, I explore the interplay between spin, charge, and lattice degrees of freedom and how they influence thermal transport and magnetic properties in ferromagnetic alloys.

I summarize my research findings from Chapter 3 – 5 in the subsequent sections of this chapter.

Magnetization Dynamics in Co-Fe Alloys:

(i) Co-concentrations that feature long-lived magnetic precessions (i.e., low magnetic damping) at the nanosecond timescale, also demonstrate longer-lived non-equilibrium magnetization dynamics at the femtosecond regime.

(ii) Analyzing the energy dynamics using the phenomenological three-temperature model (3TM) shows that the electron-phonon interactions depend strongly on composition. On the contrary, the electron-magnon interactions show a weaker dependence on composition.

(iii) Co-concentrations that feature extended non-equilibrium dynamics have weak electron-phonon interaction strengths.

Nanoscale Thermal Transport in Co-Fe Alloys:

(i) The thermal conductivity has a strong dependence on Co-concentration. The thermal conductivity is not strongly affected by alloy disorder.

(ii) Co-concentrations between 20 – 50 at. wt% demonstrate significantly high non-electronic contribution to thermal conductivity.

(iii) We see two possible explanations for large non-electronic thermal conductivity – electronic scattering processes where charge currents are degraded without a corresponding degradation in thermal gradients. Or more likely in my view, the excess non-electronic thermal conductivity is due to magnons.

Nanoscale Thermal Transport in Al-PVDF Energetic Composites

(i) Adding high conductivity particulate filler materials (like Al) to insulating polymer films (like PVDF) increases the overall thermal conductivity of the nanocomposite. This, could, enhance the flame propagation characteristics of Al-PVDF composites above Al volume fraction.

(ii) Using high throughput thermo-reflectance mapping, I can create regio-specific thermal conductivity profiles that interrogate the effects of Al nanoparticle clusters, PVDF rich regions, and pores within the Al-PVDF composite film. These maps, when correlated with high-resolution high-speed camera imaging of combustion experiments, are useful in predicting burn rates and/or directions of flame spread.

Appendix 1. Wiedemann-Franz Empirical Law

The empirical Wiedemann-Franz Law predicts that the electronic thermal conductivity ($\Lambda_{electron}$) is proportional to the product of the electrical thermal conductivity (σ) and the measurement temperature (T). The constant of proportionality is referred to as the Lorenz number (L), and is equal to the Sommerfeld value, $L_0 = 2.44 \times 10^{-8}\ W\Omega K^{-2}$.

$$\Lambda_{electron} = \sigma \times L_0 \times T$$

Derivation:

According to the Drude model for electrical transport, the expression for electrical conductivity (σ) is given by,

$$\sigma = \frac{e^2 \times n \times \tau_e}{m^*} - (1)$$

where m^* is the effective electron mass, n is the effective number of charge carriers per unit volume, τ_e is the electron energy relaxation time, and e is the electronic charge.

Also, the kinetic theory for electron thermal transport predicts that the electronic contribution to thermal conductivity ($\Lambda_{electron}$) is given by,

$$\Lambda_{electron} = \frac{1}{3} \times c_e \times v_F^2 \times \tau_k - (2)$$

where v_F is the Fermi velocity

c_e is given by the expression, $\qquad c_e = \frac{\pi^2}{2} \times \left(\frac{k_B{}^2 T}{\epsilon_F}\right) \times n - (3)$

where k_B is the Boltzmann constant, and ϵ_F is the Fermi energy and is given by,

$$\epsilon_F = \frac{\hbar^2 \times k_F^2}{2m^*}.$$

v_F is given by the expression, $v_F = \frac{\hbar \times k_F}{m^*}$, where k_F is the Fermi wave-vector.

To derive the Wiedemann-Franz Empirical Law, we consider the ratio of the electronic thermal conductivity to electrical conductivity. We also make substitutions for the electronic heat capacity, and use the expressions for the Fermi energy and Fermi velocity to obtain the following result –

$$\frac{\Lambda_{electron}}{\sigma} = \frac{\pi^2 \times k_B^2}{3 \times e^2} \frac{\tau_k}{\tau_e} \times T = L_0 \times \frac{\tau_k}{\tau_e} \times T - (4) \text{ where } L_0 = \frac{\pi^2 \times k_B^2}{3 \times e^2}$$

According to Avery et al. [120], Equation (4) can be considered the Wiedemann-Franz Law if the condition,

$$\boldsymbol{\tau_k = \tau_e} - (5)$$

is satisfied. i.e., when the thermal and electrical energy scattering processes have equivalent relaxation times. In such scenarios, charge carriers (conduction electrons) are considered to have long mean free paths and undergo scattering at the same rates.

However, it is worth noting that a disagreement to this explanation exists in Ref. [83]. Authors Ashcroft and Mermin state that the scattering rates (i.e. frequency of collisions) do not adequately describe the applicability of the Wiedemann-Franz Law, as is reported in [120] and stated in Equation (5). Rather, it is the nature of scattering processes (elastic versus inelastic) that determine its pertinence.

Elastic collisions conserve energy, and thus, degrade thermal gradients with a corresponding and equivalent degradation in charge currents. For metals, this condition is

reasonably met either at extremely low temperatures ($0K < T < \sim10K$) or above their Debye temperatures. At high temperatures, scattering processes are dominated by quasi-elastic electron-phonon scattering, whereas at low temperatures, they are dominated by elastic electron-impurity and/or lattice defect scattering. This ensures that the WF-Law holds.

Violations of the WF Law Due to Inelastic Scattering:

At interim temperatures, where $10K < T < \sim300K$, it is experimentally determined that

$$\Lambda_{electron} < \sigma \times L_0 \times T$$

for several material systems. This alludes to the presence of inelastic scattering processes that could produce electronic energy losses of the order $\sim k_B T$. These inelastic scattering processes could include small angle electron-phonon scattering or electron-magnon scattering processes.

Violations of the WF Law and the Applicability of the Smith-Palmer Equation:

Another possible explanation for the violation of the WF Law could be attributed to the non-electronic contribution to the thermal conductivity. Non-electronic contributions typically occur from phonons (lattice vibrations) and/or magnons (collective spin excitations). When non-electronic contributions are considered, an extended form of the WF Law, called the Smith-Palmer equation is considered [85]. This equation is given by:

$$\Lambda_{total} = A.\sigma.L_0.T + B$$

where A and B are material specific empirical constants.

When A = 1 and B = 0, this equation becomes the WF-Law. B = 0, implies that all the contribution to thermal conductivity comes from charge carriers. A = 1 implies that both heat currents and charge currents are affected equivalently by electronic scattering. However, for several metal alloy systems, it has been experimentally shown that A < 1 and 2 < B < 20 (W/m-K) [67]. When $B \neq 0$, it can be assumed that a non-electronic component exists. Similarly, when A < 1, it is indicative of inelastic scattering processes. Thus, we find that substantial non-electronic contributions to the total thermal conductivity could also cause a break-down of the Wiedemann-Franz Law.

In addition, in materials where extremely strong inter-particle interactions are observed, the transport behavior is almost "fluid-like" [121], [122]. Thus, in these systems, the Kinetic theory of transport doesn't apply, and hydrodynamics theory needs to be considered. In such cases, again, we see that the Wiedemann-Franz Law is violated.

References:

[1]   M. A. W. Schoen *et al.*, "Ultra-low magnetic damping of a metallic ferromagnet," *Nat. Phys.*, vol. 12, no. 9, pp. 839–842, 2016.

[2]   A. J. Lee *et al.*, "Metallic ferromagnetic films with magnetic damping under $1.4 \times 10\text{-}3$," *Nat. Commun.*, vol. 8, no. 1, pp. 1–6, 2017.

[3]   Y. Wei, W. Zhang, B. Lv, X. Xu, S. Xi, and Z. Ma, "Ultralow magnetic damping of a common metallic ferromagnetic film," *Sci. Adv.*, vol. 7, no. 4, pp. 1–7, 2021.

[4]   H. J. Qin *et al.*, "Long-living terahertz magnons in ultrathin metallic ferromagnets," *Nat. Commun.*, vol. 6, pp. 1–8, 2015.

[5]   Y. Zhou, J. Tranchida, Y. Ge, J. Murthy, and T. S. Fisher, "Atomistic simulation of phonon and magnon thermal transport across the ferromagnetic-paramagnetic transition," *Phys. Rev. B*, vol. 101, no. 22, p. 224303, 2020.

[6]   C. Huang, G. Jian, J. B. De Lisio, H. Wang, and M. R. Zachariah, "Electrospray deposition of energetic polymer nanocomposites with high mass particle loadings: A prelude to 3D printing of rocket motors," *Adv. Eng. Mater.*, vol. 17, no. 1, pp. 95–101, 2015.

[7]   X. Ke *et al.*, "Safe preparation, energetic performance and reaction mechanism of corrosion-resistant Al/PVDF nanocomposite films," *J. Mater. Chem. A*, vol. 6, no. 36, pp. 17713–17723, 2018.

[8]   W. Zhou, J. Zuo, and W. Ren, "Thermal conductivity and dielectric properties of Al/PVDF composites," *Compos. Part A Appl. Sci. Manuf.*, vol. 43, no. 4, pp. 658–664, 2012.

[9]   J. C. Huss *et al.*, "Climate-Dependent Heat-Triggered Opening Mechanism of Banksia Seed Pods," *Adv. Sci.*, vol. 1700572, 2017.

[10]   J. C. Huss *et al.*, "Temperature-induced self-sealing capability of Banksia follicles," *J. R. Soc. Interface*, vol. 15, no. 143, 2018.

[11]   T. He, B. B. Lamont, and K. S. Downes, "Banksia born to burn," *New Phytol.*, vol. 191, no. 1, pp. 184–196, 2011.

[12]   A. B. Wardrop, "The opening mechanism of follicles of some species of Banksia," *Aust. J. Bot.*, vol. 31, no. Stearn 1966, pp. 485–500, 1983.

[13]   a M. Gill, "Fire and the opening of <I>Banksia ornata</I> F. Muell. Follicles,"
Aust. J. Bot., vol. 24, no. 3, pp. 329–335, 1976.

[14]   U. G. K. Wegst, H. Bai, E. Saiz, A. P. Tomsia, and R. O. Ritchie, "Bioinspired
structural materials," *Nat. Mater.*, vol. 14, no. 1, pp. 23–36, Oct. 2014.

[15]   K. Werner, L. Pommer, and M. Broström, "Thermal decomposition of
hemicelluloses," *J. Anal. Appl. Pyrolysis*, vol. 110, no. August, pp. 130–137, 2014.

[16]   H. Tributsch and S. Fiechter, "The material strategy of fire-resistant tree barks," in
High Performance Structures and Materials IV, 2008, vol. I, pp. 43–52.

[17]   G. Bauer, T. Speck, J. Blömer, J. Bertling, and O. Speck, "Insulation capability of
the bark of trees with different fire adaptation," *J. Mater. Sci.*, vol. 45, no. 21, pp.
5950–5959, 2010.

[18]   A. Kirilyuk, A. V Kimel, and T. Rasing, "Ultrafast optical manipulation of
magnetic order," *Rev. Mod. Phys.*, vol. 82, no. September, p. 2731, 2010.

[19]   E. Beaurepaire, J. C. Merle, A. Daunois, and J. Y. Bigot, "Ultrafast spin dynamics
in ferromagnetic nickel," *Phys. Rev. Lett.*, vol. 76, no. 22, pp. 4250–4253, 1996.

[20]   F. Hellman *et al.*, "Interface-Induced Phenomena in Magnetism," *Rev. Mod. Phys.*,
vol. 89, no. June, p. 025006, 2017.

[21]   W. L. McMillan, "Transition Temperature of Strong-Coupled Superconductors,"
Phys. Rev., vol. 167, no. 2, pp. 331–344, Mar. 1968.

[22]   P. B. Allen, "Theory of thermal relaxation of electrons in metals," *Phys. Rev. Lett.*,
vol. 59, no. 13, pp. 1460–1463, 1987.

[23]   B. Koopmans *et al.*, "Explaining the paradoxical diversity of ultrafast laser-
induced demagnetization," *Nat. Mater.*, vol. 9, no. 3, pp. 259–265, 2010.

[24]   Z. Chen and L.-W. Wang, "Role of initial magnetic disorder: A time-dependent ab
initio study of ultrafast demagnetization mechanisms," *Sci. Adv.*, vol. 5, no. 6, p.
eaau8000, Jun. 2019.

[25]   K. Carva, M. Battiato, and P. M. Oppeneer, "Ab initio investigation of the Elliott-
Yafet electron-phonon mechanism in laser-induced ultrafast demagnetization,"
Phys. Rev. Lett., vol. 107, no. 20, p. 207201, 2011.

[26] E. Carpene, E. Mancini, C. Dallera, M. Brenna, E. Puppin, and S. De Silvestri, "Dynamics of electron-magnon interaction and ultrafast demagnetization in thin iron films," *Phys. Rev. B - Condens. Matter Mater. Phys.*, vol. 78, no. 17, pp. 1–6, 2008.

[27] S. Eich *et al.*, "Band structure evolution during the ultrafast ferromagnetic-paramagnetic phase transition in cobalt," *Sci. Adv.*, vol. 3, no. 3, pp. 1–9, 2017.

[28] E. Carpene, H. Hedayat, F. Boschini, and C. Dallera, "Ultrafast demagnetization of metals: Collapsed exchange versus collective excitations," *Phys. Rev. B - Condens. Matter Mater. Phys.*, vol. 91, no. 17, pp. 1–8, 2015.

[29] P. Tengdin *et al.*, "Critical behavior within 20 fs drives the out-of-equilibrium laser-induced magnetic phase transition in nickel," *Sci. Adv.*, vol. 4, no. 3, pp. 1–9, 2018.

[30] J. Kimling, J. Kimling, R. B. Wilson, B. Hebler, M. Albrecht, and D. G. Cahill, "Ultrafast demagnetization of FePt:Cu thin films and the role of magnetic heat capacity," *Phys. Rev. B - Condens. Matter Mater. Phys.*, vol. 90, no. 22, pp. 1–9, 2014.

[31] R. B. Wilson and S. Coh, "Parametric dependence of hot electron relaxation timescales on electron-electron and electron-phonon interaction strengths," *Commun. Phys.*, vol. 3, no. 1, 2020.

[32] K. Gilmore, Y. U. Idzerda, and M. D. Stiles, "Identification of the dominant precession-damping mechanism in Fe, Co, and Ni by first-principles calculations," *Phys. Rev. Lett.*, vol. 99, no. 2, pp. 1–4, 2007.

[33] V. Kamberský, "On the Landau–Lifshitz relaxation in ferromagnetic metals," *Can. J. Phys.*, vol. 48, no. 24, pp. 2906–2911, 1970.

[34] G. T. Hohensee, W. P. Hsieh, M. D. Losego, and D. G. Cahill, "Interpreting picosecond acoustics in the case of low interface stiffness," *Rev. Sci. Instrum.*, vol. 83, no. 11, 2012.

[35] D. G. Cahill, "Analysis of heat flow in layered structures for time-domain thermoreflectance," *Rev. Sci. Instrum.*, vol. 75, no. 12, pp. 5119–5122, 2004.

[36] P. Jiang, X. Qian, and R. Yang, "Tutorial: Time-domain thermoreflectance (TDTR) for thermal property characterization of bulk and thin film materials," *J. Appl. Phys.*, vol. 124, no. 16, 2018.

[37] M. J. Gomez, K. Liu, J. G. Lee, and R. B. Wilson, "High sensitivity pump-probe measurements of magnetic, thermal, and acoustic phenomena with a spectrally tunable oscillator," *Rev. Sci. Instrum.*, vol. 91, no. 2, 2020.

[38] K. Kang, Y. K. Koh, C. Chiritescu, X. Zheng, and D. G. Cahill, "Two-tint pump-probe measurements using a femtosecond laser oscillator and sharp-edged optical filters," *Rev. Sci. Instrum.*, vol. 79, no. 11, 2008.

[39] P. B. Johnson and R. W. Christy, "Optical constants of transition metals," *Phys. Rev. B*, vol. 9, no. 12, pp. 5056–5070, 1974.

[40] P. B. Johnson and R. W. Christy, "Optical Constant of the Nobel Metals," *Phys. Rev. B*, vol. 6, no. 12, pp. 4370–4379, 1972.

[41] M. A. Ordal, R. J. Bell, R. W. Alexander, L. A. Newquist, and M. R. Querry, "Optical properties of Al, Fe, Ti, Ta, W, and Mo at submillimeter wavelengths," *Appl. Opt.*, vol. 27, no. 6, p. 1203, 1988.

[42] M. Haag, C. Illg, and M. Fähnle, "Role of electron-magnon scatterings in ultrafast demagnetization," *Phys. Rev. B - Condens. Matter Mater. Phys.*, vol. 90, no. 1, pp. 1–6, 2014.

[43] E. G. Tveten, A. Brataas, and Y. Tserkovnyak, "Electron-magnon scattering in magnetic heterostructures far out of equilibrium," *Phys. Rev. B - Condens. Matter Mater. Phys.*, vol. 92, no. 18, pp. 1–5, 2015.

[44] M. Farle, "Ferromagnetic resonance of ultrathin metallic layers," *Reports Prog. Phys.*, vol. 61, no. 7, pp. 755–826, 1998.

[45] M. A. W. Schoen *et al.*, "Magnetic properties in ultrathin 3d transition-metal binary alloys. II. Experimental verification of quantitative theories of damping and spin pumping," *Phys. Rev. B*, vol. 95, no. 13, pp. 1–9, 2017.

[46] J. Kuneš and V. Kamberský, "First-principles investigation of the damping of fast magnetization precession in ferromagnetic (formula presented) metals," *Phys. Rev. B - Condens. Matter Mater. Phys.*, vol. 65, no. 21, pp. 1–3, 2002.

[47] M. Fähnle and D. Steiauf, "Breathing Fermi surface model for noncollinear magnetization: A generalization of the Gilbert equation," *Phys. Rev. B - Condens. Matter Mater. Phys.*, vol. 73, no. 18, pp. 1–5, 2006.

[48] P. B. Allen, "Empirical electron-phonon values from resistivity of cubic metallic elements," *Phys. Rev. B*, vol. 36, no. 5, pp. 2920–2923, 1987.

[49] B. Koopmans, J. J. M. Ruigrok, F. Dalla Longa, and W. J. M. De Jonge, "Unifying ultrafast magnetization dynamics," *Phys. Rev. Lett.*, vol. 95, no. 26, pp. 1–4, 2005.

[50] W. Zhang, W. He, X. Q. Zhang, Z. H. Cheng, J. Teng, and M. Fähnle, "Unifying ultrafast demagnetization and intrinsic Gilbert damping in Co/Ni bilayers with electronic relaxation near the Fermi surface," *Phys. Rev. B*, vol. 96, no. 22, pp. 1–7, 2017.

[51] S. Mathias *et al.*, "Probing the timescale of the exchange interaction in a ferromagnetic alloy," *Proc. Natl. Acad. Sci. U. S. A.*, vol. 109, no. 13, pp. 4792–4797, 2012.

[52] S. D. Brorson *et al.*, "Femtosecond room-temperature measurement of the electron-phonon coupling constant in metallic superconductors," *Phys. Rev. Lett.*, vol. 64, no. 18, pp. 2172–2175, 1990.

[53] A. Gloskovskii *et al.*, "Electron emission from films of Ag and Au nanoparticles excited by a femtosecond pump-probe laser," *Phys. Rev. B - Condens. Matter Mater. Phys.*, vol. 77, no. 19, pp. 1–11, 2008.

[54] W. L. Chan, R. S. Averback, D. G. Cahill, and A. Lagoutchev, "Dynamics of femtosecond laser-induced melting of silver," *Phys. Rev. B - Condens. Matter Mater. Phys.*, vol. 78, no. 21, pp. 1–8, 2008.

[55] U. Atxitia, T. A. Ostler, R. W. Chantrell, and O. Chubykalo-Fesenko, "Optimal electron, phonon, and magnetic characteristics for low energy thermally induced magnetization switching," *Appl. Phys. Lett.*, vol. 107, no. 19, 2015.

[56] F. Jakobs *et al.*, "Unifying femtosecond and picosecond single-pulse magnetic switching in Gd-Fe-Co," *Phys. Rev. B*, vol. 103, no. 10, pp. 18–22, 2021.

[57] C. S. Davies *et al.*, "Pathways for Single-Shot All-Optical Switching of Magnetization in Ferrimagnets," *Phys. Rev. Appl.*, vol. 13, no. 2, p. 1, 2020.

[58] T. A. Ostler *et al.*, "Ultrafast heating as a sufficient stimulus for magnetization reversal in a ferrimagnet," *Nat. Commun.*, vol. 3, 2012.

[59] A. Ceballos *et al.*, "Role of element-specific damping in ultrafast, helicity-independent, all-optical switching dynamics in amorphous (Gd,Tb)Co thin films," *Phys. Rev. B*, vol. 103, no. 2, p. 24438, 2021.

[60] W. F. Maier, K. Stowe, and S. Sieg, "Combinatorial and high-throughput materials science," *Angew. Chemie - Int. Ed.*, vol. 46, no. 32, pp. 6016–6067, 2007.

[61] J. Geng, I. C. Nlebedim, M. F. Besser, E. Simsek, and R. T. Ott, "Bulk Combinatorial Synthesis and High Throughput Characterization for Rapid Assessment of Magnetic Materials: Application of Laser Engineered Net Shaping (LENS^{TM})," *JOM*, vol. 68, no. 7, pp. 1972–1977, 2016.

[62] H. Koinuma and I. Takeuchi, "Combinatorial solid-state chemistry of inorganic materials," *Nature Materials*, vol. 3, no. 7. pp. 429–438, 2004.

[63] I. Takeuchi, J. Lauterbach, and M. J. Fasolka, "Combinatorial materials synthesis," *Mater. Today*, vol. 8, no. 10, pp. 18–26, 2005.

[64] X. Wu, Z. Liu, and T. Luo, "Magnon and phonon dispersion, lifetime, and thermal conductivity of iron from spin-lattice dynamics simulations," *J. Appl. Phys.*, vol. 123, no. 8, 2018.

[65] S. Srichandan *et al.*, "Magnon scattering in the transport coefficients of CoFe thin films," *Phys. Rev. B*, vol. 98, no. 2, pp. 1–5, 2018.

[66] "Mohan, Ramya, et al. 'Electron-Phonon Scattering governs both Ultrafast and Precessional Magnetization Dynamics in Co-Fe Alloys.' arXiv preprint arXiv:2107.11699 (2021)."

[67] X. Zheng, D. G. Cahill, P. Krasnochtchekov, R. S. Averback, and J. C. Zhao, "High-throughput thermal conductivity measurements of nickel solid solutions and the applicability of the Wiedemann-Franz law," *Acta Mater.*, vol. 55, no. 15, pp. 5177–5185, 2007.

[68] W. Fulkerson, J. P. Moore, and D. L. McElroy, "Comparison of the thermal conductivity, electrical resistivity, and seebeck coefficient of a high-purity iron and an armco iron to 1000°C," *Journal of Applied Physics*, vol. 37, no. 7. pp. 2639–2653, Jun-1966.

[69] J. C. Zhao, X. Zheng, and D. G. Cahill, "High-throughput diffusion multiples," *Mater. Today*, vol. 8, no. 10, pp. 28–37, 2005.

[70] S. Cao and J. C. Zhao, "Application of dual-anneal diffusion multiples to the effective study of phase diagrams and phase transformations in the Fe-Cr-Ni system," *Acta Mater.*, vol. 88, pp. 196–206, 2015.

[71] S. Huxtable, D. G. Cahill, V. Fauconnier, J. O. White, and J. C. Zhao, "Thermal conductivity imaging at micrometre-scale resolution for combinatorial studies of materials," *Nat. Mater.*, vol. 3, no. 5, pp. 298–301, 2004.

[72]   P. D. Desai, H. M. James, and C. Y. Ho, "Electrical Resistivity of Aluminum and Manganese," *J. Phys. Chem. Ref. Data*, vol. 13, no. 4, pp. 1131–1172, 1984.

[73]   L. J. van der PAUW, "A METHOD OF MEASURING SPECIFIC RESISTIVITY AND HALL EFFECT OF DISCS OF ARBITRARY SHAPE," in *Semiconductor Devices: Pioneering Papers*, vol. 13, WORLD SCIENTIFIC, 1991, pp. 174–182.

[74]   C. Y. Ho, R. W. Powell, and P. E. Liley, "Thermal Conductivity of the Elements," *J. Phys. Chem. Ref. Data*, vol. 1, no. 2, pp. 279–421, 1972.

[75]   P. P. Freitas and L. Berger, "Effect of atomic order on the electrical resistivity of CoxFe100-x alloys," *Phys. Rev. B*, vol. 37, no. 11, pp. 6079–6084, 1988.

[76]   "C. H. Johansson and J. O. Linde: Ann. Phys. 25 (1936) 1."

[77]   J. C. Zhao, X. Zheng, and D. G. Cahill, "Thermal conductivity mapping of the Ni-Al system and the beta-NiAl phase in the Ni-Al-Cr system," *Scr. Mater.*, vol. 66, no. 11, pp. 935–938, 2012.

[78]   C. Wei, N. Antolin, O. D. Restrepo, W. Windl, and J. C. Zhao, "A general model for thermal and electrical conductivity of binary metallic systems," *Acta Mater.*, vol. 126, pp. 272–279, 2017.

[79]   "Touloukian, Yeram Sarkis, et al. Thermophysical properties of matter-the tprc data series. volume 1. thermal conductivity-metallic elements and alloys. THERMOPHYSICAL AND ELECTRONIC PROPERTIES INFORMATION ANALYSIS CENTER LAFAYETTE IN, 1970."

[80]   M. W. Ackerman and T. N. Havill, "Thermal conductivity of ten selected binary alloy systems," *J. Phys. Chem. Ref. Data*, vol. 7, no. 3, pp. 959–1178, 1978.

[81]   "Powell, Robert L., and William A. Blanpied. 'Thermal conductivity of metals and alloys at low temperatures: a review of the literature.' (1954)."

[82]   Y. Terada, K. Ohkubo, T. Mohri, and T. Suzuki, "Thermal conductivity of intermetallic compounds with metallic bonding," *Mater. Trans.*, vol. 43, no. 12, pp. 3167–3176, 2002.

[83]   "Ashcroft, Neil W., and N. David Mermin. 'Solid state physics.' (1976)."

[84]   D. Gall, "Electron mean free path in elemental metals," *J. Appl. Phys.*, vol. 119, no. 8, 2016.

[85] "Smith, C.S. and Palmer, E.W., 1935. Thermal and electrical conductivities of copper alloys. Trans AIME Papers, 221, pp.225-241."

[86] R. W. Hill, C. Proust, L. Taillefer, P. Fournier, and R. L. Greene, "Breakdown of Fermi-liquid theory in a copper-oxide superconductor," *Nature*, vol. 414, no. 6865, pp. 711–715, 2001.

[87] H. Pfau *et al.*, "Thermal and electrical transport across a magnetic quantum critical point," *Nature*, vol. 484, no. 7395, pp. 493–497, 2012.

[88] M. A. Tanatar, J. Paglione, C. Petrovic, and L. Taillefer, "Anisotropic violation of the wiedemann-franz law at a quantum critical point," *Science (80-.).*, vol. 316, no. 5829, pp. 1320–1322, 2007.

[89] A. Garg, D. Rasch, E. Shimshoni, and A. Rosch, "Large violation of the wiedemann-franz law in luttinger liquids," *Phys. Rev. Lett.*, vol. 103, no. 9, pp. 1–4, 2009.

[90] K. S. Kim and C. Pépin, "Violation of the Wiedemann-Franz law at the kondo breakdown quantum critical point," *Phys. Rev. Lett.*, vol. 102, no. 15, pp. 1–4, 2009.

[91] C. Hess *et al.*, "Magnon heat transport in (Sr, Ca, La)14Cu24O41," *Phys. Rev. B - Condens. Matter Mater. Phys.*, vol. 64, no. 18, pp. 1843051–1843056, 2001.

[92] R. Padhye, A. J. A. Aquino, D. Tunega, and M. L. Pantoya, "Fluorination of an Alumina Surface: Modeling Aluminum-Fluorine Reaction Mechanisms," *ACS Appl. Mater. Interfaces*, vol. 9, no. 28, pp. 24290–24297, 2017.

[93] C. A. Crouse, "Fluorinated polymers as oxidizers for energetic composites," *ACS Symp. Ser.*, vol. 1106, pp. 127–140, 2012.

[94] H. Wang, M. Rehwoldt, D. J. Kline, T. Wu, P. Wang, and M. R. Zachariah, "Comparison study of the ignition and combustion characteristics of directly-written Al/PVDF, Al/Viton and Al/THV composites," *Combust. Flame*, vol. 201, pp. 181–186, 2019.

[95] Y. Mao *et al.*, "Rational design of gradient structured fluorocarbon/Al composites towards tunable combustion performance," *Combust. Flame*, vol. 230, p. 111436, 2021.

[96] D. W. Kim, K. T. Kim, T. S. Min, K. J. Kim, and S. H. Kim, "Improved Energetic-Behaviors of Spontaneously Surface-Mediated Al Particles," *Sci. Rep.*, vol. 7, no. 1, pp. 1–9, 2017.

[97]   J. A. Bencomo, S. T. Iacono, and J. McCollum, "3D printing multifunctional fluorinated nanocomposites: Tuning electroactivity, rheology and chemical reactivity," *J. Mater. Chem. A*, vol. 6, no. 26, pp. 12308–12315, 2018.

[98]   M. C. Rehwoldt, D. J. Kline, and M. R. Zachariah, "Numerically evaluating energetic composite flame propagation with thermally conductive, high aspect ratio fillers," *Chem. Eng. Sci.*, vol. 229, p. 116087, 2021.

[99]   "Eucken, A. 'Forschg. Gebiete Ingenieurw.' Forschungsheft 3 (1932): 16."

[100] "J. C. Maxwell, A treatise on electricity and magnetism, vol. I, 3rd Ed, Oxford University Press, 1904."

[101] T. B. Lewis, L. E. Nielsen, and M. Company, "Dynamic Mechanical Properties of Particulate- Filled Composites," vol. 14, pp. 1449–1471, 1970.

[102] L. E. Nielsen, "Thermal conductivity of particulate-filled polymers," *J. Appl. Polym. Sci.*, vol. 17, no. 12, pp. 3819–3820, Dec. 1973.

[103] R. Pal, "On the Lewis-Nielsen model for thermal/electrical conductivity of composites," *Compos. Part A Appl. Sci. Manuf.*, vol. 39, no. 5, pp. 718–726, 2008.

[104] A. R. Spurr, "A low-viscosity epoxy resin embedding medium for electron microscopy," *J. Ultrastruct. Res.*, vol. 26, no. 1–2, pp. 31–43, Jan. 1969.

[105] "Nielsen, Lawrence E. 'The thermal and electrical conductivity of two-phase systems.' Industrial & Engineering chemistry fundamentals 13.1 (1974): 17-20."

[106] X. Wang, V. Ho, R. A. Segalman, and D. G. Cahill, "Thermal conductivity of high-modulus polymer fibers," *Macromolecules*, vol. 46, no. 12, pp. 4937–4943, 2013.

[107] X. Liu and Q. Wu, "PP/clay nanocomposites prepared by grafting-melt intercalation," *Polymer (Guildf).*, vol. 42, no. 25, pp. 10013–10019, Dec. 2001.

[108] D. Qian, E. C. Dickey, R. Andrews, and T. Rantell, "Load transfer and deformation mechanisms in carbon nanotube-polystyrene composites," *Appl. Phys. Lett.*, vol. 76, no. 20, pp. 2868–2870, May 2000.

[109] K. Pietrak and T. Wiśniewski, "A review of models for effective thermal conductivity of composite materials," *J. Power Technol.*, vol. 95, no. 1, pp. 14–24, 2015.

[110] J. Z. Xu, B. Z. Gao, and F. Y. Kang, "A reconstruction of Maxwell model for effective thermal conductivity of composite materials," *Appl. Therm. Eng.*, vol. 102, pp. 972–979, 2016.

[111] T. Zhan, L. Fang, and Y. Xu, "Prediction of thermal boundary resistance by the machine learning method," *Sci. Rep.*, vol. 7, no. 1, pp. 1–2, 2017.

[112] "R. O. P. E. T. Swarz, Thermal boundary resistance, Rev. Mod. Phys. 61 (3) (1989) 605."

[113] F. Kargar *et al.*, "Thermal Percolation Threshold and Thermal Properties of Composites with High Loading of Graphene and Boron Nitride Fillers," *ACS Appl. Mater. Interfaces*, vol. 10, no. 43, pp. 37555–37565, 2018.

[114] Y. Su, J. J. Li, and G. J. Weng, "Theory of thermal conductivity of graphene-polymer nanocomposites with interfacial Kapitza resistance and graphene-graphene contact resistance," *Carbon N. Y.*, vol. 137, pp. 222–233, 2018.

[115] S. Y. Kwon, I. M. Kwon, Y. G. Kim, S. Lee, and Y. S. Seo, "A large increase in the thermal conductivity of carbon nanotube/polymer composites produced by percolation phenomena," *Carbon N. Y.*, vol. 55, pp. 285–290, 2013.

[116] M. Shtein, R. Nadiv, M. Buzaglo, K. Kahil, and O. Regev, "Thermally conductive graphene-polymer composites: Size, percolation, and synergy effects," *Chem. Mater.*, vol. 27, no. 6, pp. 2100–2106, 2015.

[117] W. Lin, R. Zhang, and C. P. Wong, "Modeling of thermal conductivity of graphite nanosheet composites," *J. Electron. Mater.*, vol. 39, no. 3, pp. 268–272, 2010.

[118] K. M. F. Shahil and A. A. Balandin, "Graphene-multilayer graphene nanocomposites as highly efficient thermal interface materials," *Nano Lett.*, vol. 12, no. 2, pp. 861–867, 2012.

[119] N. Shenogina, S. Shenogin, L. Xue, and P. Keblinski, "On the lack of thermal percolation in carbon nanotube composites," *Appl. Phys. Lett.*, vol. 87, no. 13, pp. 1–3, 2005.

[120] A. D. Avery, S. J. Mason, D. Bassett, D. Wesenberg, and B. L. Zink, "Thermal and electrical conductivity of approximately 100-nm permalloy, Ni, Co, Al, and Cu films and examination of the Wiedemann-Franz Law," *Phys. Rev. B - Condens. Matter Mater. Phys.*, vol. 92, no. 21, pp. 1–10, 2015.

[121] J. Crossno *et al.*, "Observation of the Dirac fluid and the breakdown of the Wiedemann-Franz law in graphene," *Science (80-.).*, vol. 351, no. 6277, pp. 1058–1061, 2016.

[122] S. Lee *et al.*, "Anomalously low electronic thermal conductivity in metallic vanadium dioxide," *Science (80-.).*, vol. 355, no. 6323, pp. 371–374, 2021.